Buffer gas loading and evaporative cooling in the multi-partial-wave regime

A thesis presented

by

Scott Vinh Nguyen

to

The Department of Physics

in partial fulfillment of the requirements

for the degree of

Doctor of Philosophy

in the subject of

Physics

Harvard University

Cambridge, Massachusetts

May 2006

To my parents

for all their sacrifices.

Thesis advisor

John Morrissey Doyle

Author

Scott Vinh Nguyen

Buffer gas loading and evaporative cooling in the multi-partial-wave regime

Abstract

This thesis describes the study of collisions in the multi-partial-wave regime relevant to the buffer gas cooling and trapping of atoms. A quantitative model is formulated to describe the dynamics of evaporative cooling and is used to infer elastic and inelastic collision rate constants of $g_{el} = 2.15(+2.5, -1.2) \times 10^{-10}$ cm^3/s and $g_{in} = 1.36(+1.2, -0.7) \times 10^{-12}$ cm^3/s between two chromium atoms in the temperature range of 0.02-1 K and explains a long standing discrepancy between theory and experiment. Magnetic trapping is then extended to atomic manganese where up to 2×10^{12} Mn atoms are trapped in all six hyperfine states, allowing for the exploration of the role of the hyperfine interaction in spin-exchange collisions. In addition, we simultaneously trap a ^{55}Mn-^{52}Cr mixture and measure an inter-species inelastic rate constant of $g_{\mathrm{Mn,Cr}} = 1.5\,(\pm 0.2) \times 10^{-13}$ cm^3/s. Demonstrating that buffer gas loading is a viable alternative to laser cooling, we have magnetically trapped and evaporatively cooled metastable helium in large numbers. 10^{11} ^{4}He* atoms are trapped at an initial temperature of 400 mK and evaporatively cooled into the ultracold regime, resulting in a cloud of $2 \pm 0.5 \times 10^9$ atoms at 1.4 ± 0.2 mK and an increase in phase space density of 5 orders of magnitude. Efficient evaporation indicates low collisional loss for ^{4}He* in both the ultracold and multi-partial-wave regime, in agreement with theory.

Contents

List of Figures

List of Tables

Citations to Previously Published Work

Portions of this thesis have appeared previously in the following papers:

"Buffer gas cooling and trapping of atoms with small effective magnetic moments", J.G.E. Harris, R.A. Michniak, S.V. Nguyen, N. Brahms, W. Ketterle, J.M. Doyle, *Europhysics Letters* **67**, 198 (2004).

"Magnetic trapping of an atomic Mn-Cr mixture", S.V. Nguyen, J.S. Helton, K. Maussang, W. Ketterle, and J.M. Doyle, *Physical Review A* **71**, 025602 (2005).

"Evaporation of metastable helium in the multi-partial-wave regime", S.V. Nguyen, S.C. Doret, C.B. Connolly, R.A. Michniak, W. Ketterle, and J.M. Doyle, *Physical Review A* **72**, 060703(R) (2005).

Acknowledgements

The sanity that I kept in this insane maze was due in large part to the community that supported me, and for this I would like to acknowledge them.

I thank my advisor John Doyle for giving me the opportunity to explore my physics curiosity and for fostering the intellectually stimulating and fun lab environment necessary for physics research to thrive. I also thank Wolfgang Ketterle, the co-PI on my project, for his expert advice and the deep insights that he would impart during our meetings.

Because of the complexity of our experiments, the success that has been achieved came only from a collaborative effort. I want to especially thank Jack Harris and Bob Michniak. Six years ago the experiment was only an idea, but their heavy lifting during the initial phases really set the tone for the rest of the project. Not only was working with them fun, but also the greatest learning experience I have ever had. And I apologize for the skipped heartbeats I might have caused. For the most part, the cell remained intact.

I also want to thank Joel Helton and Kenneth Maussang for their work on the manganese experiment and the calcium fluoride experiment to which Dima Egorov was also a lead contributor; Charlie Doret and Colin Connolloy, for their work on the metastable helium experiment; Rob deCarvalho, for his work in reanalyzing the chromium data; and Andrew Jayich, for his various contributions including a few holes in the wall and an unhinged door.

To the rest of the Doyle group, thank you for making the time spent in lab not feel like time spent at work.

I am also grateful to Vickie Greene and Shiela Ferguson for not only doing their

job so well, but also for providing me with the wise advise that only grandmothers would have.

Of course, I want to thank my buddies Ania Bleszynski, Bola George, Ronnie Potok, and Ryan Barnett for filling my six years in Cambridge (from the halls of Perkins to the bar at Grafton Steet) with fond memories. In particular, I want to thank Ryan whose Oscar winning performance as wing-man the night of July 19, 2003 led me to meeting my true love Jana Makell Leon Guerrero. She has added an extra dimension to my final three years in graduate school.

Finally, I am deeply grateful to my family for the sacrifices they have made for me. Twenty-six years ago, I don't think we knew what exactly was in store for us as we sailed out to the South China Sea. With some good fortune and perseverance, I think everything turned out okay. To my sister and brother, I thank you for your love and support. Without your trailblazing ways, my path would have been much more difficult. And to my mom and dad, I owe everything to you. How can one even quantify the choice you made to leave your homeland to ensure that we kids would have the opportunities that everyone should be entitled to?

Chapter 1

Introduction

For the past twenty years or so, atomic physicists have been developing the technology and the techniques that would enable the study of atomic and molecular processes at temperatures just a fraction of a degree above absolute zero. In addition to being able to produce the coldest temperatures in the universe right in our own laboratories, quite a few interesting physics phenomena have been discovered. Since temperature is a measure of the average energy of a system, accessing different temperature ranges gives us access to different physical phenomena. Given our experience in studying physics occurring at high temperatures, we are now interested in what phenomena occur when atoms and molecules are at temperatures just a millionth of a degree above absolute zero.

The initial motivation to cool atoms down to low temperatures was for precision measurement where the reduction of Doppler effects and increased interaction times would lead to improved spectroscopic sensitivity. This higher precision is the reason behind the push to replace the hot cesium beam used in atomic clocks with a new standard based on cold atoms [1]. In addition to improved sensitivity, the removal of the thermal motion of the atoms has enabled a new level of control of both their

position and motion. For example, with the use of optical fields atoms can be positioned in a periodic lattice replicating some of the most complicated crystal structures normally only seen in solids [2, 3]. Using magnetic fields, the confinement of atoms to traverse circular paths in atom interferometers should lead to higher sensitivity gyroscopes for use in navigation [4, 5].

As the atoms and molecules are cooled, their quantum mechanical nature begins to dominate. For instance, collisions of atoms and molecules at these low temperatures are a sensitive measure of the details of the internuclear potential of the colliding pair [6]. Inelastic and reactive channels can be resonantly tuned through the use of external fields leading to processes which were simply washed out by the large thermal distribution at higher temperatures [7]. Experimental studies of photoassociation and Feshbach resonances in the alkali-metals have produced the most accurate internuclear potentials known to date [8, 9, 10]. This has lead to the identification of higher order inelastic collisional processes that were previously unknown. For instance, second order spin-orbit coupling in the collision of two cesium atoms gave rise to such high inelastic rates that efforts to cool magnetically trapped cesium atoms were soon abandoned [11].

As the temperature decreases, the thermal deBroglie wavelength increases to a length which is comparable to the inter-particle separation, leading to quantum degeneracy. Two of the greatest achievements of modern atomic physics were the attainment of Bose-Einstein condensation in 1995 [12, 13, 14] and Fermi-degeneracy in 1999 [15]. These two quantum degenerate phases are a consequence of the combination of many-body effects and quantum mechanical identical particle symmetries. Because of the experimental control of a variety of physical parameters, these systems have become the testing ground for a host of theoretical work which is now crossing

over into the field of condensed matter physics. For example, the study of bosons and fermions in optical lattices are producing experimental evidence for extensions of the Bose-Hubbard model [16, 17]. This could potentially lead to the understanding of the physical origins of high temperature superconductivity, currently a highly debated topic in the condensed matter arena.

1.1 Cooling and trapping

All of the physics described above are examples of the rich and diverse array of physical phenomena that are accessible at low temperatures. However, there is still much more to explore, and for all of these potential experiments, there should ideally exist a ready source of atoms which are cold and dense. Unfortunately, simply putting the gas of atoms into contact with something very cold like a dilution refrigerator ($\sim$ 10 mK) will not work. The binding energy of atoms to most surfaces is generally greater than $\sim$ 1 K [18], and hence the gas of atoms would simply freeze onto the walls of the container as the system is cooled down. Therefore it is necessary to confine the atoms in free space to prevent them from touching the walls of the container.

For neutral particles this is generally achieved by magnetically trapping the atoms. This process relies on the interaction of an atom's magnetic moment μ with external magnetic fields. The forces that are exerted on an atom by the magnetic field gradient will depend on the orientation of the magnetic moment relative to the external magnetic field lines (Fig. 1.1). Magnetic moments which are aligned with the magnetic field will feel a force pushing them to higher fields and as such are termed "high-field seekers." Magnetic moments which are anti-aligned with the magnetic field lines feel a force pushing them towards lower fields and are termed "low-field seekers." Because it is impossible to produce a magnetic field maximum in free space [19], only the

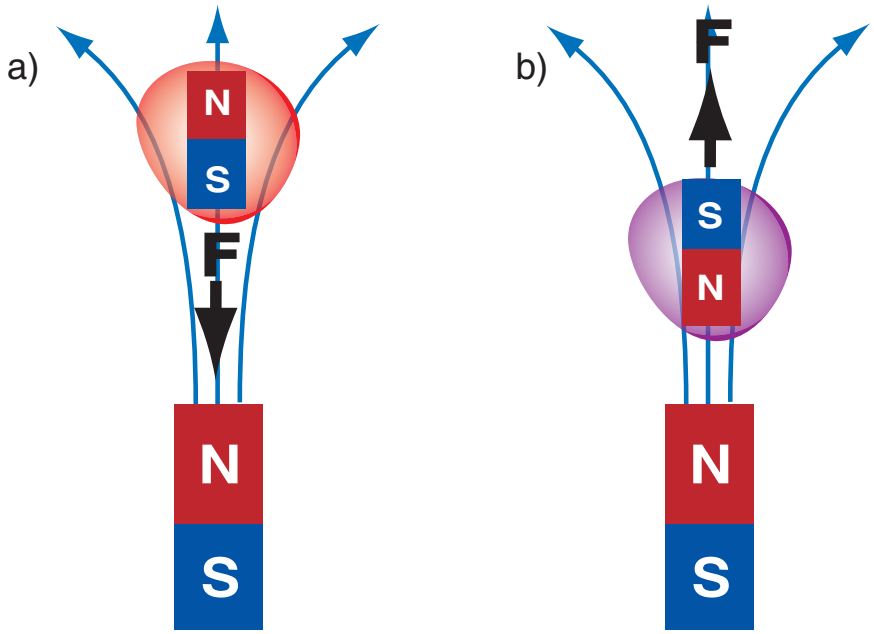

Figure 1.1: Forces exerted on a paramagnetic atom by an external magnetic field gradient. The small magnet represents the orientation of the atom's magnetic moment. a) Untrappable high-field seeker. b) Trappable low-field seeker.

low-field seekers are magnetically trappable; high field seekers are ejected from the trap.

Unfortunately, high-field seekers are the lower energy, thermodynamically favored states. As such, it is possible for trapped low-field seekers to undergo transitions to these lower energy states via collisions. These inelastic collisions lead to trap loss and are to be avoided if the goal is to achieve a large sample of cold atoms.

In practice, magnetic traps have a magnetic field strength that increases radially outwards from a central B_{min} to a maximum finite magnetic field B_{max}, the difference of which is known as the trap depth $B_{\text{trap}} \equiv B_{\text{max}} - B_{\text{min}}$. The deepest magnetic traps to date have a trap depth of $B_{\text{trap}} = 4.1$ T, currently limited by superconducting technology [20]. Atoms can only be trapped if they obey the following "Golden Rule"

of magnetic trapping

$$\mu B_{\text{trap}} > k_{\text{B}} T. \tag{1.1}$$

For $\mu = \mu_{\text{B}}$ and with the deepest magnetic trap, $\mu B_{\text{trap}}/k_{\text{B}} \sim 1$ K. Therefore, in addition to magnetic trapping, the study of cold atoms requires some cooling process to load the atoms into the trap. Fortunately, there are two methods which are capable of cooling hot atoms down to a temperature such that they can be magnetically trapped: laser cooling and buffer gas cooling (Fig. 1.2).

1.2 Laser cooling

First demonstrated in 1982 in the cooling of a beam of sodium atoms [21], laser cooling has become the standard method to produce cold atoms [22]. Laser cooling relies on multiple absorption and re-emission of photons from a red-detuned laser. The Doppler shift will cause fast atoms to preferentially absorb the counter-propagating photons, and since the emission is random, the net effect is a reduction in the forward momentum of the atom. Using this method, atoms can be cooled into the ultracold regime (< 1 mK) where effects of collisions between the atoms can be described by a single parameter, the s-wave scattering length [6].

Because the momentum $\hbar k$ imparted on the atom is small, laser cooling usually relies on tens of thousands of photon scattering events. Atoms with simple level structures where a cyclic atomic transition is available is best suited for laser cooling. Unfortunately, most atoms have a fairly complex level structure such that there is a high probability of decaying to a state different from that of the initial state. Decay to these off-resonant states stymies the cooling process and makes laser cooling not applicable to these atoms. The situation is even worse in the case of molecules. The additional degrees of freedom from the rotation and vibration of the molecules add to

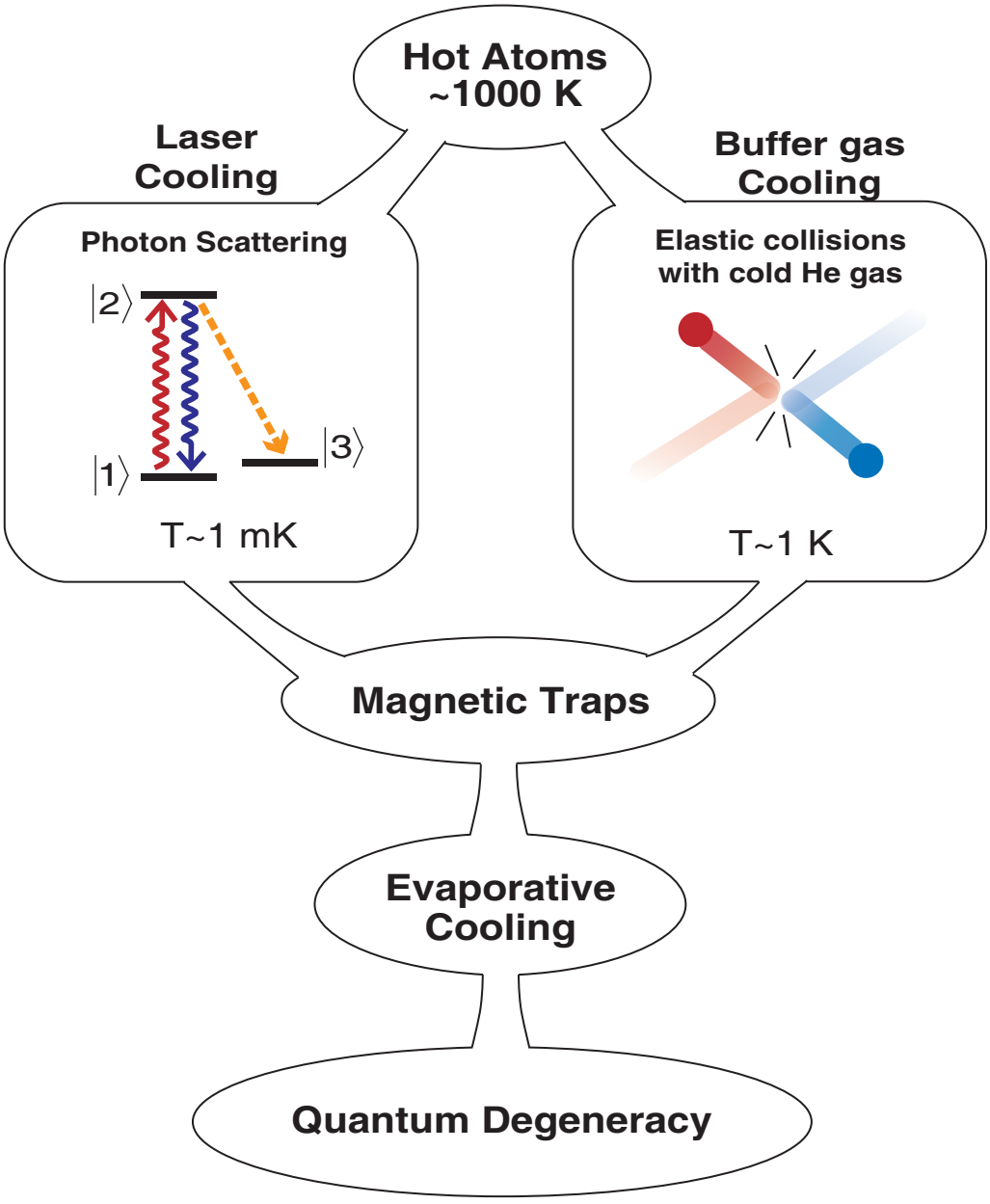

Figure 1.2: Cooling paths from hot atoms to quantum degeneracy.

the complexity of the level structure, providing an enhanced number of off-resonant states to which the molecule can decay. For this reason, laser cooling is not a general method to produce cold atoms or molecules. Thus far it has been demonstrated with atoms with simple level structures, most notably the alkali-metals and metastable noble gases.

Laser cooling also has limits on the size and density of the atomic samples it can cool. Excited state collisions and radiation trapping limit the densities to $\sim 10^{12}$ cm^{-3} and atom numbers to $\sim 10^{10}$ [23]. This is orders of magnitude smaller than the fundamental limits associated with magnetic traps.

1.3 Buffer gas cooling

Buffer gas cooling is an alternative method to loading a magnetic trap that does not face the same limitations as laser cooling [24]. It relies on elastic collisions with a cryogenically cooled helium buffer gas to cool the sample down to temperatures below that of the trap depth. Any atoms which have not thermalized with the helium gas are simply lost to the walls of the container. Among those that have thermalized, the atoms in the low-field seeking state are subsequently trapped whereas those in the high-field seeking states are ejected from the trap. The helium atoms which are non-magnetic are then removed, leaving behind a thermally isolated, trapped sample. Figure 1.3 shows the step by step process of buffer gas cooling and trapping.

Because it relies solely on elastic collisions, buffer gas cooling is a general cooling technique that is applicable to any paramagnetic species regardless of internal structure. Therefore not only are other atoms across the periodic table amenable to this cooling method, but so are molecules. In addition, there are no density or number limitations; the entire thermal distribution may be loaded. Thus far, buffer gas cool-

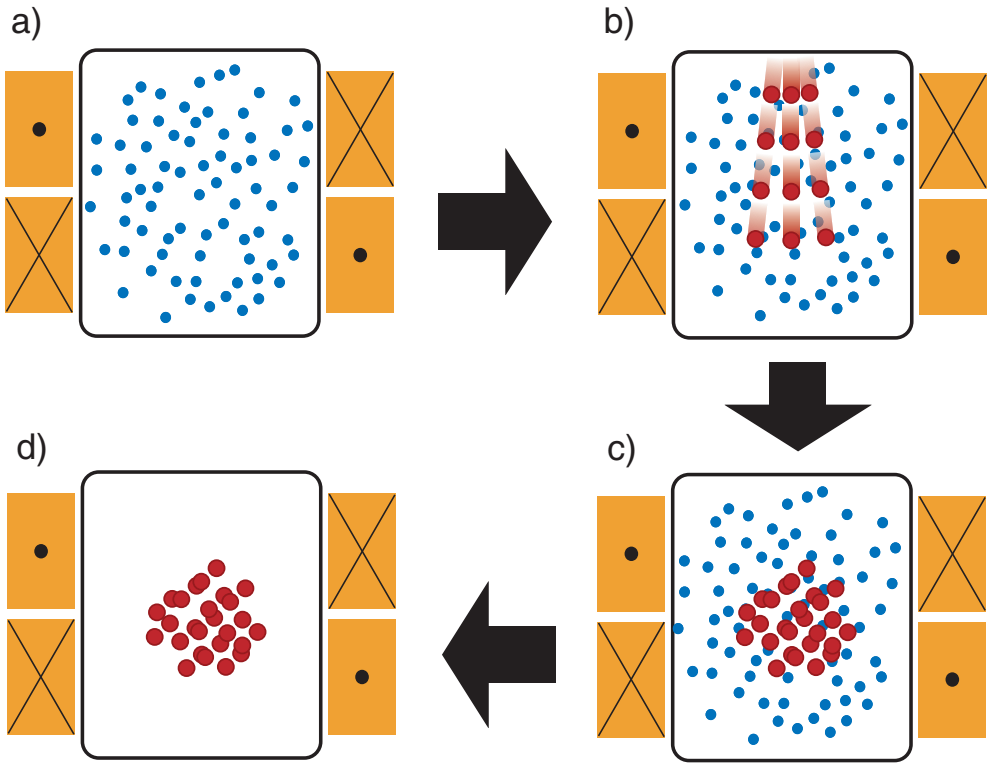

Figure 1.3: Buffer gas cooling and trapping procedure. a) Container is filled with helium gas at ~ 0.5 K. Magnetic trap is made by two superconducting solenoids with current running in opposite directions. b) Introduce hot gas. c) Sample collides with the helium gas and the low-field seekers are magnetically trapped. d) The helium gas is removed, leaving behind a thermally isolated trapped sample.

ing has been shown to be successful for magnetically trapping and thermally isolating several atomic samples including europium [25], chromium [26], holmium, and dysprosium [27], each with numbers greater than 10^{11} (limited solely by the production efficiency). Buffer gas cooling has also been shown to be successful for magnetically trapping 10^8 calcium hydride CaH molecules [28]. The CaH molecules though were still embedded in the helium buffer gas and therefore were not thermally isolated.

The process of thermal isolation is at the heart of the latest technological advance made in the buffer gas cooling method. In the original implementation of buffer gas cooling, the helium buffer gas was removed by lowering the temperature of the cell to

below 100 mK via a dilution refrigerator. As the cell cools, the vapor pressure of either ^{3}He and ^{4}He is dramatically reduced and the helium gas no longer provides a thermal link to the walls. It takes a few seconds though to "freeze out" the buffer gas. Samples with trap lifetimes shorter than this do not survive the thermal isolation process. This was the case for CaH. The trap lifetime depends exponentially on the ratio of the magnetic trap depth to temperature which we define to be $\eta \equiv \mu B_{\mathrm{trap}}/k_{\mathrm{B}}T$ [29]. For atoms with very large magnetic moments like Cr ($6\mu_{\mathrm{B}}$) and Eu ($7\mu_{\mathrm{B}}$), the trap life time is longer than a few seconds under normal operating temperatures and trap depths. On the other hand, those with low magnetic moments like CaH or sodium ($1\mu_{\mathrm{B}}$) have trap lifetimes of < 50 ms for similar operating conditions.

To address this issue, a fast actuating large aperture cryogenic valve was developed and incorporated into the buffer gas loading procedure [30]. The valve separates the cell into two regions, a trapping region and a vacuum region. With the valve initially closed, the loading procedure proceeds through frames **a** through **c** as shown in Figure 1.3. After the atoms have thermalized and are subsequently trapped, the valve is then opened. The helium buffer gas is pumped out, leaving behind a thermally isolated, trapped sample. The valve can be fully extended in < 20 ms with minimal vibration onto the cell. The timescale to pump-out the helium gas is limited by the conductance of the valve aperture.

The development of this pump-out technique greatly extends the number of species which can now be successfully buffer gas loaded and thermally isolated. Buffer gas loading is no longer limited to only species with large magnetic moments. Figure 1.4 shows the efficiency of buffer gas loading as a function of the magnetic moment μ_{eff} of species to be trapped. For $\mu_{\mathrm{eff}} \geq 3\mu_{\mathrm{B}}$, atoms were trapped and thermally isolated with almost unit efficiency. For $\mu_{\mathrm{eff}} < 3\mu_{\mathrm{B}}$, the fraction of atoms remaining after

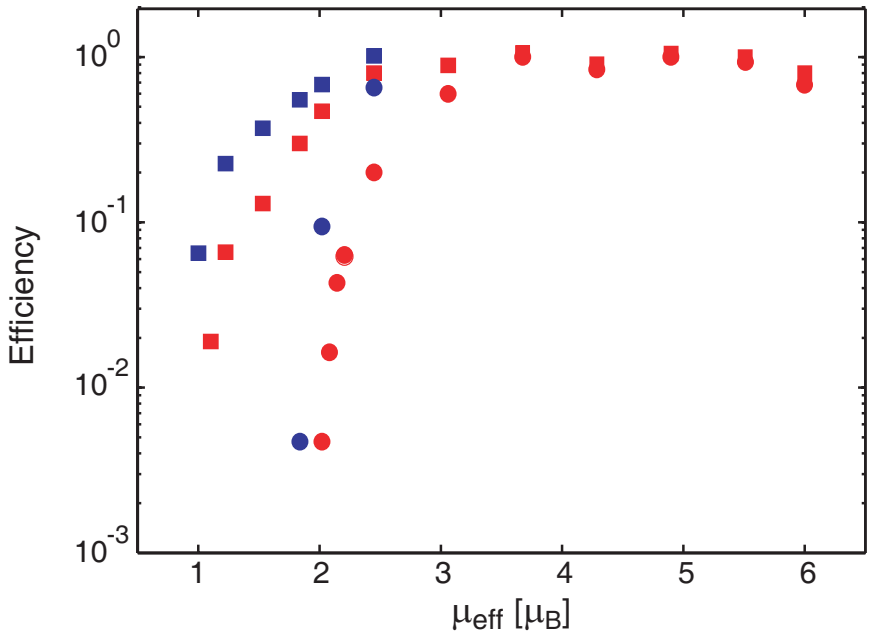

Figure 1.4: Efficiency of buffer gas loading using the pump-out technique to achieve thermal isolation. The squares represent the efficiency of atoms trapped after 300 ms after the valve is opened. Atoms remaining at this timescale are trapped but not thermally isolated. The solid circles represent the efficiency atoms remaining 10 s after the valve is opened. Atoms remaining at this timescale are trapped and thermally isolated. The lighter data points are taken at $T = 550$ mK, and the darker data points are taken at $T = 480$ mK.

full thermal isolation was limited by wind from the rapid removal of the buffer gas and desorbing helium film from the cell walls. Of particular note is the capability of magnetically trapping and thermally isolating atoms with $\mu_{\text{eff}} = 2$. This triples the number of species that can be buffer gas cooled, trapped, and thermally isolated, and bridges the gap between atoms which can be buffer gas cooled and those which have been evaporatively cooled to quantum degeneracy inside a magnetic trap (all of which have $\mu \leq 2\mu_{\text{B}}$) [1].

[1]Chromium ($6\mu_{\text{B}}$) was cooled to degeneracy in the lowest Zeeman level in an optical trap [31]

1.4 Evaporative cooling

Once loaded into a magnetic trap using either cooling method, the sample is still many orders of magnitude from the quantum degenerate regime where the phase space density approaches unity. Reaching quantum degeneracy requires additional cooling. All successful efforts thus far to achieve either a Bose-Einstein condensate or Fermi degenerate gas have utilized evaporative cooling which relies on the removal of the highest energy atoms inside the trap distribution [32]. This lowers the average energy of the sample. Elastic collisions will then rethermalize the remaining atoms to a new lower temperature. Successive iterations of this process can lead to very low temperatures and very high phase space densities. First suggested by Hess in 1986 for cooling atomic hydrogen [33], evaporative cooling was soon implemented for cooling the alkali-metals, resulting in the Bose-Einstein condensation of rubidium, sodium, and lithium in 1995 [12, 13, 14].

Evaporative cooling is implemented by simply setting a finite trap depth. Atoms with energies higher than the trap depth are lost from the trap and stick to the walls. Even though evaporation will still occur with a static trap depth, the process can be enhanced by actively lowering the trap depth as the system cools. This process called "forced evaporation" is generally implemented in one of two ways. The first method which is straight forward to implement in a cryogenic environment is to reduce the magnitude of the confining magnetic potential. The second method relies on driving RF transitions from the low-field seeking state to the high-field seeking, untrapped state [34]. The magnetic field gradient of the trap allows the higher energy atoms to be spectroscopically selected from the trap distribution. Because evaporation by an RF-knife does not require changing the confining potential, it is easier to achieve the high densities needed for evaporation and has thus become the standard evaporative

cooling method. Similar in concept to an RF-knife, the trap depth can be set by a physical surface which moves into the trapped sample, or alternatively the trapped sample can be moved in towards the surface. The position of the surface which adsorbs the higher energy atoms sets the trap depth [35, 36].

A necessary consequence of evaporative cooling is the loss of atoms. However, because each evaporated atom can carry away a significant fraction of the total energy of the system, large increases in phase space density can be achieved with minimal loss in atom number. For example, in creating sodium condensates, only two orders of magnitude of atom number are lost for an increase of six orders in phase space density [32]. This efficiency is set by the rate of certain loss processes relative to the rate of elastic collisions which produce evaporated atoms. Loss processes can include collisions with background gas, Majorana loss, and inelastic collisions which produce states which are not magnetically trappable. Successful evaporative cooling requires that these loss processes be minimized during evaporation. Unfortunately, inelastic collisions are sometimes an uncontrollable consequence of the particular choice of atomic species and are not technical in origin. As mentioned before, second order spin-orbit coupling prevented cesium from joining the quantum degenerate club until 2003 when Weber *et al.* evaporatively cooled cesium atoms in their lowest Zeeman level which is impervious to inelastic collisions [37].

Evaporative cooling a buffer gas loaded sample is inherently different than for a laser cooled sample. Because laser cooling is capable of cooling atoms down to temperatures < 1 mK, only one partial wave (s-wave) contributes to the collisional processes during evaporative cooling. With buffer gas cooling, atoms are initially loaded into the magnetic trap at ~ 1 K. At these temperatures, ~ 10 partial waves contribute to the collisional dynamics. Not only does this add many more channels

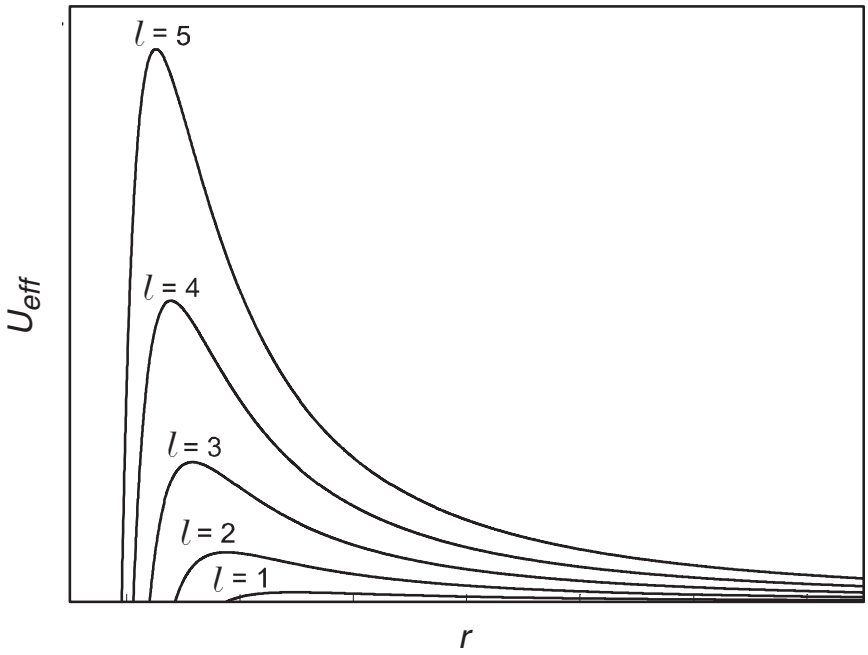

Figure 1.5: Effective potential between two colliding atoms for the first five partial waves l.

for inelastic processes such as dipolar relaxation or spin-exchange, the multiple partial waves introduce an angular momentum term $\hbar^2 l(l+1)/(2mr^2)$ to the interaction of two colliding atoms where l is the angular momentum quantum number and r is the distance between the colliding pair(Fig. 1.5). One consequence of this angular momentum term is the formation of a potential barrier, giving rise to "shape resonances" which can resonantly enhance a collisional process [38]. Therefore the role of shape resonances in the evaporative cooling process needs to be understood to ensure that a buffer gas loaded sample can be successfully cooled to quantum degeneracy [39].

1.5 Thesis overview

This thesis describes work to understand the various collisional processes relevant to buffer gas cooling in the multi-partial wave regime. In Chapter 2, a quantitative

model describing the dynamics of evaporative cooling is presented. The microscopic collisional processes are averaged over the trap distribution and related to the measurable quantities of atom number and temperature. The application of this model to understanding both elastic and inelastic collisions of two chromium Cr atoms is presented in Chapter 3, explaining a longstanding discrepancy between measured and theoretical values. Chapter 4 describes the extension of magnetic trapping to a new atomic species manganese (Mn). By trapping all six hyperfine states and measuring each state's decay from the trap, we are able to explore spin-exchange collisions in this transition metal. In addition we are able to study inter-species inelastic collisions with the first simultaneous trapping of a Mn-Cr mixture. Chapters 5 and 6 describes our successful effort to produce, buffer gas cool, magnetically trap, and evaporative cool large samples of metastable helium He* into the ultracold regime. By moving the He* cloud towards an adsorbing surface, the cloud is evaporatively cooled from 400 mK to 1.4 mK with an increase in phase space density of five orders of magnitude. This is the first significant increase in phase space density for a buffer gas loaded sample and demonstrates that buffer gas loading is a viable alternative to laser cooling. Finally, Chapter 7 describes the experimental modifications necessary to cool the He* further to achieve quantum degeneracy which should lead to exciting potential applications in quantum atom optics and cold molecular gases.

Chapter 2

Evaporative Cooling Model

Thus far, all efforts to create a quantum degenerate gas of atoms have employed evaporative cooling after initially trapping the atoms in a magnetic or optical trap. Cooling of the sample is achieved through selectively removing the higher energy atoms from the trapped distribution, thereby lowering the mean energy of the trapped sample. In this chapter we describe a quantitative model which describes the dynamics of the trapped sample as it is being evaporatively cooled. This model helps elucidate the relationships of the various physical processes which affect the properties of the trapped sample and is used to understand the collisional properties of magnetically trapped atomic chromium, presented in Chapter 3.

This model is an extension of the model developed by Doyle *et al.* [40] which provided a comprehensive treatment of the evaporation of atomic hydrogen. The current model can be applied to any atomic or molecular species and includes a term which accounts for the spilling of particle from the trap due to forced evaporation, a process which was not important for the MIT hydrogen experiments. In the current implementation of this model, each cooling, heating, or atom loss process is easily isolated to analyze its contribution to the evaporation dynamics. A comprehensive

review of other analytical or numerical models of the evaporation process can be found in Reference [32].

2.1 Evaporation model

Collisions are central to the evaporative cooling process. By taking into account the various collisional processes, we are able to model the dynamical evolution of the properties of the trapped sample.

Many of the features of evaporative cooling can be parameterized by the variable $\eta \equiv \mu B_{\rm trap}/k_{\rm B}T$ which is defined to be the ratio of the trap depth to the temperature. The trap depth $E_{\rm th} = \eta k_{\rm B}T$ can be experimentally set by a method depending on the experimental parameters. This includes using a surface to set $\eta k_{\rm B}T$ or the magnetic field gradient to selectively drive transitions from magnetically trapped states to untrapped states.

Given a particular trap depth $E_{\rm th}$, atoms are lost from the trap due to the following processes (Fig. 2.1):

1. Evaporation over the trap edge due to elastic collisions at a rate $\dot{N}_{ev}$. These collisions lead to cooling as higher energy atoms are most likely to be knocked over the trap edge.

2. Spin flips from magnetically trapped states to untrapped states due to inelastic collisions at a rate $\dot{N}_{in}$. This leads to heating as inelastic collisions are most likely to occur at the center of the trap.

3. Atom loss due to background gas collisions knocking the atoms out of the trap at a rate $\dot{N}_{bg}$.

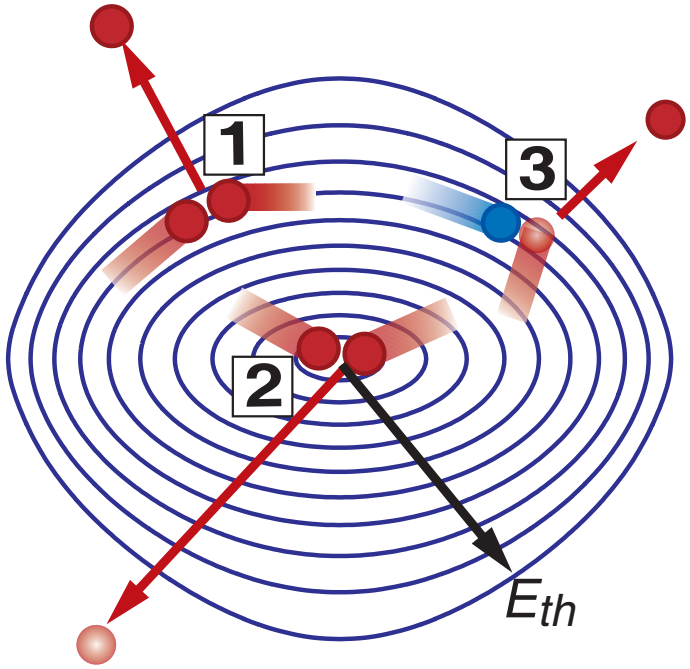

Figure 2.1: Collisional processes relevant to evaporative cooling. $E_{\text{th}} = \eta k_B T$ is the trap depth. 1) Elastic collisions leading to evaporation over the trap edge. 2) Inelastic collisions leading to spin flips. 3) Collisions with background gas leading to trap loss.

4. Atoms lost due to forced evaporation at a rate $\dot{N}_f$. This is the fraction of atoms in the high energy tail of the thermal distribution which is above the trap depth.

The combination of all these processes will govern the evolution of the number of atoms N in the trap given by the following rate equation,

$$\dot{N} = \dot{N}_{ev} + \dot{N}_{in} + \dot{N}_f + \dot{N}_{bg}. \tag{2.1}$$

In this model we do not include atom loss due to three-body recombination which is significant at densities $> 10^{14}$ cm^{-3} [32, 41]. This process can easily be included by adding the appropriate term to Equation 2.1.

Each $\dot{N}$ term is determined by integrating the loss rate over the volume of the trap. The evaluation of each term for a spherically symmetric trap can be found in Reference [32] and Reference [42]. The terms in Reference [32] are valid for in the

high η limit ($\eta > 4$), while the terms in Reference [42] are valid for all values of η. The spatially averaged terms in the high η limit, assuming field independent collision rate constants g_{el} and g_{in}, are summarized below:

$$\dot{N}_{ev} = -\frac{\eta^3}{64\pi r_{\rm th}^3} f(\eta) g_{el} N_{ev}^2 \tag{2.2}$$

$$\dot{N}_{in} = -\frac{\eta^3}{64\pi r_{\rm th}^3} g_{in} N_{in}^2 \tag{2.3}$$

$$\dot{N}_{bg} = -\frac{1}{\tau_{bg}} N \tag{2.4}$$

$$\dot{N}_{f} = \frac{2}{\sqrt{\pi}} \sqrt{\eta} e^{-\eta} \frac{\dot{E}_{\rm th}}{k_{\rm B} T} N. \tag{2.5}$$

In Equations 2.2 and 2.3, $r_{\rm th}$ is the distance from the trap center to the trap edge. In Equation 2.2, $f(\eta)$ is the probability that an elastic collision will result in an atom with an energy greater than the trap depth $\eta k_B T$. In the high η limit, $f(\eta) = 4\sqrt{2}\eta e^{-\eta}$. Equation 2.4 assumes that collisions with the background gas leads only to trap loss at a rate $1/\tau_{bg}$ with no associated heating.

For each atom that is lost due to these processes, there is also a corresponding change in the energy of the trapped distribution $\dot{E} = E\dot{N}$, where E is the energy of the lost atom. This results in a second rate equation that accounts for the change in energy of a trapped distribution,

$$\dot{E} = E_{ev}\dot{N}_{ev} + E_{in}\dot{N}_{in} + E_f\dot{N}_f + \dot{E}_{ad}, \tag{2.6}$$

where $\dot{E}_{ad}$ is the energy change due to adiabatic expansion or compression of the trap. Because entropy is conserved, $\dot{E}_{ad}$ does not increase or decrease the phase space density. The change in the energy of the distribution due to the different processes can be more easily seen if Eq. 2.6 is reexpressed in terms of the average energy $\bar{E}$,

$$N\dot{\bar{E}} = (E_{ev} - \bar{E})\dot{N}_{ev} + (E_{in} - \bar{E})\dot{N}_{in} + (E_f - \bar{E})\dot{N}_f + \dot{E_{ad}}. \tag{2.7}$$

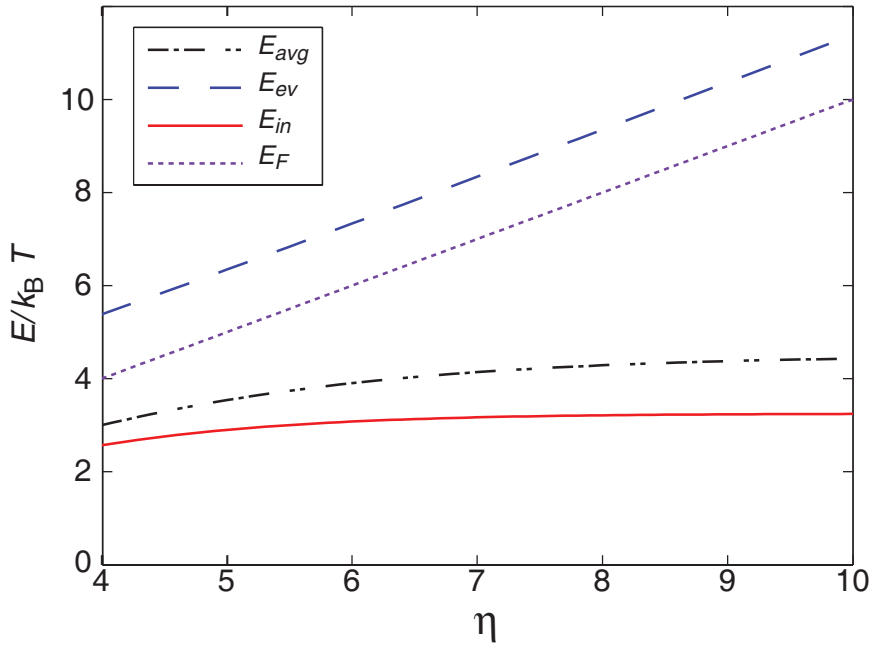

Figure 2.2: Energy scale of the different atomic loss processes.

As is evident from the equation, each loss process can be a heating/cooling term depending on if the energy of the lost atom is smaller/larger than the average energy.

In the infinite η approximation, the energy of each process is summarized below:

$$\bar{E} = \frac{9}{2}k_{\mathrm{B}}T \tag{2.8}$$

$$E_{ev} = (\eta+1)k_{\mathrm{B}}T \tag{2.9}$$

$$E_{in} = 3k_{\mathrm{B}}T \tag{2.10}$$

$$E_F = \eta k_{\mathrm{B}}T \tag{2.11}$$

$$\dot{E}_{ad} = 3k_{\mathrm{B}}T\frac{\dot{E}_w}{E_w}N, \tag{2.12}$$

where E_w is the depth defined by the magnetic trap. Figure 2.2 shows the relationship between the the energy terms as a function of η for $\eta > 4$, .

Equation 2.7 can be related to the temperature of the trap sample. We now have two rate equations to account for the dynamical evolution in atom number and

temperature of the trapped atoms during the evaporative cooling process,

$$\dot{N} = \dot{N}_{ev} + \dot{N}_{in} + \dot{N}_f + \dot{N}_{bg} \tag{2.13}$$

$$\dot{T} = \frac{2}{9k_{\mathrm{B}}}\frac{1}{N}[(E_{ev} - \bar{E})\dot{N}_{ev} + (E_{in} - \bar{E})\dot{N}_{in} + (E_f - \bar{E})\dot{N}_f + \dot{E}_{ad}]. \tag{2.14}$$

From this model, we can draw some interesting conclusions. As shown in Figure 2.2, atoms lost due to inelastic collisions will lead to heating ($E_{in} < \bar{E}$) while two-body evaporation and forced evaporation will lead to cooling ($E_{ev}, E_f > \bar{E}$). As η increases, the amount of cooling possible per atom lost by evaporation improves dramatically. Unfortunately because of the $f(\eta)$ function in Equation 2.2, the evaporation rate E_{ev} is exponentially suppressed at high η's. Therefore as stated in Reference [32], we would have to wait an infinitely long time for a single collision which will remove an atom that carries all the energy of the trap distribution. Furthermore, because both are two-body processes, the number of atoms lost to evaporation over the trap edge relative to the atoms lost to inelastic collisions is simply $\dot{N}_{ev}/\dot{N}_{in} = f(\eta)g_{el}/g_{in}$.

If the trap depth is held constant, the heating rate of inelastic collisions and cooling rate of evaporation will balance, leading to a steady state temperature T_{eq} for the trapped sample. One can easily show that T_{eq} depends solely on the ratio of the elastic and inelastic collision rate (or cross-section),

$$\frac{g_{el}}{g_{in}} = \frac{3}{8\sqrt{2}}\frac{e^{\eta_{\mathrm{eq}}}}{\eta_{\mathrm{eq}}(\eta_{\mathrm{eq}} - 7/2)}, \tag{2.15}$$

where η_{eq} is the "equilibrium η" as determined by T_{eq} and the trap depth (Fig. 2.3).

2.2 Relevant timescales

By lowering the trap depth, the trapped sample will cool to a new lower temperature. Therefore to get an extremely cold sample, we can lower the trap depth to an

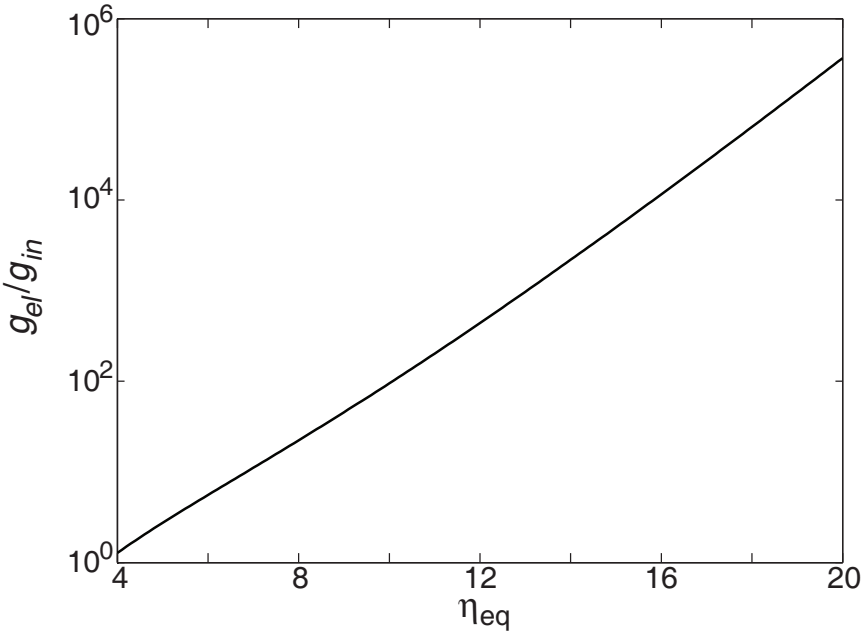

Figure 2.3: Equilibrium η as a function of the ratio of elastic and inelastic cross-sections.

extremely small value. However an instantaneous change to an extremely small trap depth will remove almost all of the atoms in the trap. To balance the negative effect of atom loss and positive effect of cooling, there exists an optimal rate at which the trap depth should be lowered to efficiently evaporate atoms from the trap.

Ideally, the rate of change of the trap depth $\tau_{E_{\rm th}}^{-1}$ should be slower than the cooling rate τ_c^{-1} to allow the system to thermalize before making the next cut in the trap distribution. Changing $E_{\rm th}$ too quickly results in skimming and inefficient cooling. As shown in Figure 2.4, if a cut is taken at E_2 before the trap distribution cools from a temperature T_1 to T_2, then the atoms in the shaded region are lost without any change in the temperature.

The cooling rate τ_c^{-1} is the rate in which atoms are evaporated out of the trap. Using a detailed balance argument, the rate at which atoms are produced with an energy greater than $E_{\rm th}$ is equal to the collision rate of atoms in the part of the

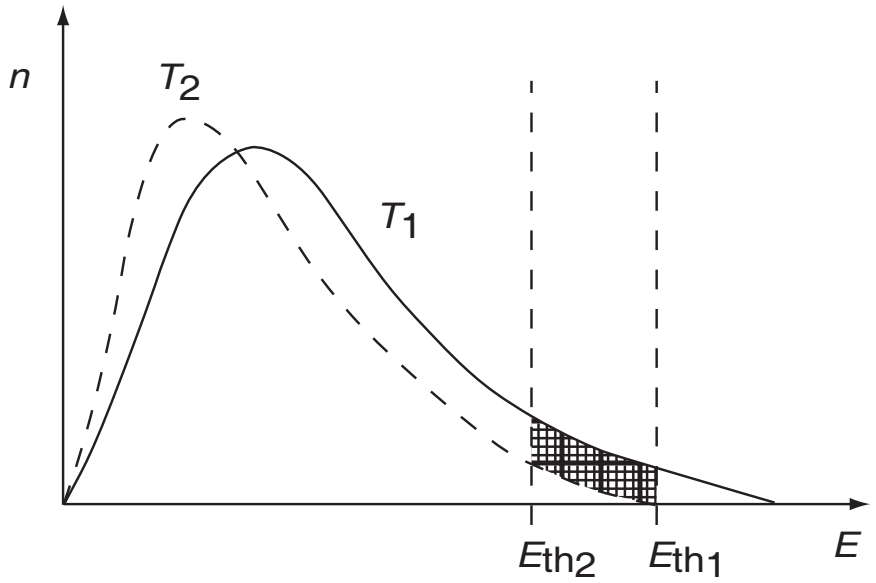

Figure 2.4: Energy distributions as the trap depth is inefficiently lowered. If a cut is taken at E_2 before the trap distribution cools from a temperature T_1 to T_2, then the atoms in the shaded region are lost without any change in the temperature

distribution with $E > E_{\rm th}$. Here we assume that a collision involving an atom in the tail of the distribution with any other atom in the distribution will most likely produce atoms with energies below $E_{\rm th}$. Therefore by calculating the faction of atoms with $E > E_{\rm th}$, the cooling rate is simply $\tau_c^{-1} = n_o g_{el} \eta e^{-\eta}$.

On the other hand, we also do not want to change $E_{\rm th}$ too slowly. $\tau_{E_{\rm th}}^{-1}$ needs to be faster than the inelastic collision rate τ_{in}^{-1} or the background gas loss rate τ_{bg}^{-1}. This minimizes both atom loss and heating.

Taking these factors into account, the rate at which the trap depth is lowered should follow the inequality

$$\tau_{in}^{-1} \text{ or } \tau_{bg}^{-1} \ll \tau_{E_{\rm th}}^{-1} \ll \tau_c^{-1} \tag{2.16}$$

to ensure that not too many atoms are lost in the evaporation process.

2.3 Evaporation Efficiency

Analysis of the efficiency of evaporation can be taken one step further. We can define an efficiency parameter χ as

$$\chi \equiv \frac{\dot{T}/T}{\dot{N}/N}. \tag{2.17}$$

χ is the change in temperature T per change in atom number N, or in other words, it is the order of magnitude decrease in temperature for a given order of magnitude loss in atom number. If $\chi > 0$, the system is cooling. If $\chi < 0$, the system is actually being heated, something we definitely do not want. In previous evaporative cooling experiments involving the alkali-metals, $\chi_{al} \sim 2$ [32], and for hydrogen, $\chi_H \sim 1.5$ [43].

To most efficiently evaporate atoms from the trap, we want to find the optimal parameters to vary the trap depth such that χ is maximized. Since the trap depth can be parameterized by η, we can therefore use Equations. 2.13 and 2.14 to find the optimal η_{opt} at a given temperature which maximizes χ ($\frac{\partial \chi}{\partial \eta}|_T = 0$). Evaporation at any other η leads to inefficient evaporation. If $\eta < \eta_{\text{opt}}$, then there is the excessive loss of low energy atoms over the trap edge. If $\eta > \eta_{\text{opt}}$, we will now have excessive loss due to inelastic collisions.

2.3.1 Dominant inelastic collisions rate

First we will only consider trap loss due to $\dot{N}_{ev}$ and $\dot{N}_{in}$ and not $\dot{N}_{bg}$. This will generally be the case in cryogenic experiments where the background gas density is negligible and will be the situation when we discuss the evaporation of trapped atomic chromium. Because $\dot{N}_{ev}$ and $\dot{N}_{in}$ are both two-body processes, the the efficiency of evaporative cooling is set by the ratio of the two rate constants g_{el}/g_{in}. Therefore χ is determined solely by the inherent physical properties of the species to be evaporated

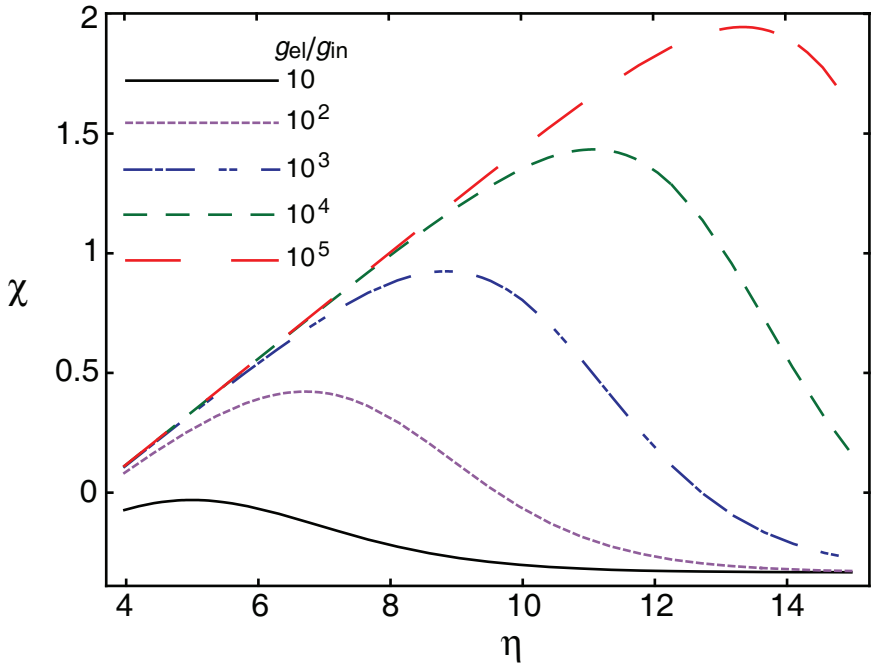

Figure 2.5: Evaporation efficiency χ when elastic and inelastic collisions are dominant. Various curves are for different ratios of g_{el} and g_{in}.

and not by the experimental parameters. Figure 2.5 shows χ as a function of η for various ratios g_{el}/g_{in}.

For a given g_{el}/g_{in} there is an optimal $\eta_{\rm opt}$ to evaporate at and a corresponding efficiency χ. Therefore experimentally, efficient evaporation would start off by setting the trap depth to $E_{\rm th} = \eta_{\rm opt} k_{\rm B} T$. As the system starts too cool, $E_{\rm th}$ is lowered to maintain the system at $\eta_{\rm opt}$. Quadratic fits for the $\eta_{\rm opt}$ and the corresponding $\chi_{\rm max}$ for a given g_{el}/g_{in} are

$$\eta_{\rm opt}(g_{el}/g_{in}) = 3.2 + 1.64\log(g_{el}/g_{in}) + 0.081(\log(g_{el}/g_{in}))^2 \quad (2.18)$$

$$\chi_{\rm max}(g_{el}/g_{in}) = -0.5 + 0.45\log(g_{el}/g_{in}) + 0.0085(\log(g_{el}/g_{in}))^2 \quad (2.19)$$

As evident from the graph and Equations. 2.19, the efficiency χ is strongly dependent on g_{el}/g_{in}. If $g_{el}/g_{in} < 10$, the inelastic rate dominates and the system can never cool. In addition, only for $g_{el}/g_{in} > 10^3$ does an order of magnitude in atom loss

correspond to more than an order of magnitude in temperature decrease. Therefore species with high inelastic rates will be inherently less efficient in evaporation than that seen in the alkali-metals.

2.3.2 Dominant background gas

If the inelastic collision rate is negligible compared to the background gas collision rate, χ is now a function of η, g_{el}, N, and τ_{bg}. Because loss due to background gas collisions is not density dependent like the inelastic loss rate, χ no longer depends solely on the inherent properties of the species to be evaporated. The efficiency is determined by the density of the sample and corresponding elastic collision rate relative to the loss rate due to background gas collisions. χ is now parameterized by the ratio of the collision rates Γ_{el}/Γ_{bg}. For this reason, very tight confinement and high atom number are essential for efficient evaporation.

Equations 2.2 and 2.4 can reexpressed in terms of Γ_{el} and Γ_{bg} by substituting the atom number N for the peak density $n_o = N/V_{\text{eff}}$, where V_{eff} is the effective volume given by $V_{\text{eff}} = 6V_o/\eta^3$ for a spherical trap in the high η limit. V_o is the physical volume of the spherical trap. Figure 2.6 shows the efficiency χ for various ratios Γ_{el}/Γ_{bg}. Just like the previous case there is an optimal η and maximum efficiency for a given ratio Γ_{el}/Γ_{bg}. Quadratic fits for the η_{opt} and the corresponding $\chi_{\max}$ for a given g_{el}/g_{in} are

$$\eta_{\text{opt}}(\Gamma_{el}/\Gamma_{bg}) = 3.36 + 0.92\log(\Gamma_{el}/\Gamma_{bg}) + 0.14(\log(\Gamma_{el}/\Gamma_{bg}))^2 \quad (2.20)$$

$$\chi_{\max}(\Gamma_{el}/\Gamma_{bg}) = -0.42 + 0.25\log(\Gamma_{el}/\Gamma_{bg}) + 0.028(\log(\Gamma_{el}/\Gamma_{bg}))^2 \quad (2.21)$$

If neither the inelastic loss rate nor background gas loss rate are negligible, then we can consider the lesser loss rate of the two as a perturbation on χ. The additional loss mechanism will tend to lower $\chi_{\max}$ and push η_{opt} to lower values.

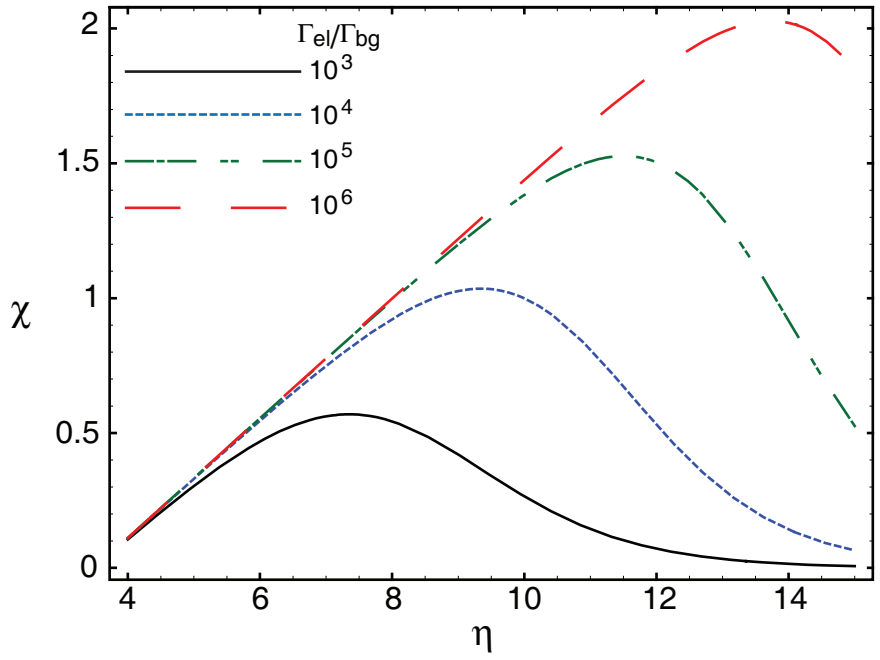

Figure 2.6: Evaporation efficiency χ when elastic collisions and loss due to background gas collisions are dominant. Various curves are for different ratios of Γ_{el} and Γ_{bg}.

2.4 Evaporation dynamics

To simulate the dynamics of evaporative cooling, we can numerically solve Equations 2.1 and 2.14 for the atom number N and temperature T as a function of time. The numerical integration requires initial starting conditions N_o and T_o and specification of how the trap depth E_{th} varies with time.

2.4.1 Equilibrium η

As mentioned before, at a constant trap depth E_{th}, the trap sample will reach an equilibrium η_{eq} set by the ratio g_{el}/g_{in}. Figure 2.7 and 2.8 shows the trap dynamics for a fixed trap depth of $E_{\text{th}} = 10.8$ K. The elastic and inelastic rate constants are $g_{el} = 10^{-11}$ cm^3/s and $g_{in} = 10^{-13}$ cm^3/s which are the measured values for Cr-Cr collisions. According to Equation 2.15 and with $g_{el}/g_{in} = 100$, the system should

reach $\eta_{\rm eq} \sim 10$.

Figure 2.7 shows the trap dynamics if the trap initially starts at $T_o = 0.5$ K for various initial N_o. Atom loss from the trap is characteristic of 2-body decay as expected, with $N \sim 10^{10}$ remaining when the system reaches thermal equilibrium. The temperature starts at 0.5 K ($\eta = 22$) and heats up to 1.2 K ($\eta = 10$) as expected. The timescale to heat up to 1.2 K depends critically on the initial atom number. For $N_o = 10^{13}$ the system takes only a few seconds whereas with $N_o = 10^{11}$ the system takes about a thousand times longer. The heating is due to the high inelastic loss rate compared to the evaporation rate, and the timescale $\tau_{\rm eq}$ to reach equilibrium should approximately follow $\tau_{\rm eq} = (n_o g_{in})^{-1}$. For $N_o = 10^{11}$, $N_o = 10^{12}$, and $N_o = 10^{13}$, $\tau_{\rm eq}$ is equal to 1000 s, 100 s, and 10 s, respectively.

If on the other hand the system is initially at a $T_o = 2$ K , it will cool to the temperature set by $\eta_{\rm eq}$. Because of the exponential dependence on η, $f(\eta)$ is extremely important to the cooling rate. At low η, trap loss is initially due to evaporation over the trap edge. At $\eta > 7$ the inelastic loss rate begins to dominate and the cooling rate slows down. Like before, the timescale to reach equilibrium is dependent on N_o. In this case, the timescale $\tau_{\rm eq}$ to reach equilibrium should approximately follow $\tau_{\rm eq} = (n_o f(\eta) g_{el})^{-1}$. For $N_o = 10^{11}$, $N_o = 10^{12}$, and $N_o = 10^{13}$, $\tau_{\rm eq}$ is equal to 250 s, 25 s, and 2.5 s, respectively.

2.4.2 Evaporation by lowering the magnetic field

One method of evaporative cooling is by uniformly lowering the depth of the magnetic trap. The wall which will adsorb the higher energy atoms from the cloud sets the trap depth, now labelled E_w (Fig. 2.9). In this evaporation method, E_w is coupled to the confinement provided by the magnetic trap. Therefore as the trap depth is

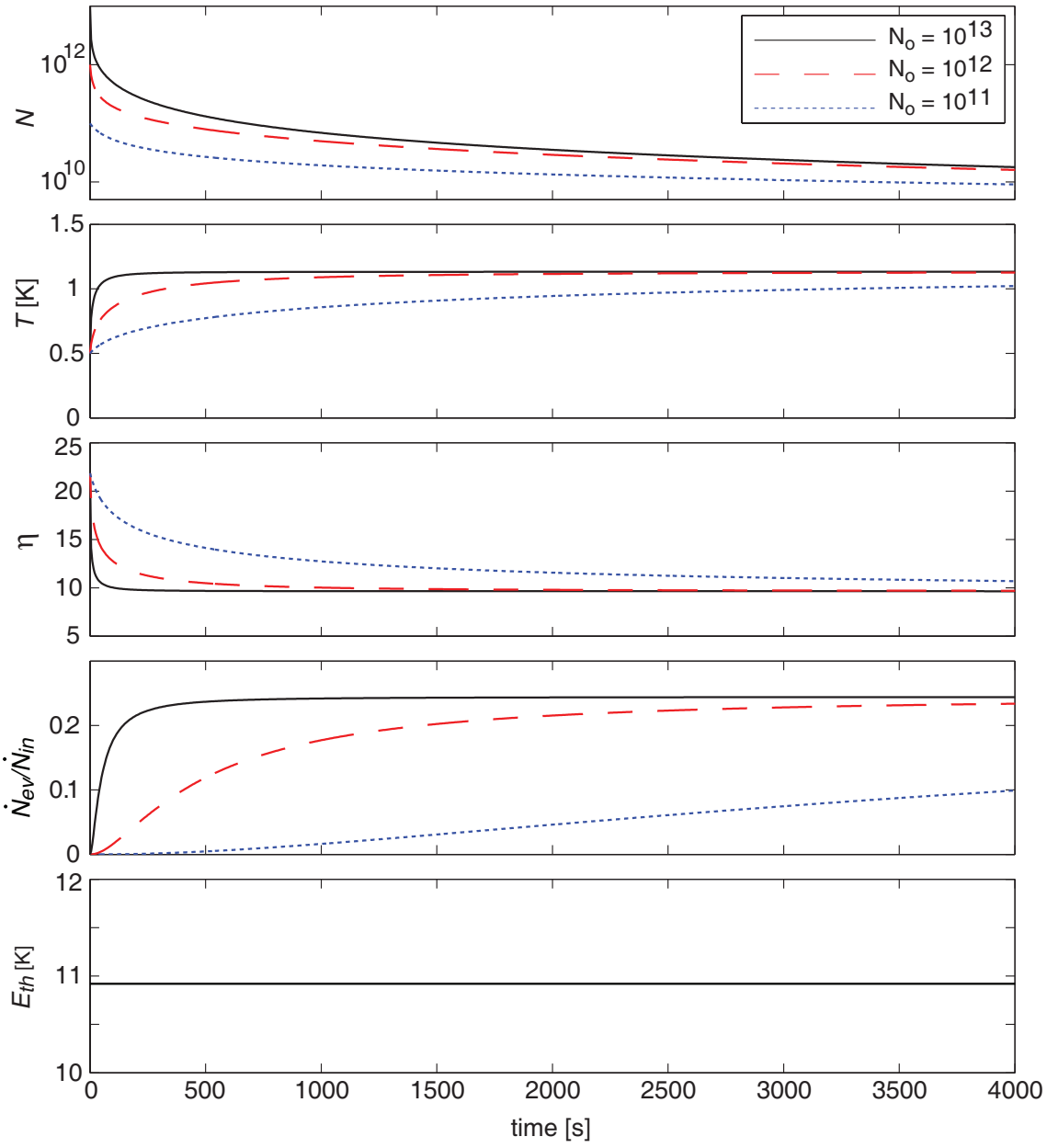

Figure 2.7: Evaporation dynamics at a fixed trap depth for an initial starting temperature $T_o = 0.5$ K and various initial atom number N_o. The elastic and inelastic rate constants are $g_{el} = 10^{-11}$ cm^3/s and $g_{in} = 10^{-13}$ cm^3/s

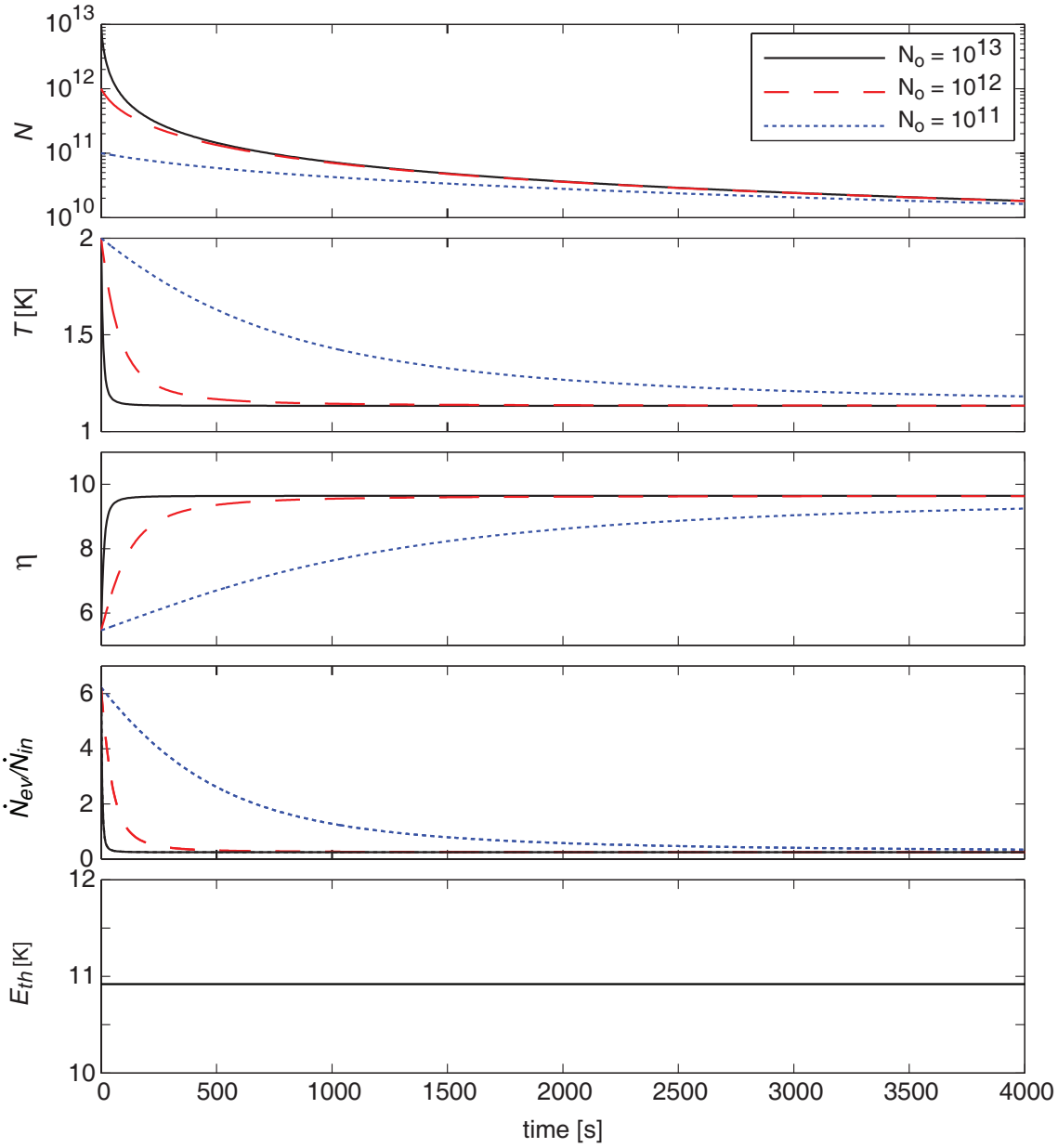

Figure 2.8: Evaporation dynamics at a fixed trap depth for an initial starting temperature $T_o = 2.0$ K and various initial atom numbers N_o. The elastic and inelastic rate constants are $g_{el} = 10^{-11}$ cm^3/s and $g_{in} = 10^{-13}$ cm^3/s

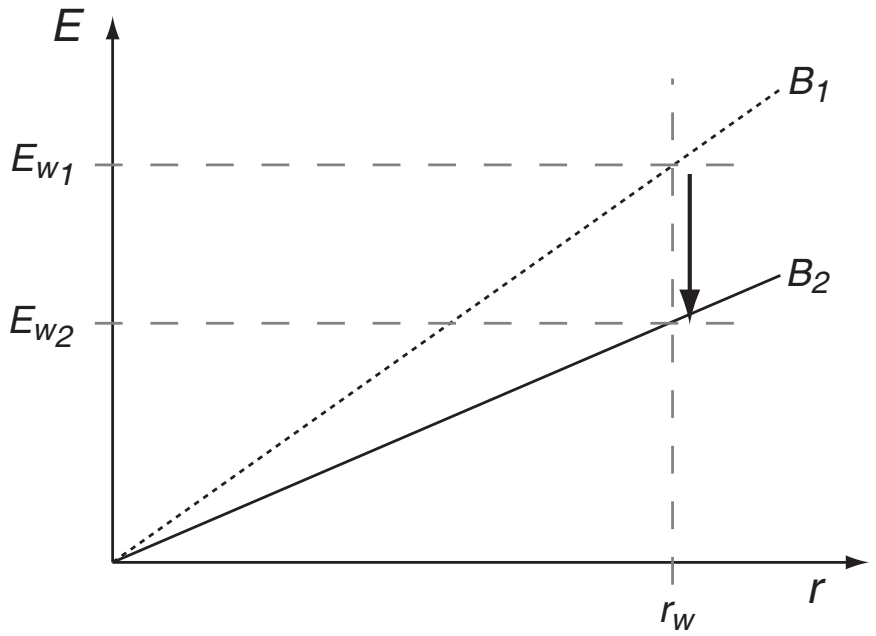

Figure 2.9: Evaporation by uniformly lowering the magnetic trap. The trap depth E_w is set by the magnetic field at the walls r_w. Evaporation is achieved by lowering the trap depth from E_{w1} to E_{w2}.

lowered, the trapped sample is cooled by evaporation over the trap edge, adiabatic expansion, and forced evaporation.

Figure 2.10 shows the dynamics for a trapped sample initially at $T_o = 1$ K. The elastic and inelastic rate constants are $g_{el} = 10^{-11}$ cm^3/s and $g_{in} = 10^{-13}$ cm^3/s. The trap depth varies as $E_w = E_o e^{-t/\tau}$, where $E_o = 10.8$ K and $\tau = 10$ s. Once $E_w = 0.78$ K, it is held constant.

At $E_w = 0.78$ K, the temperature that the sample reaches only weakly depends on N_o, indicating that cooling is dominated by adiabatic expansion. At that point forward, the system cools to the steady state condition of $T = 78$ mK ($\eta_{\rm eq} = 10$). The timescale however depends on N_o. For $N_o = 10^{11}$, the sample remains at an elevated temperature of $T = 100$ mK. The timescale to cool is so long that it seems like the system has already reached its steady state temperature and corresponding

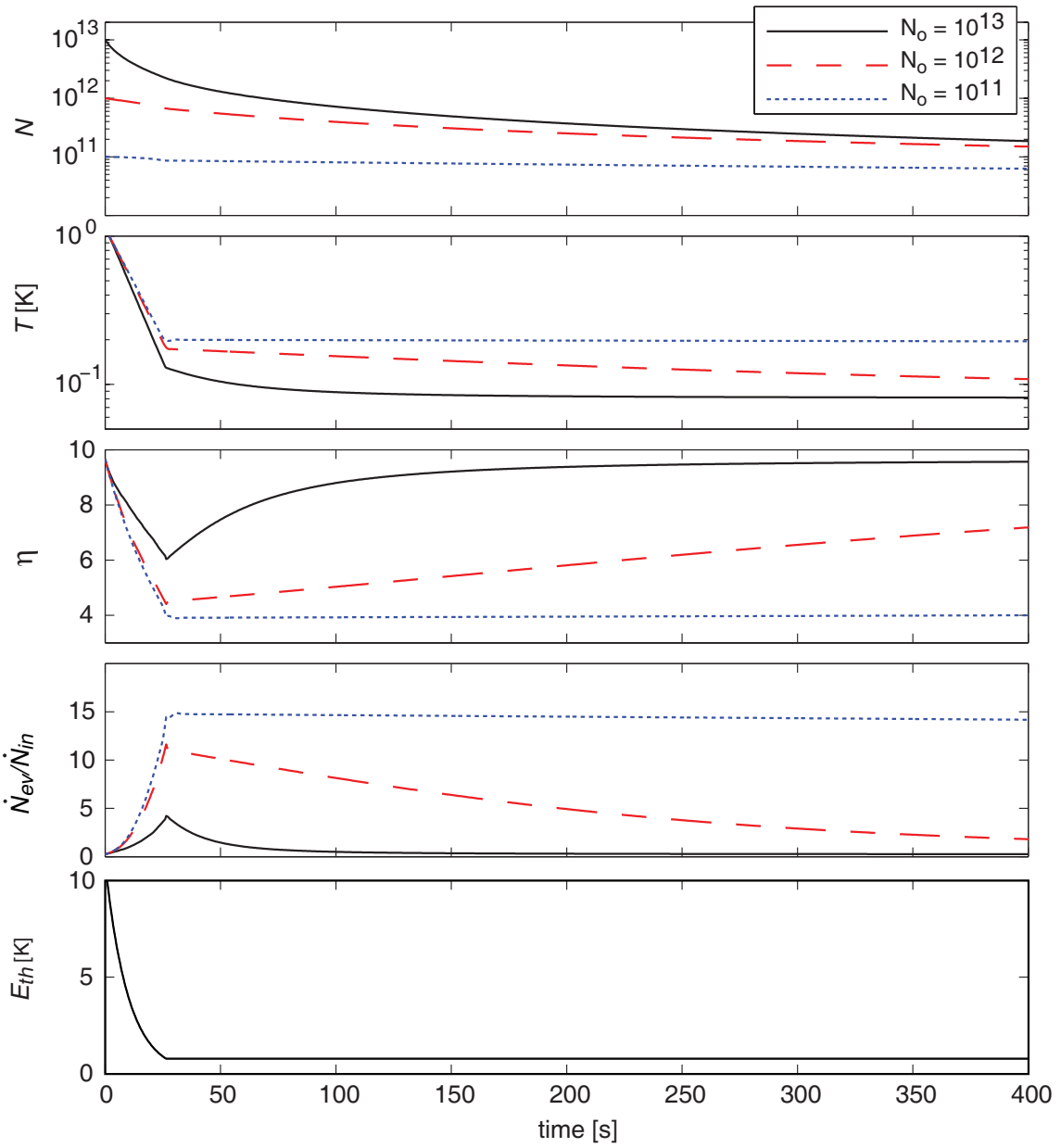

Figure 2.10: Evaporation dynamics as the magnetic trap depth is uniformly lowered for various initial atom number. N_o. The elastic and inelastic rate constants are $g_{el} = 10^{11}$ cm^3/s and $g_{in} = 10^{-13}$ cm^3/s. The trap depth varies as $E_w = E_o e^{-t/\tau}$, where $E_o = 10.8$ K and $\tau = 10$ s. The final trap depth is $E_w = 0.78$ K.

equilibrium η. This however is an artifact resulting from the low densities which are reached as the trap depth is lowered. The elastic collision rate necessary to drive evaporation is too slow to observe a change of temperature on this time scale. Samples with higher N_o do reach $T_{\rm eq}$ within the observed time window. Even though the elastic collision rate is very slow, atom loss is dominated by evaporation over the trap edge rather than inelastic collisions. This counterintuitive point is due to the low η that the system has reached after the trap depth is lowered. At $\eta = 5$, $f(\eta) \sim 0.1$ and evaporation over the trap edge is ~ 10 times larger than inelastic loss.

Figure 2.11 shows the effect of the ratio g_{el}/g_{in} on the trap dynamics. E_w is ramped down exponentially to a final trap depth of $E_w = 0.78$ K with a time constant of $\tau = 50$ s. The initial atom number is $N_o = 10^{12}$ and the elastic rate constant is $g_{el} = 10^{-10}$ cm^3/s.

For a ratio $g_{el}/g_{in} = 10$, not only is there large atom loss, the system also initially heats up. Only after $\eta < 7$ does the cooling rate from evaporation over the trap edge begin to dominate over the heating from inelastic collisions. The high loss rate from both the low η and inelastic rate combined with the decreased confinement leads to a large drop in the density, resulting in only minimal cooling to $T = 350$ mK. The phase space density decreases three orders of magnitude.

This is in contrast to the evaporation for a ratio of $g_{el}/g_{in} = 10^3$. The system cools to 70 mK, and the density only drops by a factor of 5 for the same decrease in confinement. The phase space density increases an order of magnitude. For a ratio of $g_{el}/g_{in} = 10^5$, the results are even more dramatic. The system cools to 60 mK, and the density remains constant even though the confinement is reduced. The phase space density increases by almost two orders of magnitude. In this case, evaporation is said to be in the regime of "run-away evaporation" where the elastic collision rate either

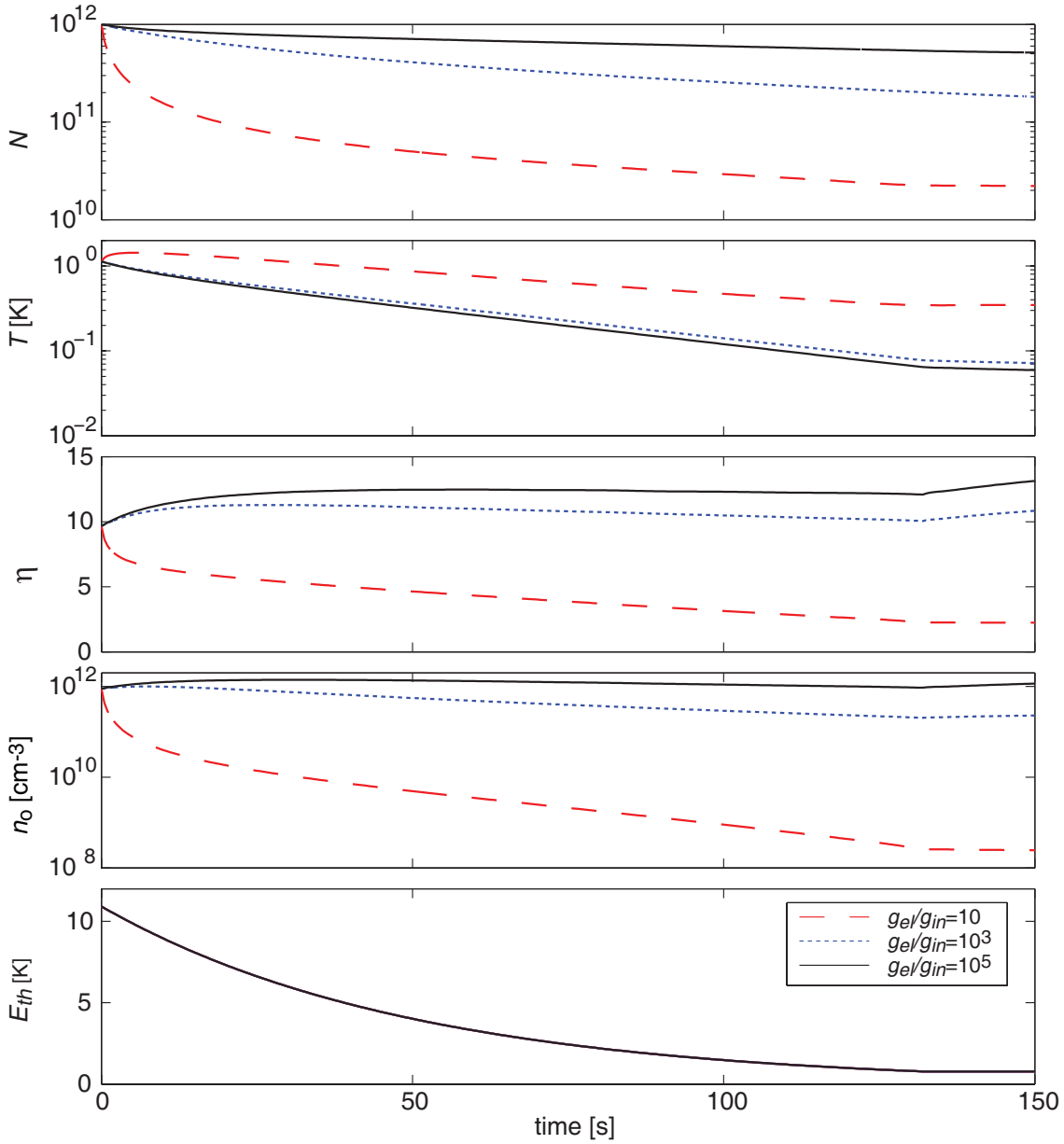

Figure 2.11: Evaporation dynamics as the magnetic trap depth is uniformly lowered for various ratios of g_{el}/g_{in}. The elastic rate constants is $g_{el} = 10^{-11}$ cm^3/s, and the trap depth varies as $E_w = E_o e^{-t/\tau}$, where $E_o = 10.8$ K and $\tau = 50$ s. The final trap depth is $E_w = 0.78$ K.

remains constant or increases. The efficiency of this evaporation trajectory is $\chi = 2.1$ which is better than the $\chi_{\max}$ calculated from Equation 2.19. The additional cooling comes from forced evaporation and adiabatic expansion which were not included in Equation 2.19.

Figure 2.12 shows the dynamics for evaporation at different rates. $N_o = 10^{12}$ and the elastic and inelastic rate constants are $g_{el} = 10^{-11}$ cm^3/s and $g_{in} = 10^{-14}$ cm^3/s. For $\tau = 10$ s, the rate that the trap depth is lowered is faster than the cooling rate. η quickly falls to 4.5 and slowly rises as the system cools to $T_{\rm eq}$. The cooling power here is inefficient because too many low energy atoms are lost to evaporation. The phase space density increases only marginally. For $\tau = 50$ s, η slowly falls to 7 and evaporation becomes more efficient. For $\tau = 200$ s, $\eta > 10$ and therefore the cooling rate is lower than for $\tau = 50$ s. The greatest phase space increase occurs for $\tau = 50$ s, indicating that there is an optimal rate to lowering the trap depth.

2.4.3 Evaporation by applying a cutoff knife

In evaporation by lowering the magnetic field, the threshold energy $E_{\rm th}$ is set by the magnetic field at the wall of the cell. By lowering the magnetic field to evaporate, both $E_{\rm th}$ and the confinement is decreased. Unless the ratio $g_{el}/g_{in} > 10^4$ as discussed in the previous section, the decrease in confinement leads to lower densities. The elastic collision rate therefore drops, and evaporation stalls.

To avoid this problem, $E_{\rm th}$ needs to be independent from the magnetic trapping fields. This is generally accomplished by applying a cutoff-knife to set $E_{\rm th}$ (Fig. 2.13). This uses the magnetic field gradient to spectroscopically distinguish the higher energy atoms in the trap. Atoms with energy higher than the $E_{\rm th}$ set by the cutoff-knife are removed from the trap by inducing transitions from the trapped states to the

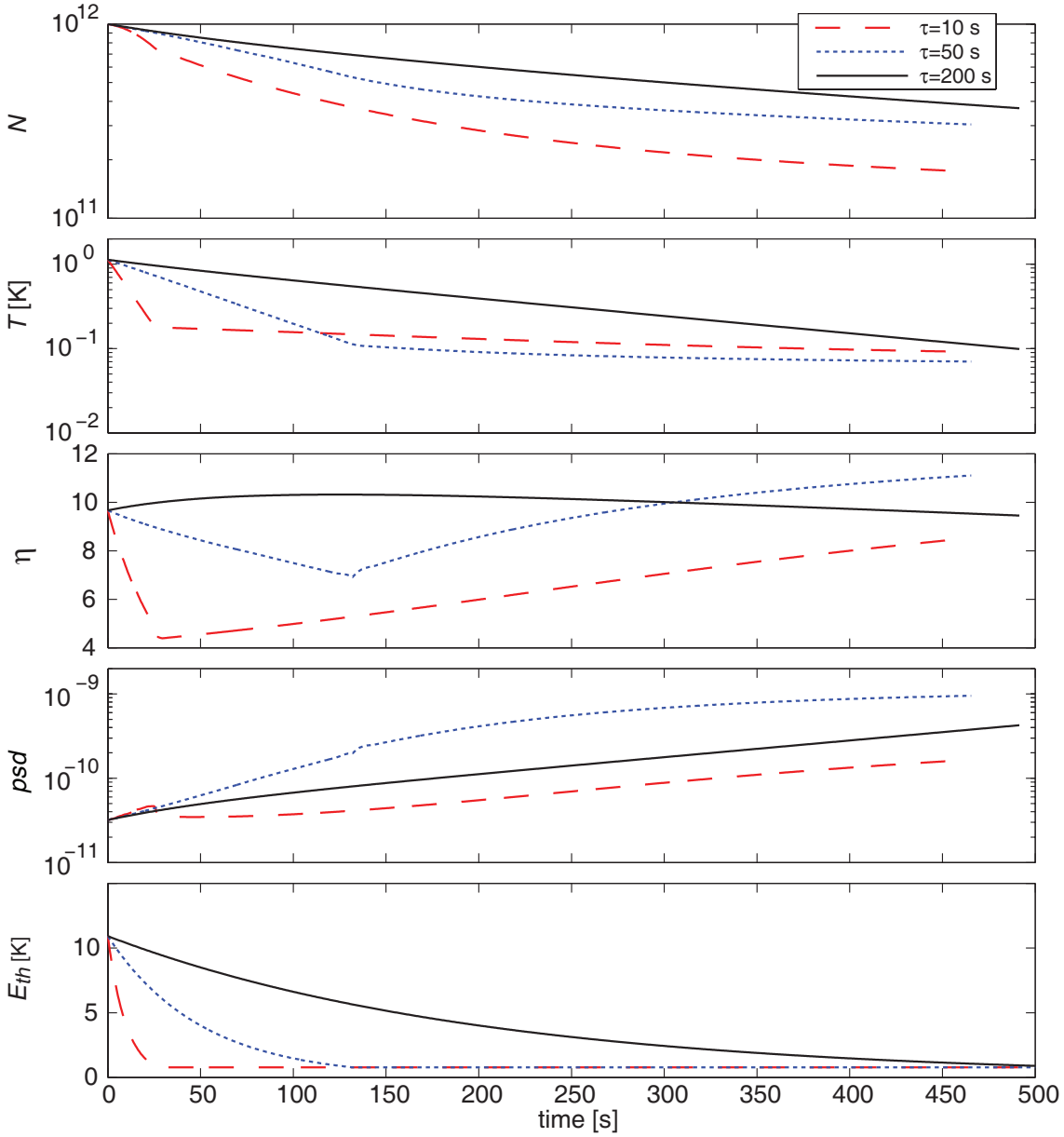

Figure 2.12: Evaporation dynamics as the magnetic trap depth is uniformly lowered at various rates. The elastic and inelastic rate constants is $g_{el} = 10^{-11}$ cm^3/s and $g_{el} = 10^{-14}$ cm^3/s. The final trap depth is $E_w = 0.78$ K.

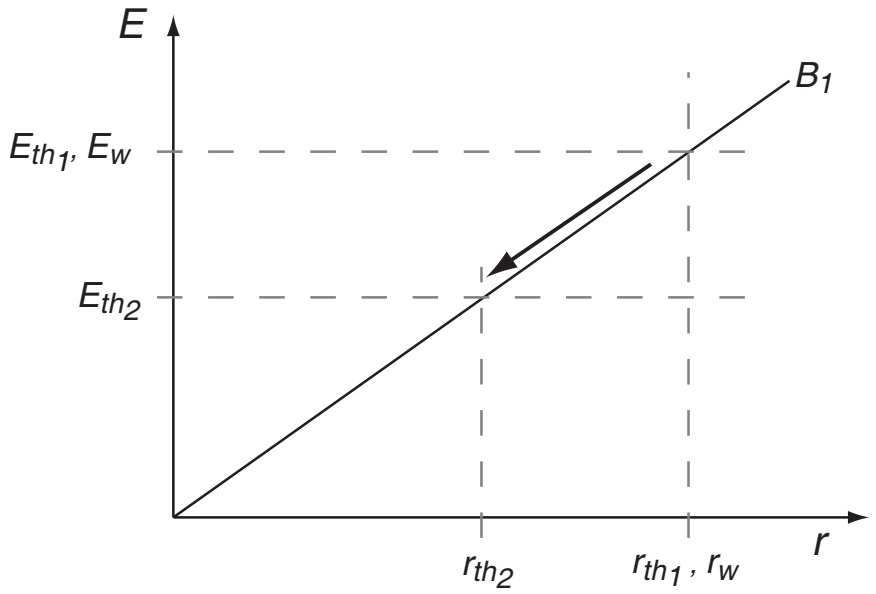

Figure 2.13: Evaporation by applying a cutoff knife. The magnetic trapping fields sets E_w and static during the evaporation process. Evaporative cooling is achieved by lowering the threshold energy from $E_{\mathrm{th}1}$ to $E_{\mathrm{th}2}$.

untrapped states using either an rf-knife or optical knife. The magnetic trapping field only sets the confinement.

If translating the trapped sample is possible, evaporation can also be achieved by moving the sample towards a surface. Atoms that come into contact with the surface are adsorbed and lost from the trap. As the atoms at the edge of the sample have higher energy than the average energy of an atom in the cloud, evaporative cooling occurs. In this case, E_{th} is set by the distance of the trap center from the adsorbing surface. Like the previous method, the magnetic trapping field only sets the confinement.

The advantage of evaporation by applying an independent E_{th} over uniformly lowering the magnetic field is shown in Figure. 2.14. Evaporation by applying a cutoff-knife is labelled the "E_{th} evaporation" while evaporation by uniformly lowering the magnetic field is labelled "E_w evaporation." For both methods, the initial trap

parameters are the same. 10^{12} atoms are initially trapped at 1 K. The elastic and inelastic rate constants are $g_{el} = 10^{-11}$ cm^3/s and $g_{in} = 10^{-13}$ cm^3/s, respectively. The trap depth is exponentially lowered from 10.8 K to a final trap depth of 0.78 K with a time constant of $\tau = 50$ s. For E_{th} evaporation the magnetic trapping field remains unchanged and is equal to the initial field of E_w evaporation.

At a trap depth of 0.78 K, the E_{th} evaporation method reaches a temperature of 150 mK while the E_w evaporation method reaches only 250 mK. The remarkable difference between the two methods is the increasing density associated with E_{th} evaporation. With E_w evaporation, the density actually decreases an order of magnitude. The corresponding phase space density remains constant in contrast to E_{th} evaporation which increases almost two orders of magnitude. Unfortunately, the higher densities using E_{th} evaporation translates into higher inelastic loss. Only $\sim 10^9$ atoms remain while there is still $\sim 10^{11}$ atoms remaining using E_w evaporation.

Evaporation can also be achieved by a combination of applying a cutoff knife and lowering of the magnetic field. This is generally needed when during evaporation the densities reach $> 10^{14}$ cm^{-3}. At these high densities, three-body recombination becomes significant, requiring the magnetic field confinement to be lowered [41].

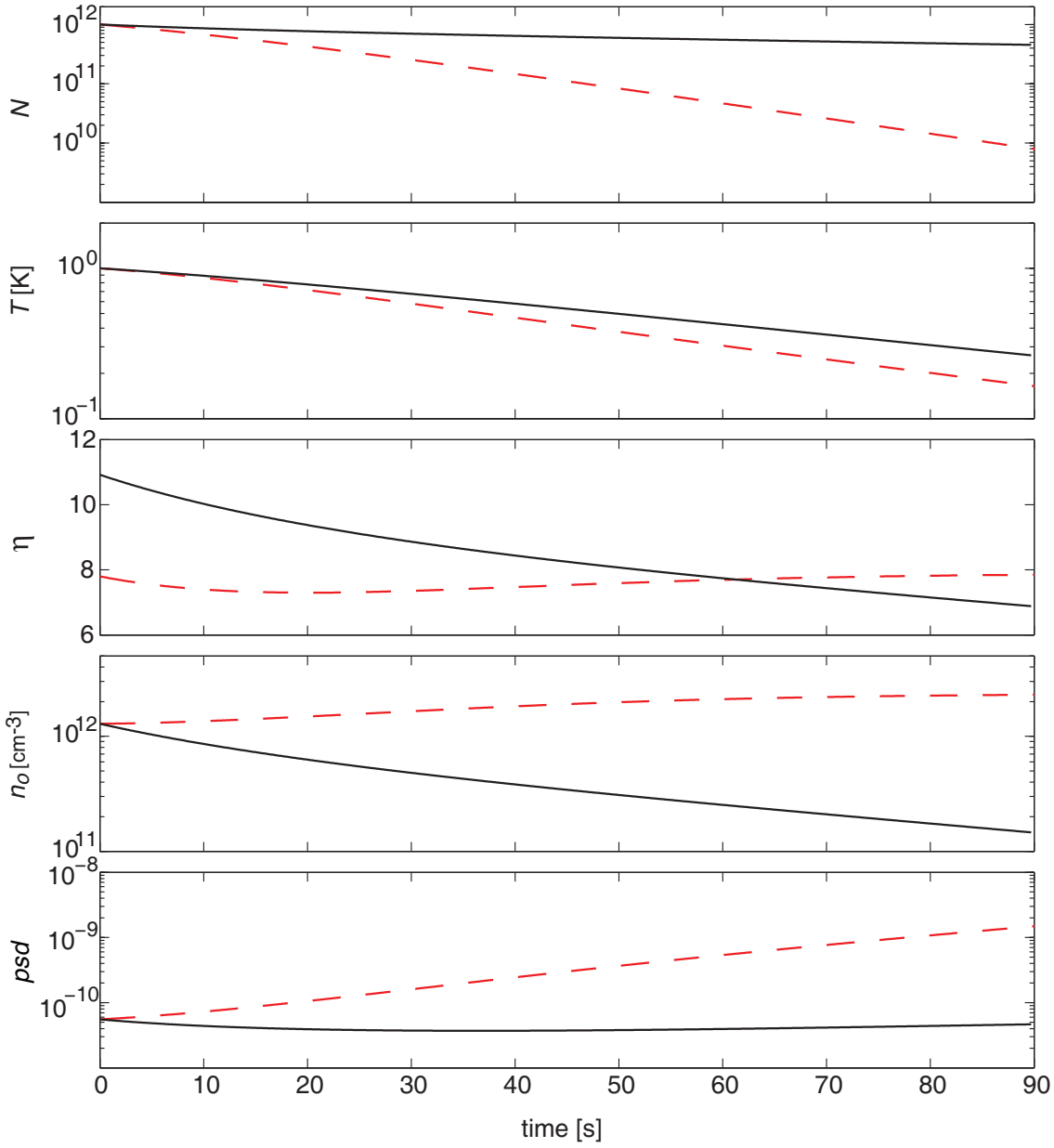

Figure 2.14: Comparison of evaporation by uniformly lowering the magnetic field versus applying a cutoff-knife. The solid line is E_{th} evaporation, and the dashed line is E_w evaporation. The elastic and inelastic rate constants is $g_{el} = 10^{-11}$ cm^3/s and $g_{el} = 10^{-13}$ cm^3/s. The trap depth is exponentially lowered from 10.8 K to a final trap depth of 0.78 K with a time constant of $\tau = 50$ s

Chapter 3

Cr-Cr collisions: Reanalysis

In 2002, atomic chromium was buffer gas cooled and magnetically trapped [26]. Evaporative cooling was then implemented to try to cool the sample to quantum degeneracy where one might be able to study the properties of Fermi-degeneracy or dipolar gases. Unfortunately, evaporation stalled at $T = 2$ mK [44]. The measured inelastic collision rate increased four orders of magnitude from 1 K down to 5 mK, eventually becoming larger than the elastic collision rate. These measurements, however, disagreed with theoretical calculations of the elastic and inelastic collision rates [45, 46]. In this chapter, we use the the evaporative cooling model presented in Chapter 2 to reanalyze the data from these measurements. By looking at the evaporative cooling dynamics, we are able to understand the experimental parameters that led to the measured values and infer elastic and inelastic collision rate constants which agree with theory.

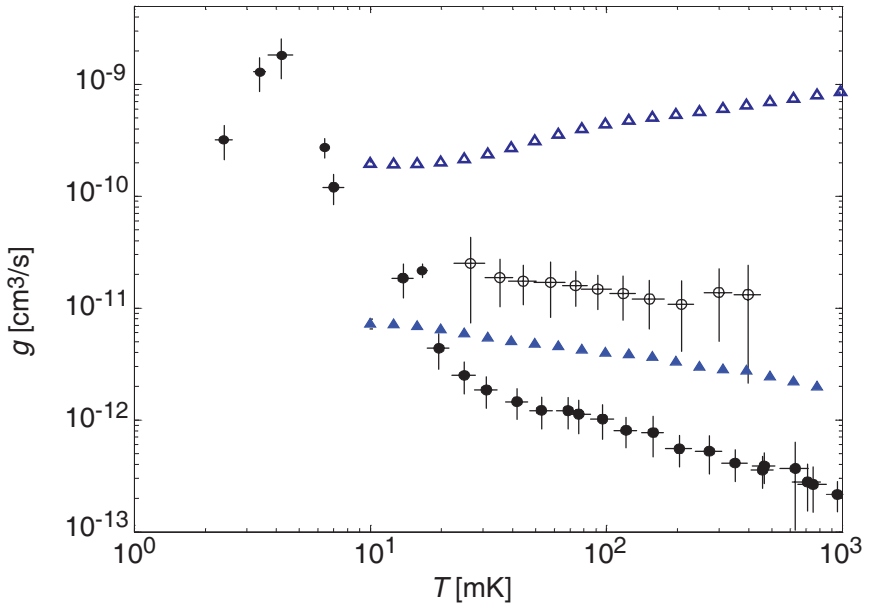

Figure 3.1: Measured and theoretical collision rate constants between two $|S_{1,2} = 3, m_{S1,2} = +3\rangle$ chromium atoms. The open circles are the measured elastic rate constants. The solid circles are the measured inelastic rate constants. The open triangles are the theoretical elastic rate constants. The closed triangles are the theoretical inelastic rate constants. The measured rate constants are taken from Reference [44]. The theoretical rate constants are taken from Reference [45, 46].

3.1 Measured and theoretical collision rates

Figure 3.1 shows the measured elastic and inelastic collision rate constants as a function of temperature [26, 44]. Also plotted are the theoretically calculated rate constants by Pavloic *et al.* [45, 46]. The discrepancy between measured and theoretical rate constants is dramatic both in value and functional form. The measured inelastic rate skyrockets four orders of magnitude as the temperature is lowered from 1 K down to 2 mK. Because many partial waves contribute to the collisional dynamics for this temperature range, the possibility of shape resonances has been suggested as an explanation.

Unfortunately, theoretical calculations of dipolar relaxation taking into account

all significant partial waves are monotonic over this temperature range. The theoretical values are based on scattering calculations between chromium atoms in the $|S_{1,2} = 3, m_{S1,2} = +3\rangle$ state. The corresponding $|S = 6, M_S = 6, m_{s1} = +3, m_{s2} = +3\rangle$ molecular potential used in the calculation is constructed using the magnetic field positions from measured Feshbach resonances in an ultracold gas of chromium atoms [47]. The calculations assume inelastic loss is due to dipolar relaxation where the spin of the two chromium atoms are coupled to the orbital angular momentum of the colliding pair.

The measured collision rate constants were obtained by first trapping a cloud of atomic chromium at $\sim$ 1 K and then evaporatively cooling the sample to lower temperatures. At the colder temperatures, the elastic collision rate was measured by optically pumping atoms selectively out of one part of the thermal distribution and observing the re-equilibration of the atoms as show in Figure 3.2a. The rate at which sample returns to a thermal distribution is proportional to the elastic collision rate. The inelastic collision rate constant was measured by observing trap loss. Because the decay of the trap sample fit well to the expected functional form for two-body loss, trap loss was attributed to Cr-Cr collision induced dipolar relaxation (Fig. 3.2b).

In addition, after the trap depth was lowered and the atoms were evaporatively cooled, the temperature was observed to not to change within the signal to noise of the experiment. The measured temperature was assumed to be the equilibrium temperature $T_{\rm eq}$ set by the ratio g_{el}/g_{in}. Figure 3.3 shows the measured equilibrium η as a function of temperature. The decrease in $\eta_{\rm eq}$ at colder temperatures is consistent with the measured decrease in the ratio g_{el}/g_{in}.

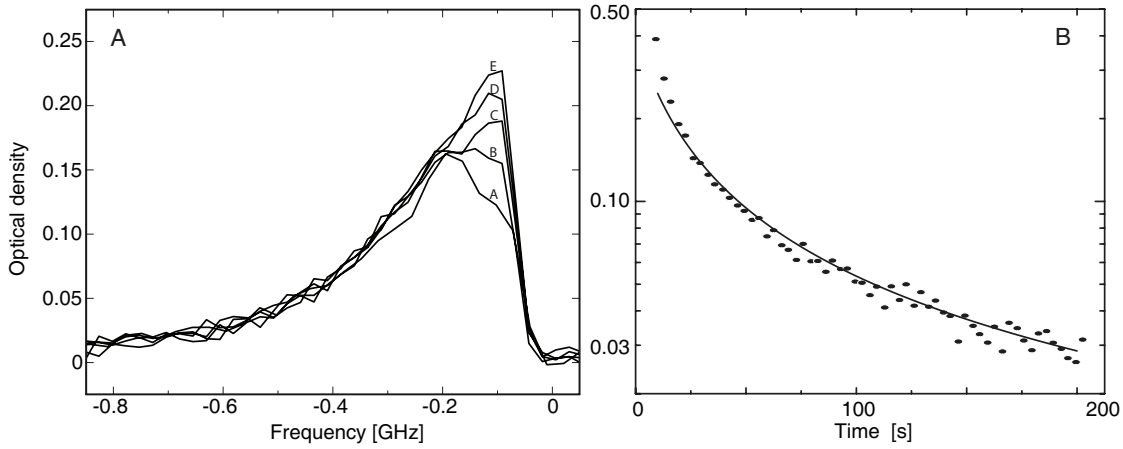

Figure 3.2: Experimental methods in which the measured collision rate constants were extracted. A) Elastic collision rate. Spectra taken after optically pumping atoms out of the trap, showing a return to a thermal distribution due to elastic collisions. Successive spectra A-E were taken at 1 s intervals following the optical pumping. B) Inelastic collision rate. Trap loss fit to the expected functional form for two-body loss. Graphs were taken from Reference [48].

3.2 Cr evaporation dynamics

The reason for the discrepancy between the measured and theoretical rate constants has thus far been unexplained. By simulating the evaporation dynamics using the model described in Chapter 2 we can understand the experimental conditions in which the measured rate constants where taken.

3.2.1 Simulation

In the experiment, 6×10^{11} Cr atoms were initially loaded into a $E_w = 9$ K deep magnetic trap at a temperature of $T = 700$ mK. The magnetic trap depth was then uniformly lowered at an exponential rate with $\tau = 4$ s. The 4 s time constant was set by the L/R time of the inductance of the superconducting magnet and the resistor bank circuit. Once the trap depth reached a predetermined value, the trap depth was held constant. At this trap depth, the temperature of the cloud and the elastic and

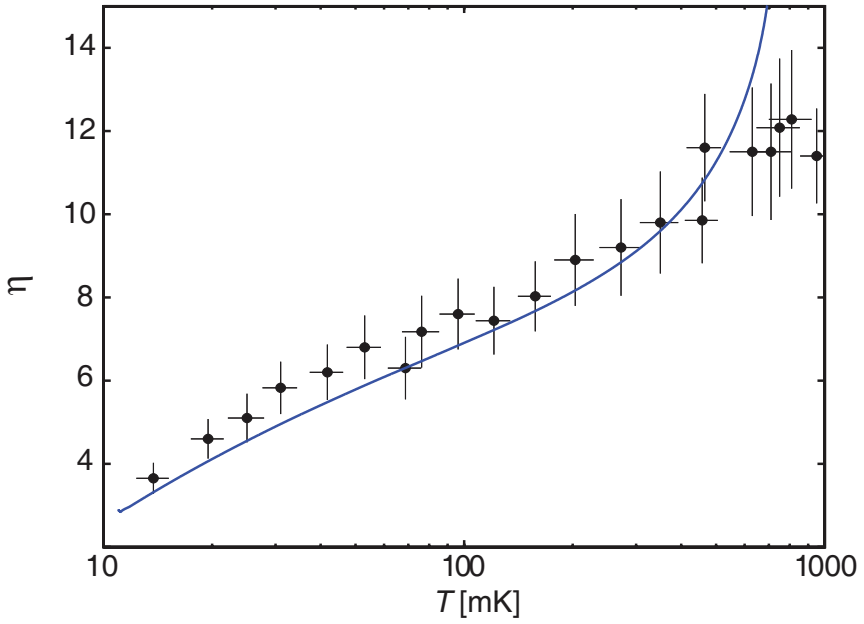

Figure 3.3: Measured η as a function of temperature. The solid circles are the measured η after the system has been evaporatively cooled to a trap depth E_w. Data taken from Reference [48]. The solid line is the η that would be measured generated from the evaporation model assuming $g_{el} = 2.15 \times 10^{-10}$ cm^3/s and $g_{in} = 1.36 \times 10^{-12}$ cm^3/s.

inelastic collision rates were measured. The experiment was repeated at lower and lower final trap depths.

Figure 3.4 shows the evaporation dynamics for the specified experimental parameters. The average measured values of $g_{el} = 10^{-11}$ cm^3/s and $g_{in} = 10^{-13}$ cm^3/s are used for the elastic and inelastic collision rates. The final trap depth is $E_w = 0.16$ K.

3.2.2 Two-body loss and equilibrium η

From the simulations, we see that the fast decrease in trap depth quickly leads to a low density of $n_o \sim 10^{10}$ cm^{-3}. Because the collision rate is very slow, the system does not reach its equilibrium temperature $T_{\rm eq}$ within the 300 s window of the simulation. The temperature is constant at ~ 40 mK. Only with larger initial atom number and corresponding higher collision rates does the system cool to $T_{\rm eq} = 16$ mK ($\eta_{eq} = 10$)

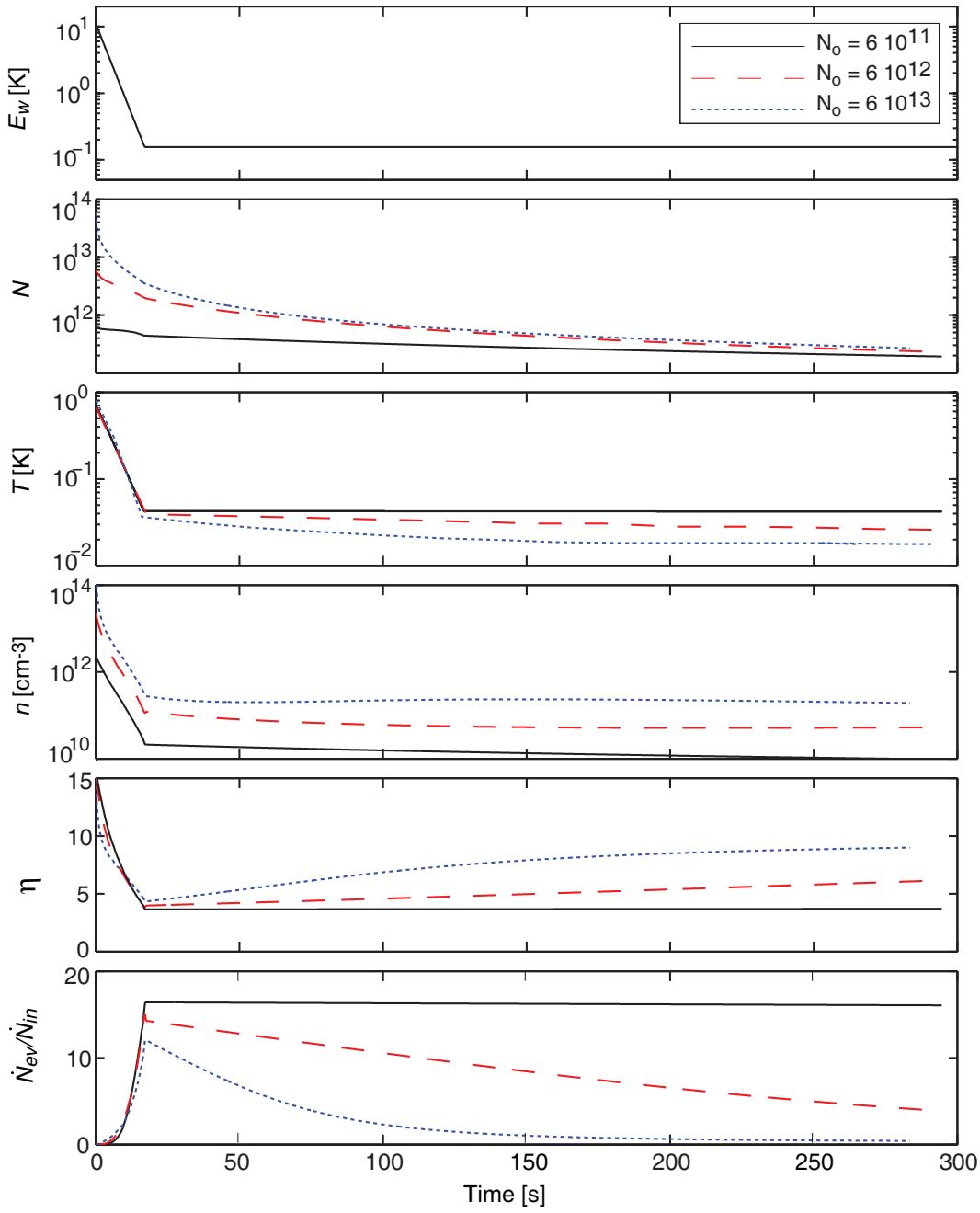

Figure 3.4: Evaporation dynamics of magnetically trapped Cr. The elastic and inelastic rate constants are $g_{el} = 10^{11}$ cm^3/s and $g_{in} = 10^{-13}$ cm^3/s. The trap depth varies as $E_w = E_o e^{-t/\tau}$, where $E_o = 10.8$ K and $\tau = 4$ s. The final trap depth is $E_w = 0.16$ K.

within the 300 s window. Therefore, the temperatures that are measured in the experiments at these final trap depths are not necessarily the steady-state temperature $T_{\rm eq}$. The system has not reached the $\eta_{\rm eq}$ set by the ratio g_{el}/g_{in} within the measurement period. Low signal-to-noise resulting from the low densities would prevent experimentally observing any change in temperature over a reasonable timescale as the system approached $T_{\rm eq}$.

Figure 3.5 shows the dynamics as the trap depth is lowered to different final values. The elastic and inelastic rate constants used in the simulation are $g_{el} = 2.15 \times 10^{-10}$ cm^3/s and $g_{in} = 1.36 \times 10^{-12}$ cm^3/s ($\eta_{eq} = 10$). As the trap depth is lowered, the η that the system reaches also decreases. This simply reflects that the trap depth is being lowered too quickly for the system to cool to $T_{\rm eq}$. The solid line in Figure 3.3 is the η that would be measured after the the system has been evaporatively cooled to a trap depth E_w. Not only does the curve reproduce the functional form of the measured η, the values are within the error bars. This confirms that the measured values for η are not necessarily $\eta_{\rm eq}$. The measured decrease in η as the temperature of the system was lowered is an artifact of evaporation procedure and is not a reflection of a decreasing ratio of g_{el}/g_{in}.

In addition, at the low η's reached in the experiment, atom loss is actually dominated by $\dot{N}_{ev}$ rather than $\dot{N}_{in}$. For $N_o = 6 \times 10^{11}$ atoms, there is ~ 16 atoms lost due to evaporation over the trap edge for every one atom lost due to inelastic collisions. Therefore, attributing the 2-body decay constant g_{2b} solely to inelastic collisions is not accurate. The measured g_{2b} is a combination of inelastic loss and evaporation over the trap edge. Figure 3.6 shows the fraction of two-body loss which is due to evaporation over the trap edge for various ratios of g_{el}/g_{in}.

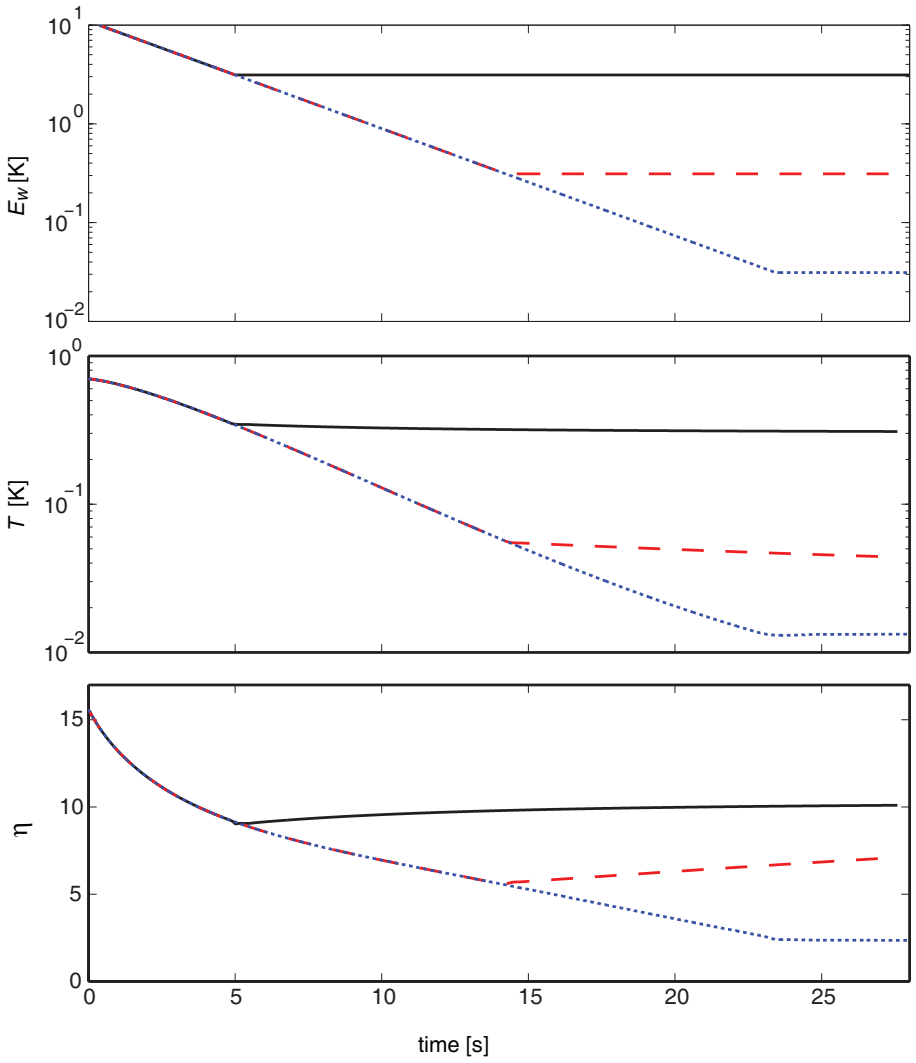

Figure 3.5: Decrease in η after evaporation to various trap depths. The elastic and inelastic rate constants are $g_{el} = 2.15 \times 10^{-10}$ cm^3/s and $g_{in} = 1.36 \times 10^{-12}$ cm^3/s ($\eta_{eq} = 10$). The trap depth varies as $E_w = E_o e^{-t/\tau}$, where $E_o = 10.8$ K and $\tau = 4$ s. The final trap depths are $E_w = 3.1, 0.31, 0.031$ K.

3.3 Inelastic rates

According to Equation 2.13 trap loss at a constant trap depth can be expressed as

$$\dot{N} = \dot{N}_{ev} + \dot{N}_{in} \propto (f(\eta) g_{el} + g_{in}) N^2. \tag{3.1}$$

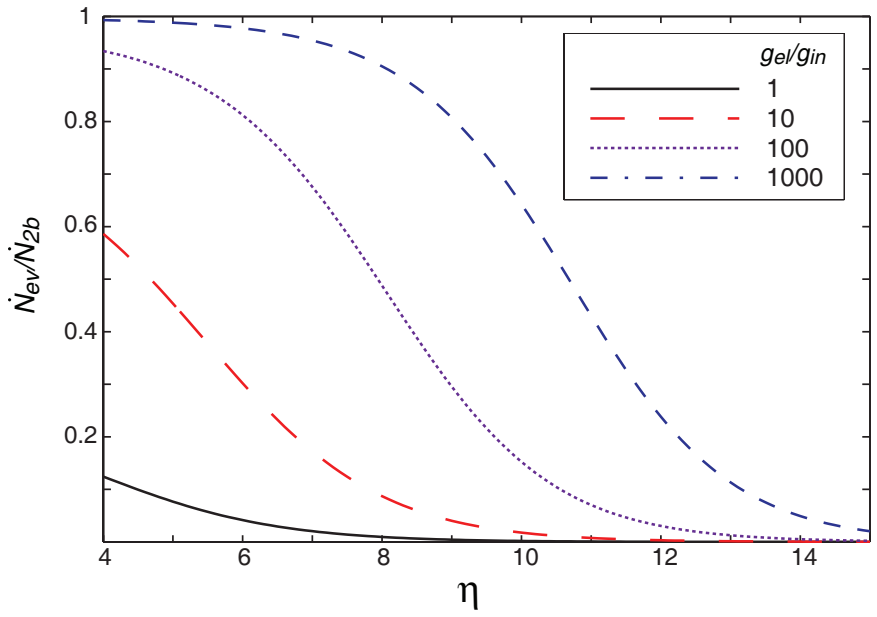

Figure 3.6: Fraction of two-body loss due to evaporation over the trap edge.

Therefore the measured two-body loss rate is equal to $g_{2b} = f(\eta)g_{el} + g_{in}$. The fraction due to inelastic collisions is then $g_{in} = g_{2b} - f(\eta)g_{el}$. To determine the inelastic collision rate, we need both the η at which the two-body measurement was taken and the corresponding elastic rate constant at that given temperature.

Figure 3.7 shows the inelastic collision rates for the measured g_{2b}, g_{el}, and η. For temperatures above 20 mK, g_{in} is not increasing at lower temperatures as previously thought. It is constant at a level of $\sim 10^{-13}$ cm^3/s.

Unfortunately the inelastic rates below 20 mK cannot be determined because elastic measurements were not made for those temperatures. Assuming a constant $g_{el} \sim 10^{-11}$ through this temperature range cannot explain the large g_{2b} ($> 10^{-11}$ cm^3/s) that were measured. Both g_{el} and g_{in} would have to increase dramatically in this temperature range to account for those measurements. Furthermore, the theoretical values still disagree with g_{in} and most notably g_{el}.

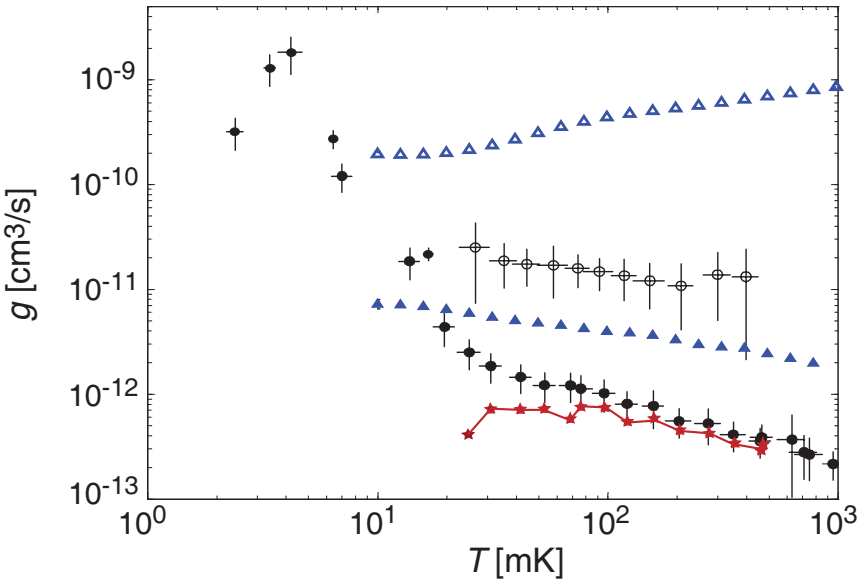

Figure 3.7: Modified chromium inelastic collision rates. The stars are the modified inelastic rates. The solid circles are the measured two-body loss rates, and the open circles are the measured elastic collision rates. The solid triangles are the theoretical inelastic rates, and the open triangles are the theoretical elastic rates.

3.4 Inferred elastic and inelastic rates

Though the simulation of the evaporation dynamics revealed a clearer picture of the relationship between elastic and inelastic processes during evaporation, the discrepancy with theoretically predicted values is still an issue. As mentioned before, the theoretical values are calculated using the most accurate to date $|S = 6, M_S = 6, m_{s1} = +3, m_{s2} = +3\rangle$ molecular potential, based on the identification of a series of measured magnetic Feshbach resonances in an ultracold sample of chromium atoms. Because this method has been shown previously to be accurate at determining the molecular potential of the alkali-metals [10, 7], there is less ambiguity in the theoretical values compared to the measured values of the collision rates.

The analysis based on the simulations thus far has not involved the elastic collision rate constant, taking it only as an input parameter. Because of the discrepancy with

the theoretical values, the misinterpretation of the inelastic data casts some doubt on the elastic collision rate measurements. Modifications to the elastic collision data would also affect the inelastic data. Therefore resolving the discrepancy between theory and experiment requires a experimental method which is not based on the previous measurement of g_{el} and g_{in}.

Fortunately, data for this independent method already exists. In evaporatively cooling chromium, the experiment measured both the temperature and number of chromium atoms as a function of the trap depth [48]. Since $\dot{N}$ and $\dot{T}$ are both functions of g_{el} and g_{in}, the dynamical evolution of N and T is solely determined by the collision rate constants and the experimental trap parameters. Therefore we are able to use the evaporative cooling model along with the evaporative cooling data to independently infer an elastic and inelastic collision rate constants.

Figure 3.8 plots the measured density and temperature after being evaporatively cooled to various final trap depths. At the initial trap depth of 9 K, $n_o = 1.8 \times 10^{12}$ cm^{-3} and $T_o = 700$ mK. The trap depth was then lowered exponentially with a time constant of $\tau = 4$ s. By running the evaporation model and numerically solving Equations 2.13 and 2.14 for n_o and T as a function of trap depth, we can perform a least squares fit for the values of g_{el} and g_{in} which would best reproduce the measured evaporation data. In this analysis we assume that both g_{el} and g_{in} are constant though the 20 mK-1K temperature range. Even though there may be some functional dependence on temperature, both the measured and theoretical collision rates show only a weak dependence. The theoretical values change only by a factor of ~ 3 through this temperature range.

A least-squares fit for the data presented in Figure 3.8 with g_{el} and g_{in} as fit parameters yields collision rates of $g_{el} = 2.15(+2.5, -1.2) \times 10^{-10}$ cm^3/s and $g_{in} =$

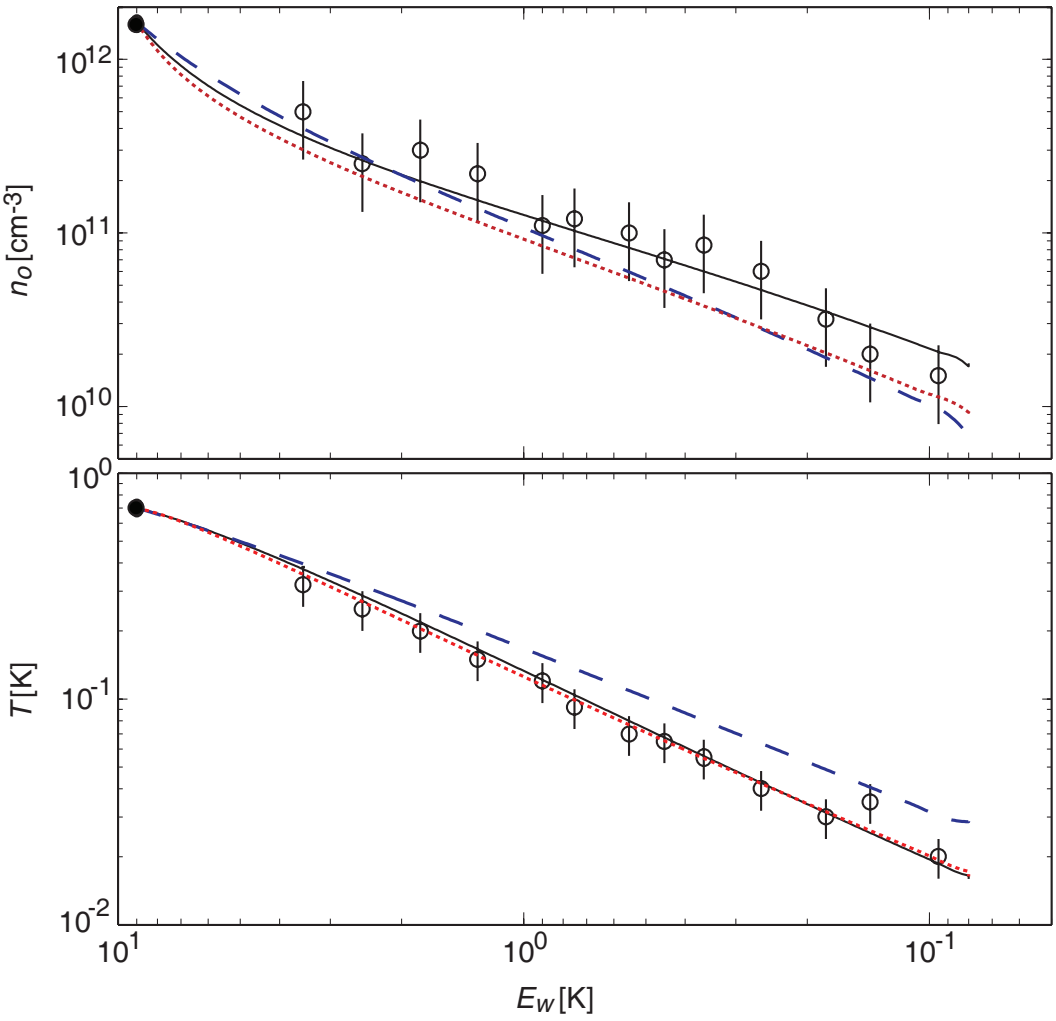

Figure 3.8: Least-squares fit to the Cr evaporation data. The solid circles are the initial conditions. The open circles are the measured values for n_o and T after being evaporatively cooled to E_w. The solid line is a least squares fit for the elastic and inelastic collision rates yielding $g_{el} = 2.15 \times 10^{-10}$ cm^3/s and $g_{in} = 1.36 \times 10^{-12}$ cm^3/s. The dotted line is evaporation using the theoretically predicted values. The dashed line is evaporation using the experimentally measured values.

$1.36(+1.2, -0.7) \times 10^{-12}$ cm^3/s with $\chi^2_{\text{fit}} = 8.1$. If we use the theoretically predicted values for g_{el} and g_{in} which includes the temperature dependence, $\chi^2_{\text{theory}} = 10.7$. Taking it one step further, using the average experimentally measured values $g_{el} = 1.5 \times 10^{-11}$ cm^3/s and $g_{in} = 7 \times 10^{-13}$ cm^3/s, $\chi^2_{\text{exp}} = 66.3$.

The result which stands out the most from this fit is the elastic collision rate constant. The fitted value for g_{el} is more than an order of magnitude larger than the measured value and agrees with theoretically predicted values. As seen in Figure 3.8, g_{el} must be this large to account for the amount of cooling that was experimentally measured. With g_{el} tens times slower, cooling due to the evaporation rate over the trap edge is too slow compared to the rate at which the trap depth is lowered.

The fitted value for g_{in} is slightly lower than the theoretically predicted values. It is important to note that the theoretical values presented here have been thermally averaged over the distribution of collision energies, however it has not been averaged over the distribution of magnetic fields. The theoretical values are the inelastic rate constants at a magnetic field $3B_{\text{max}}/2\eta$, which is the magnetic field at which a two-body collision is most likely to occur. Comparing the fitted value for g_{in} to the experimentally measured value is uninformative because the experimental values are dependent on knowing the elastic collision rates. The fitted value of g_{el} now puts into question the experimental method which was used to measure the elastic collision rate.

3.5 Conclusions

Figure 3.9 shows a summary of the inferred collision rate constants based on the evaporation model compared to the theoretical and previously measured rates constants. In the current analysis, the fit to the evaporation data assumes a constant collision

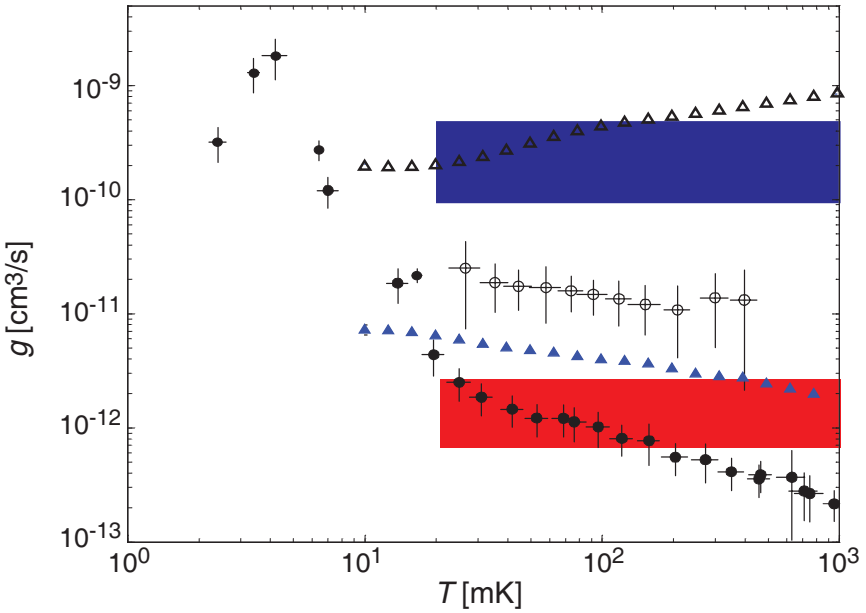

Figure 3.9: Inferred chromium collision rates. The darker shaded region represents the inferred elastic collision rate from a fit of the evaporation data show in Figure 3.8. The lighter shaded region represents the inferred inelastic collision rate. The solid circles are the measured two-body loss rates, and the open circles are the measured elastic collision rates. The solid triangles are the theoretical inelastic rates, and the open triangles are the theoretical elastic rates.

rate through this temperature range. However, the analysis can be easily extended to include a temperature dependence if a functional form is known. By comparing the resulting χ^2, we can determine if a particular model better describes the evaporation data. In addition, the the inferred rates are only valid for the temperature range between 20 mK and 1 K because reliable evaporation data was only taken for temperatures above 20 mK. Even though we cannot say with certainty, the large two-body rates ($> 10^{-10}$ cm^3/s) that were measured below 20 mK is likely due to evaporation over the trap edge, which now can be accounted for by both the elastic collision rate and low η at which the measurement was performed.

An even bigger issue, however, is the reason for the discrepancy between the inferred rate constants from the experimentally measured values, especially the elastic

collision rate constant. From the evaporation model, we have a good understanding of how to determine the inelastic collision rate. Unfortunately, extracting this value from two-body measurements requires knowing the elastic collision rates. The optical-pumping experiments to determine the the elastic collision rate relied on measuring the timescale for the atoms to return to a thermal distribution. This time scale is set by a combination of the elastic collision rate, the number of collisions required to repopulate the orbits of the atoms which were optically pumped away, and the density of the particular atoms which would mostly likely repopulate the missing orbits. Reinterpretation or reanalysis of this data is necessary to understand why the elastic collision rate extracted from it is an order of magnitude lower than what is expected.

In addition, further experiments should be conducted to resolve the discrepancy for the collision rates below 20 mK. This can easily be done by measuring the density and temperature as a function of trap depth and fitting for g_{el} and g_{in}. Another method of determining the collision rates is to measure the two-body loss rate at a given temperature as a function of η since $g_{2b} = g_{in} + f(\eta)g_{el}$. These two methods would avoid any confusion associated with determining the elastic collision rate from optical-pumping experiments.

Chapter 4

Manganese

Two advantages of buffer gas loading over laser cooling are the ability to magnetically trap a variety of atoms independent of its internal structure and the ability to simultaneously load mixtures of atoms and/or molecules. In this chapter, we describe the first magnetic trapping of atomic manganese, an atom quite different from the alkali-metals. Mn is a transition metal with a large magnetic moment of $5\mu_{\mathrm{B}}$, and it is at the center of a longstanding debate on the magnetic properties of transition metal clusters. By studying the collisional dynamics of different hyperfine states at 500 mK, we gain information on the internuclear potential of Mn dimers which should be useful in determining the nature of their magnetic coupling. In addition, we demonstrate the first multi-species trapping of buffer gas loaded samples with the simultaneous trapping of Mn and Cr. Beyond this general demonstration, a Mn-Cr mixture does have particular properties of interest. A binary mixture of manganese and chromium in the quantum degenerate state could have significant dipolar effects [49]. Furthermore, it might be possible via a Feshbach resonance or photoassociation to produce an electric dipolar molecule with very high magnetic moment – an interesting species for studies of dipolar effects in quantum matter. In an imporatant first step towards

creating a degenerate mixed gas of Mn and Cr, we also measure the Mn-Cr inelastic rate constant – an important parameter in the initial co-evaporative cooling of these species.

4.1 Mn dimers

Mn is a transition metal with a half filled 3d shell of which all the electrons are uncoupled, giving rise to a large magnetic moment of $5\mu_B$ per atom. Because of its many electrons, Mn has generated much interest both experimentally and theoretically . The electronic structure of Mn dimers and larger clusters is poorly understood and thus has generated much debate [50, 51, 52, 53].

Mn is a unique element in the 3d transition metal series. The binding energy of Mn_2 is believed to be weak between 0.1 ± 0.1 and 0.56 ± 0.26 eV, leading to a bond length between 3.2 and 3.6$\mathring{A}$ which is actually larger than that in the bulk solid whereas the reverse is the case in all of the other transition metals [51, 54]. This weak binding energy raises certain questions about the relationship between the molecular structure and electronic configuration of Mn clusters. Does the weak binding energy suggest a weak magnetic coupling of all the electrons in the cluster such that magnetic moment of the cluster is just the sum of the free atom values [52]? Is the coupling ferromagnetic or anti-ferromagnetic? If small clusters are ferromagnetic, what is the critical size for a magnetic transition given that bulk Mn is not ferromagnetic [55]?

Unfortunately, there have been no gas phase studies of the electronic structure of Mn or Mn clusters. Experimental studies have been limited to electron spin resonance (ESR) measurements on Mn clusters embedded in a krypton or xenon matrix [51, 54]. The study of Mn_2 found antiferromagnetic coupling between the 3d electons and estimated a Heisenberg exchange coupling constant of $J = -9 \pm 3$ cm^{-1}. On the

other hand, Mn_2^+ has been found to be ferromagnetic with a total magnetic moment of $11\mu_B$ [56]. Similarly, a cluster believed to be Mn_5 has been observed to have a magnetic moment of $25\mu_B$ [51, 57]. Theoretical studies Mn clusters have focused on *ab initio* calculations of the electronic structure but have been diverse in their results [50, 52, 53, 55, 58, 59]. There is still no clear explanation of why Mn_2 is antiferromagnetic whereas other clusters are ferromagnetic. The role, if any, of the matrix that the clusters are embedded in is also still unresolved, leaving open the question of what the magnetic coupling is like for free, isolated dimers.

The half filled 3d shell of Mn is accompanied by a filled outer 4s shell. As found in the study of He-Ti($^3F_2$) collisions, the filled 4s shell leads to a suppression of collisionally induced spin relaxation [60, 61]. The ratio of elastic to inelastic collision cross-section for Ti was measured to be $\sigma_{el}/\sigma_{in} = 4000$, compared to calculations of He collisions with Sr($^3P_2$), Ca($^3P_2$), or O($^3P_2$) (all open valence shells) with predicted ratios of $\sigma_{el}/\sigma_{in} \sim 1$ [62, 63, 64]. Related to the question of magnetic coupling is the role that the filled outer 4s shell plays on other inelastic processes such as spin-exchange or dipolar relaxation.

To gain information on these processes we study the collisional dynamics of Mn atoms in the gas phase by magnetically trapping 10^{12} Mn atoms at 500 mK. At this temperature, observing trap loss due to dipolar relaxation and spin-exchange is a sensitive measure of the Mn-Mn internuclear potential. Accurate knowledge of this potential should help to answer the questions about the magnetic coupling in Mn_2 and understand any shielding effect by the 4s shell.

4.2 Experimental procedure

The experimental apparatus, shown in Fig.4.1, is described in detail in Reference [65] and Chapter 5. Details relevant to this experiment are summarized below. A cylindrical plastic/copper composite cell is cooled to temperatures as low as 500 mK by a ^{3}He refrigerator through a copper thermal link. The cell fits coaxially inside the bore of a superconducting anti-Helmholtz magnet, creating a spherical quadrupole trap with depths up to 3.9 T. A valve separates the trapping chamber from the pumping region filled with $\sim$ 30 g of activated charcoal cooled to a temperature of 1.5 K. At the top of the trapping chamber sits both a metal manganese target and metal chromium target.

With the valve initially closed, the cell is filled with ^{3}He gas at a typical density of 10^{16} cm^{-3}. A beam from a pulsed frequency-doubled Nd:YAG laser with a typical energy of 5 mJ per pulse is focused onto the Mn target. Mn atoms produced by the ablation pulse collides with the buffer gas and quickly thermalize to the temperature of the ^{3}He buffer gas. The atoms are detected via laser absorption spectroscopy on the $^6S_{5/2} \rightarrow {}^6P_{7/2}$ transition at 403 nm. Spectroscopic properties of Mn are summarized in Appendix C. Probe powers of 50 nW are typically used with no observed effect on the loss rate or temperature of the atoms. Figure 4.2 shows the magnetic field free spectrum of buffer gas cooled Mn. The peaks in the spectrum are transitions from Mn's six hyperfine states ($I = 5/2$). Roughly a few times 10^{12} total Mn atoms in all six hyperfine states are produced per ablation pulse. The relative position of the transitions are used to calibrate the frequency scan of the laser diode used for detection.

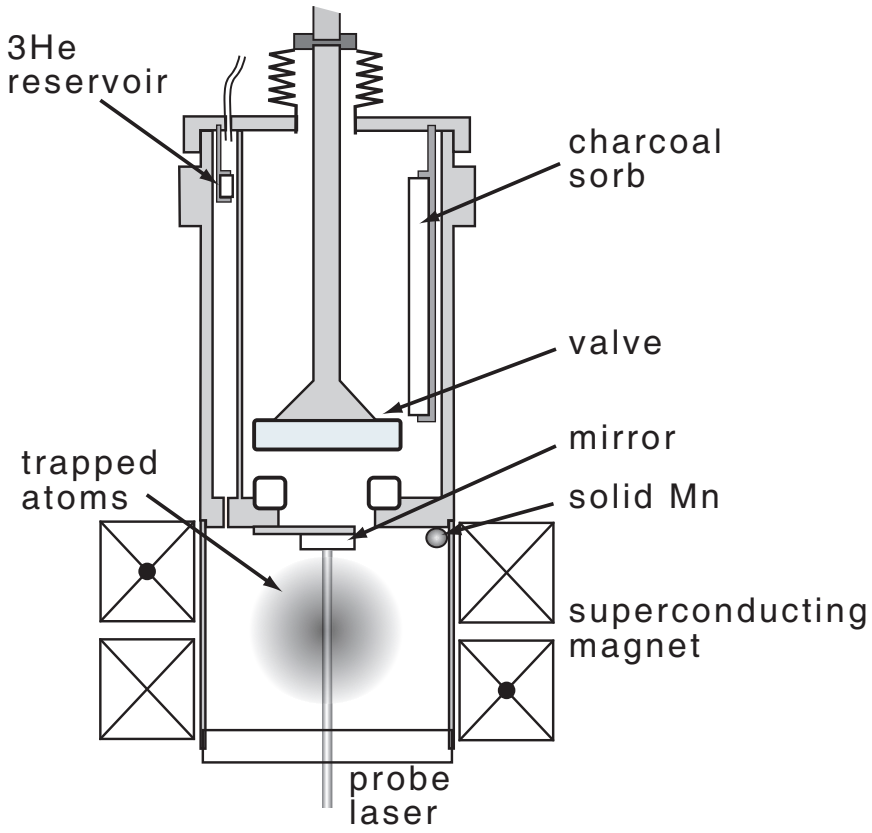

Figure 4.1: Schematic of the experimental cell for magnetically trapping Mn. Mn atoms are produced by a 5 mJ ablation pulse from a Nd:YAG laser.

4.3 Trapping of Mn

With the magnetic trap on, the low-field-seeking Mn atoms which have thermalized with the ^{3}He buffer gas fall into the magnetic trap while the high-field-seeking atoms are lost to the cell wall. Five seconds after the ablation pulse the valve is opened, pumping the ^{3}He from the trapping chamber onto the charcoal sorb with a time constant of $\sim$ 50 ms. After this loading procedure, we are able to trap upwards of 2×10^{12} Mn atoms in the electronic stretched state and in all six hyperfine $|m_S = +5/2, m_I = +5/2, ..., -5/2\rangle$. Because we are in the high field limit, m_S and m_I are good quantum numbers. Figure 4.3 shows a spectrum of $N_o = 2 \times 10^{12}$ magnetically

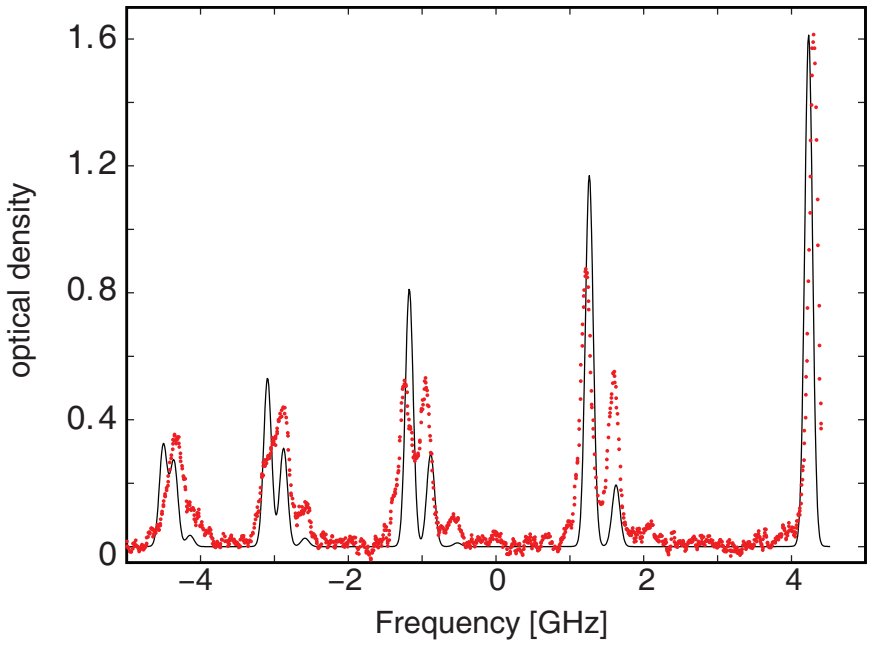

Figure 4.2: Magnetic field free spectrum of Mn. Points are experimental data. Solid line is a simulation of the spectrum for the ${}^6S_{5/2} \rightarrow {}^6P_{7/2}$ transition at 403 nm which accurate calculates the position of the transitions but not their intensities.

trapped Mn atoms at a temperature of $T = 855$ mK and a trap depth of $B_{\text{trap}} = 3.6\ T$ ($\eta = 14$). N and T are determined by fitting the trapped atoms' Zeeman-broadened absorption spectrum to that of a spatial Boltzmann distribution of atoms in our magnetic trap, as described in Reference [48, 66]. The multiple features in the spectrum are due to $\Delta m = 0, +1$ transitions from the six hyperfine states that are simultaneously trapped. The densities for the hyperfine states $|m_I = +5/2, ..., -5/2\rangle$ are $n_o = 15$, 8.5, 6.0, 5.5, 9.0, and 8.5×10^{11} cm^{-3}, respectively.

4.4 Mn-Mn collisions

To measure the inelastic collisional processes, we observe trap loss of the different hyperfine states. Because all the ^{3}He atoms are pumped away (one-body lifetime > 100 s), trap loss is due solely to Mn-Mn collisions. The trap loss measurements

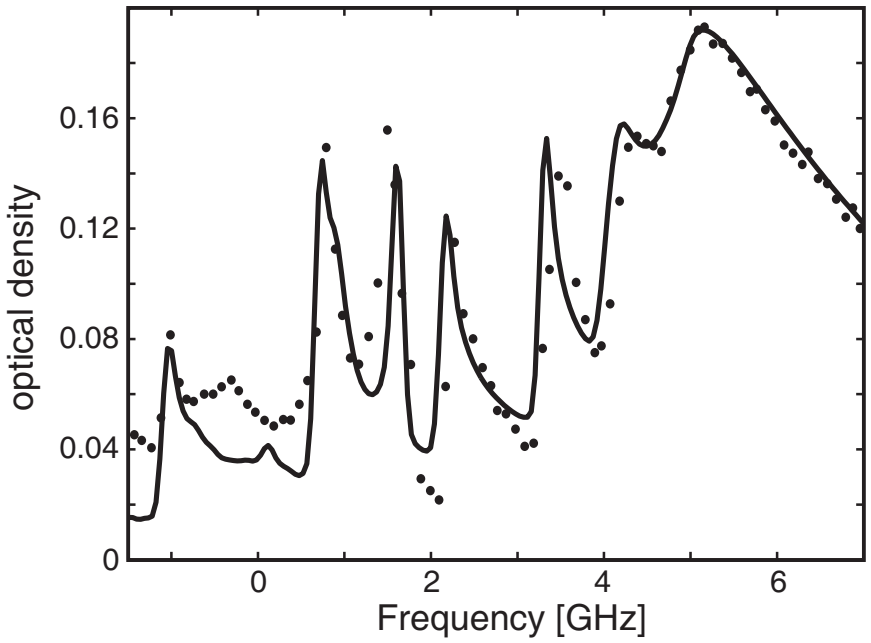

Figure 4.3: Spectrum of magnetically trapped Mn at $B_{\rm trap} = 3.6$ T. The solid line is a fit to a spatial Boltzmann distribution yielding $T = 855$ mK, $n_o = 5.2 \times 10^{12}$ cm^{-3}, and $N = 2 \times 10^{12}$.

are taken at an $\eta = 14$. At this high η, the likely-hood that a single elastic collision results in an evaporated atom is $f(14) \sim 10^{-4}$. Therefore unless the elastic collision rate constant is abnormally large compared to other atoms ($g_{\rm Mn} > 10^{-9}$ cm^3/s), we can neglect the contribution of evaporation of over the trap edge. Trap loss is then dominated by inelastic collisions.

4.4.1 Hyperfine populations

Unfortunately, measuring the population of each hyperfine state as a function of time is not straightforward. Figure 4.4 shows the simulated spectrum of each hyperfine state at a temperature of $T = 850$ mK, trap depth of $B_{\rm trap} = 3.6$ T, and peak density of $n_o = 1 \times 10^{12}$ cm^{-3}. Because of the Zeeman broadening, each hyperfine state cannot be spectroscopically resolved. At any single frequency, there are contributions

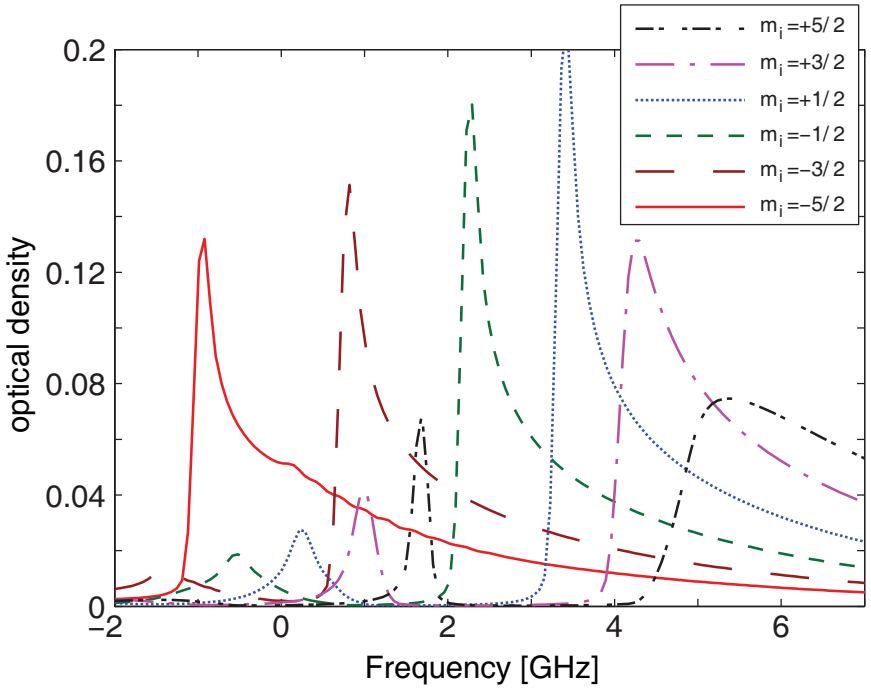

Figure 4.4: Simulation spectrum of each hyperfine state magnetically trapped Mn at $T = 850$ mK, $n_{m_I} = 10^{12}$ cm^{-3}, and trap depth $B_{\text{trap}} = 3.6$ T.

from all six states.

Fortunately, we can get around this problem with the following procedure. After the Mn atoms are initially trapped, we continuously scan the laser frequency over the transition, making sure the scans are wide enough to record all the features in the spectrum. The frequency is scanned at 5 Hz which is much shorter than any trap loss timescale.

Because the simulated spectrum well describes the measured spectrum, we can construct a system of linear equations to convert the measured optical density at a particular frequency to the density of each hyperfine state. At any given frequency f, the contribution of each hyperfine state of density $n_{|m_I\rangle}$ to the total measured optical

density *od* can be written as

$$od(f) = \sum_{m_I=-5/2}^{5/2} a_{|m_I\rangle}(f) n_{|m_I\rangle}, \tag{4.1}$$

where $a_{|m_I\rangle}(f)$ is the coefficient whose value represents the simulated optical density for a given density $n_{|m_I\rangle}(a)$ of state $|m_I\rangle$ at the frequency f. By choosing six different frequencies, we can create a transfer matrix $\hat{A}$ to fully describe the contribution of the density of each hyperfine state to the measure spectrum. In matrix form this can be written as $\hat{od} = \hat{A}\hat{n}$ or

$$\begin{bmatrix} od(f_1) \\ od(f_2) \\ od(f_3) \\ od(f_4) \\ od(f_5) \\ od(f_6) \end{bmatrix} = \begin{bmatrix} a_{+5/2}(f_1) & a_{+3/2}(f_1) & \dots & a_{-5/2}(f_1) \\ a_{+5/2}(f_2) & \dots & \dots & a_{-5/2}(f_2) \\ a_{+5/2}(f_3) & \dots & \dots & a_{-5/2}(f_3) \\ a_{+5/2}(f_4) & \dots & \dots & a_{-5/2}(f_4) \\ a_{+5/2}(f_5) & \dots & \dots & a_{-5/2}(f_5) \\ a_{+5/2}(f_6) & \dots & \dots & a_{-5/2}(f_6) \end{bmatrix} \begin{bmatrix} n_{+5/2} \\ n_{+3/2} \\ n_{+1/2} \\ n_{-1/2} \\ n_{-3/2} \\ n_{-5/2} \end{bmatrix}. \tag{4.2}$$

If there is no Zeeman broadening and each state can be spectroscopically resolved, $\hat{A}$ is diagonal. The conversion from measured optical density to the density of each hyperfine state is simply the inverse, $\hat{n} = \hat{A}^{-1}\hat{od}$. $\hat{A}$ is unique for any combination of trap depth and temperature.

4.4.2 Trap loss

Figure 4.5 shows the inferred trap loss of each hyperfine state at two different temperatures and trap depths. In Figure 4.5a, $T = 855$ mK and $B_{\text{trap}} = 3.6$ T. In Figure 4.5b, $T = 480$ mK and $B_{\text{trap}} = 2.0$ T. Because both measurements are taken at $\eta = 14$, the average magnetic field where a two-body collision is most likely to occur simply scales with B_{trap} and is equal to $\bar{B}_{2b} = 3B_{\text{trap}}/2\eta = 0.39$ T and 0.21 T, respectively.

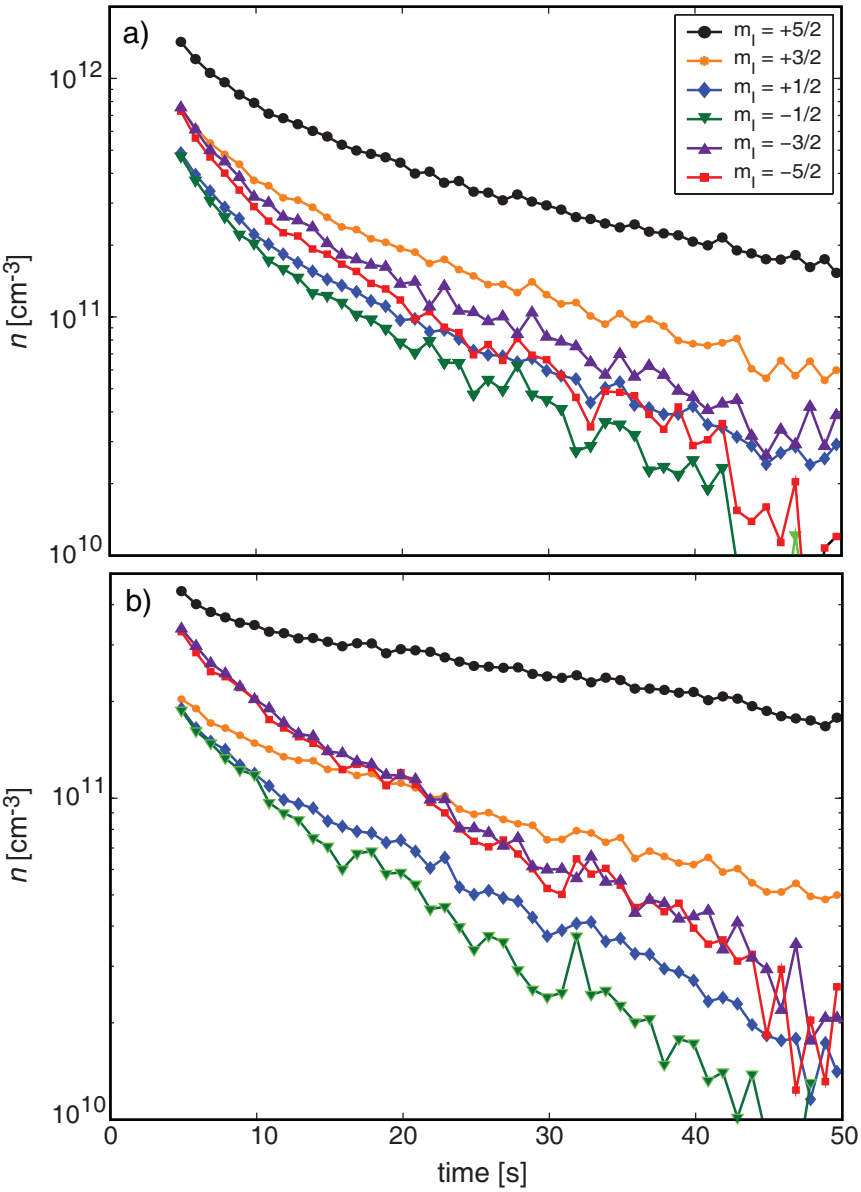

Figure 4.5: Trap loss for the different hyperfine states of Mn. a) Trap loss measured at $T = 855$ mK and trap depth $B_{\text{trap}} = 3.6$ T ($\eta = 14$) b) Trap loss measured at $T = 480$ mK and trap depth $B_{\text{trap}} = 2.0$ T ($\eta = 14$). Mn atoms are produced at $t = 0$, and the valve is opened at $t = 5$ s.

The evolution of each hyperfine state is governed by dipolar relaxation and spin-exchange. In dipolar relaxation, the interaction of two magnetic dipole moments μ colliding at a distance $\mathbf{R}$ is given by [67, 68]

$$\hat{H}_{\text{dipole}} = \frac{\mu_1 \cdot \mu_2 - 3(\hat{\mathbf{R}} \cdot \mu_1)(\hat{\mathbf{R}} \cdot \mu_2)}{R^3}. \tag{4.3}$$

The interaction leads to a coupling of the magnetic moment with the motion of the colliding pair. Spin-exchange collisions on the other hand are dictated by the exchange interaction which is commonly expressed as

$$\hat{H}_{\text{ex}} = J\mathbf{S_1} \cdot \mathbf{S_2}, \tag{4.4}$$

where $\mathbf{S}$ is the spin of the atom and J is the exchange coupling constant. Because this term is used to model the Pauli exclusion effects of the electron cloud, the rate of spin-exchange collisions is a measurement of the electronic wavefunction overlap of the colliding pair [50, 69].

If we first only take into account dipolar relaxation, then the probability of an inelastic collision should simply depend on the magnetic moment. Since all the states have a magnetic moment of $5\mu_{\text{B}}$, they should all decay with the same inelastic rate constant g_{dip}. The decay of the sum of all the populations $n_{\text{total}} = \sum n_{m_I}$ should follow the rate equation

$$\frac{d}{dt} n_{\text{total}}(t) = -g_{\text{dip}} \int n_{\text{total}}^2(r,t) d^3r, \tag{4.5}$$

where the integration is over the spatial distribution of atoms in the trap. Figure 4.6 plots n_{total} as a function of time for the data set taken for $T = 855$ mK and $B_{\text{trap}} = 3.6$ T. A fit of $n_{\text{total}}(t)$ to the numerical solution of Equation 4.5 yields a dipolar relaxation rate of $g_{\text{dip}} = 4 \pm 0.2 \times 10^{-13}$ cm^3/s. The fit though good for most of the data deviates from the data at times longer than 30 s, predicting that the population should level off more than it actually does.

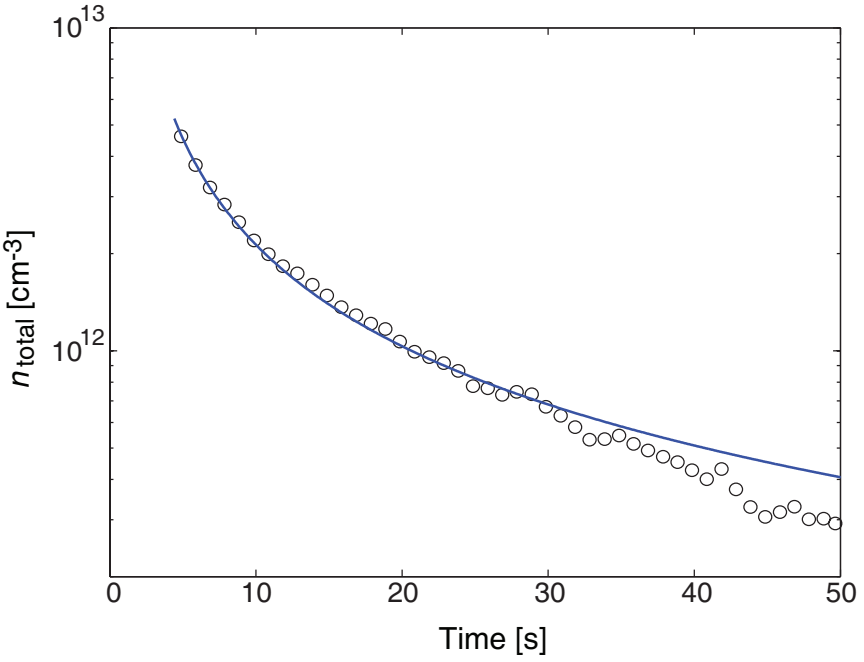

Figure 4.6: Decay of the total population of Mn atoms for $T = 855$ mK and $B_{\text{trap}} = 3.6$ T. The solid line is a fit to the solution of Eq. 4.5 yielding $g_{\text{dip}} = 4 \pm 0.2 \times 10^{-13}$ cm^3/s.

Each individual hyperfine state should decay similarly with the same inelastic rate constant according to the rate equation

$$\frac{d}{dt} n_{m_I}(t) = -g_{\text{dip}} \int n_{m_I}(r,t) n_{\text{total}}(r,t) d^3r \tag{4.6}$$

Since we already know g_{dip} and the initial population, the decay of each state is already predetermined. Figure 4.7 plots the solution of Equation 4.6 for each hyperfine state given $g_{\text{dip}} = 4 \times 10^{-13}$ cm^3/s and initial population $n_{m_I}(t = 5)$. As is clear from the figure, the decay of each hyperfine state is not well described by this simple model. Each state except the $|m_I = +5/2\rangle$ state decays much faster than predicted by the rate constant $g_{\text{dip}} = 4 \times 10^{-13}$ cm^3/s.

Instead, there must be more than just dipolar relaxation contributing to trap loss. This could be due to spin-exchange. Equation 4.4 can be rewritten in terms of

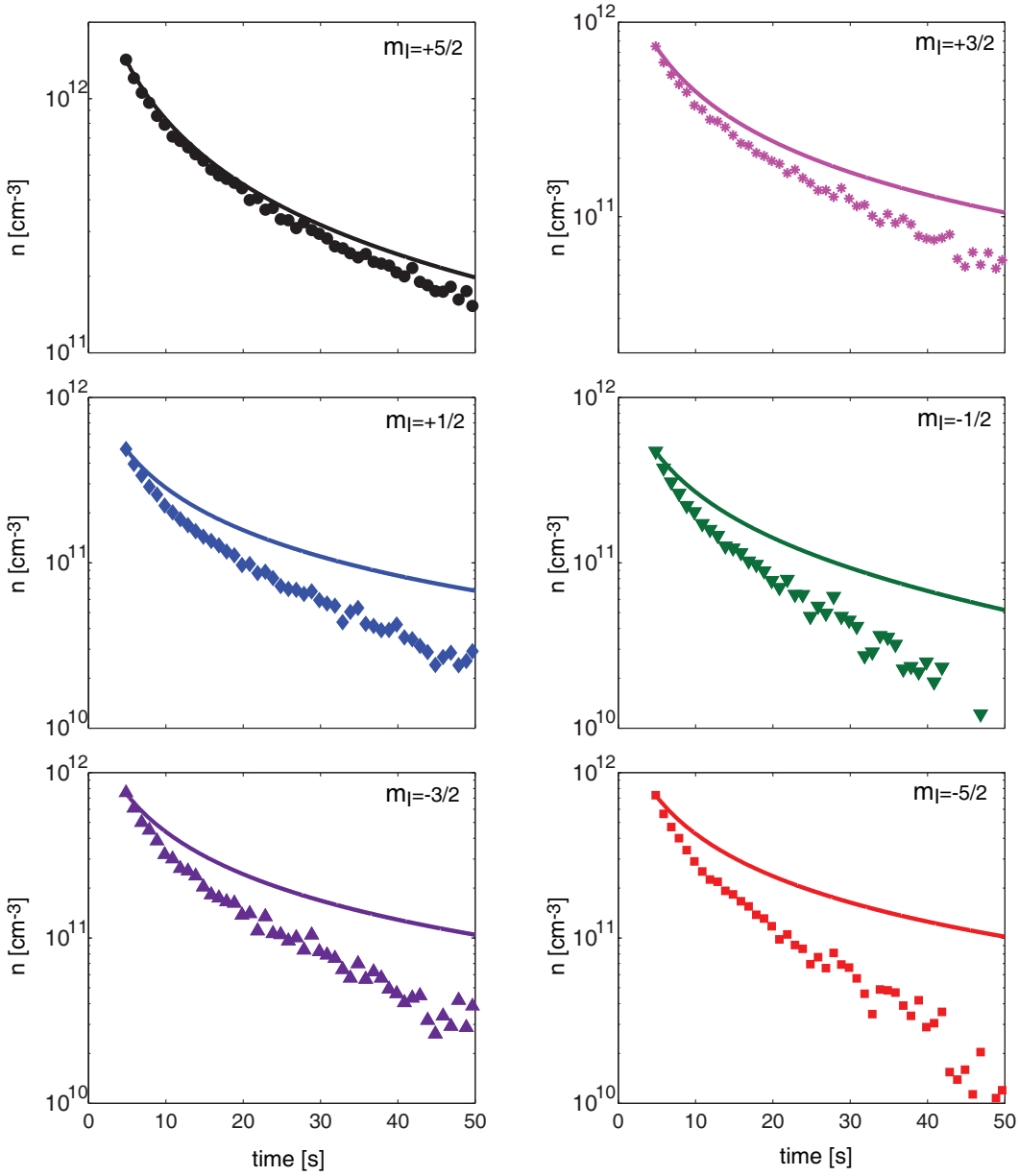

Figure 4.7: Decay of each hyperfine state of Mn atoms for $T = 855$ mK and $B_{\text{trap}} = 3.6$ T. The solid lines are solutions to Eq. 4.6 given $g_{\text{dip}} = 4 \times 10^{-13}$ cm^3/s and initial population $n_{m_I}(t = 5)$.

lowering and raising operators,

$$J\mathbf{S_1}\cdot\mathbf{S_2} = \frac{1}{2}J(4S_{z1}S_{z2} + S_1^+S_2^- + S_1^-S_2^+) \tag{4.7}$$

The operators S^+ and S^- only act on the electronic spin. Because all the states in the trap are in the electronic stretched state $m_S = +S$, we would initially expect that spin-exchange collisions do not occur in the trap. Even though we are in the high field limit where m_S and m_I are good quantum numbers, identifying each state as $|m_S, m_I\rangle$ is not entirely accurate. The atoms are not in the infinite field limit, and to first order each state shown in Figure 4.5 has a small admixture of the $|m_S = 3, m_I + 1\rangle$ states,

$$|m_S = +5/2, m_I\rangle \rightarrow |m_S = +5/2, m_I\rangle + \epsilon|m_S = +3/2, m_I + 1\rangle, \tag{4.8}$$

where ϵ is the degree of mixing of the two states. ϵ depends on the magnitude of the hyperfine coupling relative to the Zeeman energy and is proportional to $A/(g_e\mu_B B)$ where A is the hyperfine coupling constant [69, 70]. Mn has a small hyperfine coupling constant (A=-72 MHz) relative to the alkali-metals, and therefore it reaches the high-field limit ($B \sim 0.02$ T) much sooner [71]. Only the fully stretched state $|m_S = +5/2, m_I = +5/2\rangle$ has no admixture of any other states. For simplicity we rename the states $|m_I = +5/2\rangle, |m_I = +3/2\rangle, \ldots, |m_I = -5/2\rangle$ as $|a\rangle, |b\rangle, \ldots, |f\rangle$.

Because of the small admixture of the $|m_S = +3/2\rangle$ state, spin-exchange collisions can now occur between the nuclear spin and electronic spin. Not only will there be collisions that produce the less magnetically trapped $|m_S = 3/2\rangle$ states which would soon be lost from the trap, there will also be collisions in which the states $|a\rangle, \ldots, |f\rangle$ are the byproducts. The rate equation for each state will have terms to account for both the depletion and repopulation of the state, each with its own spin-exchange rate constant g_{ij},

$$\frac{d}{dt}n_a(t) = -g_{\text{dip}}\int n_a(r,t)n_{\text{total}}(r,t)d^3r + \sum_{i,j} g_{ij}\int n_i n_j d^3r, \tag{4.9}$$

where the sum is over all the possible combinations of states. The spin-exchange rate constant g_{ij} should scale as B^{-2} because the degree of mixing $\epsilon \propto B^{-1}$ [70]. Therefore spin-exchange should occur ~ 3 times more readily in the trap sample with $B_{\text{trap}} = 2.0$ T than in the trap sample with $B_{\text{trap}} = 3.6$ T.

Unfortunately because g_{ij} is different for every term, we are unable to make any quantitative statement as to the role spin-exchange collisions play in the observed trap loss other than noting that spin-exchange should be present along with dipolar relaxation, perhaps accounting for the additional observed loss. However, it may be possible to formulate a theoretical model in which all the spin-exchange collisions are parameterized by a limited number of variables. The trap loss data can then be fitted for these values. This should provide us information on the $S = 5$ and $S = 4$ molecular potential and possibly elucidate the character of the magnetic coupling of Mn dimers.

4.5 Mn-Cr mixture

In the next step, we set out to simultaneously trap atomic Mn and atomic Cr in order to demonstrate that multi-species trapping using buffer gas loading is straightforward. The experimental procedure is similar to that described in Section 4.2. The beam from the Nd:YAG laser is now split in two by a 50/50 beam splitter, and each beam, both with typical energies of 5 mJ, is focused onto its respective metal target (Fig. 4.8). The Cr atoms are detected by laser absorption spectroscopy on the ${}^7S_3 \rightarrow {}^7P_4$ transition at 425 nm.

Roughly 10^{13} Cr atoms and 10^{12} Mn atoms are produced per ablation pulse. After the valve is opened, 2×10^{12} Cr atoms in the fully stretched state $|J = 3, m_J = +3\rangle$ and 4×10^{11} Mn atoms in the fully stretched state $|m_J = +5/2, m_I = +5/2\rangle$ are

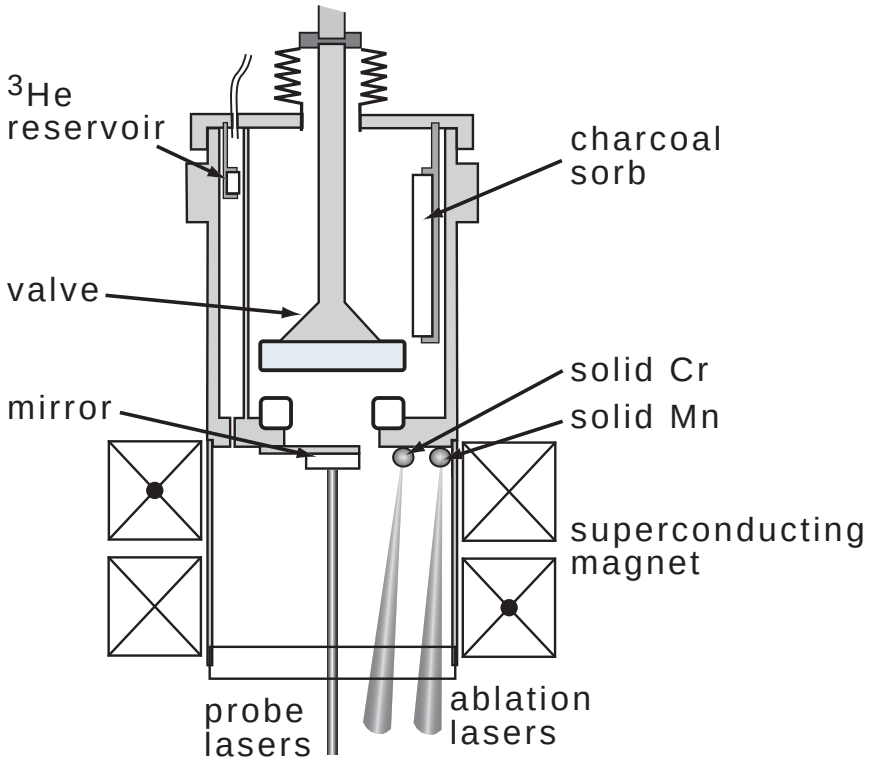

Figure 4.8: Schematic of the experimental cell for magnetically trapping Mn and Cr. The ablation pulse from a Nd:YAG laser is split in two by a 50/50 beam splitter.

detected in the magnetic trap at peak densities of 4×10^{13} cm^{-3} and 3×10^{12} cm^{-3}, respectively. The other isotopes of Cr, which are less naturally abundant, cannot be spectroscopically resolved under the current experimental conditions. We do detect other hyperfine states ($|m_J = +5/2, m_I = -5/2, ..., +3/2\rangle$) of Mn in the trap but with a factor of five or more lower yield.

We monitor the decay of the trapped sample to measure the inter-species inelastic collision rate (Fig. 4.9). By blocking one of the ablation beams and loading the trap with only one atomic species, we alternately monitor the trap loss due to Mn-Mn or Cr-Cr inelastic collisions. The decay of a single trapped species fits well to the expected functional form for two-body loss. At a temperature of 600 mK and trap depth of 3.5 T, the Mn-Mn and Cr-Cr inelastic rate constants are $g_{\mathrm{Mn,Mn}} =$

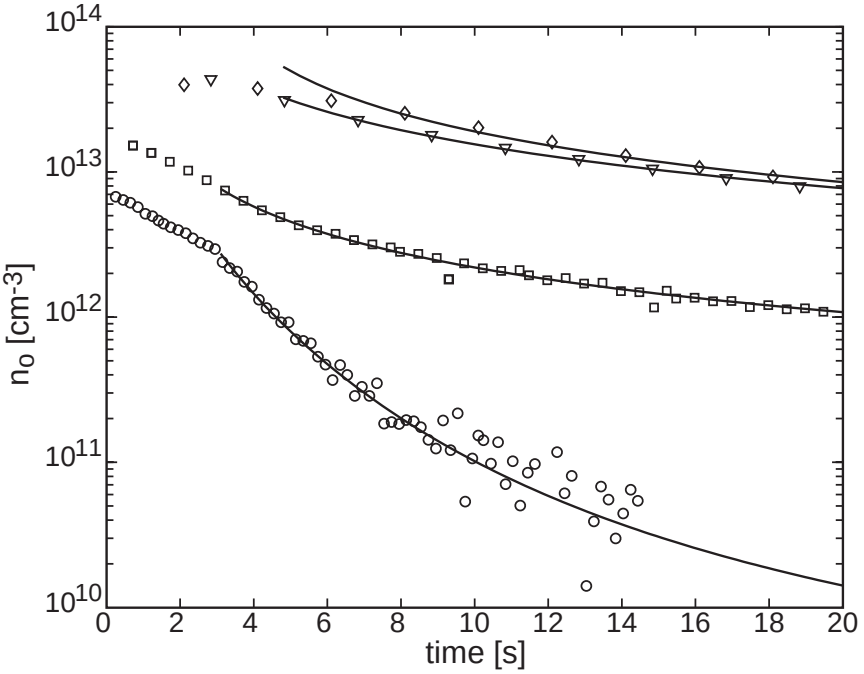

Figure 4.9: Decay of the peak density of trapped Mn and Cr. Ablation pulse occurs at t=0. Valve opens at 3 s. Triangles: decay of Cr. Squares: decay of Mn. Diamonds: decay of Cr in the presence of Mn. Circles: decay of Mn in the presence of Cr. Solid lines: fits to expected loss model (Eq. 4.10, 4.11)

$3.8\,(\pm 0.2)\times 10^{-13}$ cm^3/s and $_{\mathrm{Cr,Cr}} = 5.0\,(\pm 0.5)\times 10^{-14}$ cm^3/s, respectively.

Mn and Cr are also loaded simultaneously so as to extract the Mn-Cr inelastic rate. The decays are fit to the appropriate rate equations:

$$\begin{aligned}
\frac{d}{dt}n_{\mathrm{Mn}}(t) &= -g_{\mathrm{Mn,Mn}}\int n_{\mathrm{Mn}}^2(r,t)d^3r \\
&\quad -g_{\mathrm{Mn,Cr}}\int n_{\mathrm{Mn}}(r,t)n_{\mathrm{Cr}}(r,t)d^3r \qquad (4.10)\\
\frac{d}{dt}n_{\mathrm{Cr}}(t) &= -g_{\mathrm{Cr,Cr}}\int n_{\mathrm{Cr}}^2(r,t)d^3r \\
&\quad -g_{\mathrm{Cr,Mn}}\int n_{\mathrm{Mn}}(r,t)n_{\mathrm{Cr}}(r,t)d^3r, \qquad (4.11)
\end{aligned}$$

where $n(r)$ is the density distribution in the trap of either Mn or Cr and g is the inelastic rate constant for Cr, Mn, or Mn-Cr. $g_{\mathrm{Mn,Cr}}$ is determined by numerically integrating Equation 4.10 using the measured value of $g_{\mathrm{Mn,Mn}}$ and the measured decay

of the trapped Cr as inputs. A least-squares fit of the measured Mn decay to the numerical solution of Equation 4.10 yields a rate constant of $g_{\mathrm{Mn,Cr}} = 1.5\,(\pm 0.2) \times 10^{-13}$ cm^3/s for Cr induced Mn trap loss, corresponding to a cross-section of $\sigma_{\mathrm{Mn,Cr}} = 1.4\,(\pm 0.5) \times 10^{-16}$ cm^2. Similarly, Equation 4.11 can be numerically integrated to determine the rate constant for Mn induced Cr trap loss. However because the density of Mn is an order of magnitude less than that of Cr, we are only able to place an upper limit of $g_{\mathrm{Cr,Mn}} \leq 3 \times 10^{-13}$ cm^3/s, consistent with $g_{\mathrm{Mn,Cr}}$, as expected. The dominant source of systematic error comes from determining the peak density from the measured absorption spectra.

The Mn-Cr inelastic rate is several orders of magnitude smaller than those measured in trapped alkali mixtures in the presence of MOT lasers ($\sim 10^{-10}$ cm^3/s) [72, 73]. In a MOT, light assisted collisions open up a number of additional decay channels including radiative escape and fine-structure changing collisions. In the absence of radiation fields, inelastic rates of $\leq 10^{-14}$ cm^3/s were reported for bi-alkali mixtures in their fully stretched state [74]. Our measured Mn-Cr rate is similar to rates measured in single species systems with similar magnetic moments where dipolar relaxation is the dominant trap loss mechanism [44, 75]. Taken as a whole, the measurement of magnetic dipolar 2-body rates does not, as one might naively expect, scale as μ^4. The Cr-Cr inelastic rate measured here is much slower than either the Mn-Mn or Mn-Cr inelastic rate. The hyperfine structure of Mn may open additional inelastic channels such as spin-exchange as discussed in Section 4.4. In addition, the variations may be due to the fact that even at 0.6 K, differences in the details of the long-range part of the internuclear potential between the colliding pair play a significant role [45].

Chapter 5

He* Experimental Setup

Technological improvements have extended buffer gas loading to atoms with magnetic moments of $\geq 2\mu_{\mathrm{B}}$. However, our choice to magnetically trap and evaporatively cool metastable helium He* ($2\mu_{\mathrm{B}}$) required additional modifications to the experimental setup. In this chapter, we describe modifications made to the cryogenic apparatus to integrate a low temperature RF discharge with a new cell design to ensure better temperature management. We also implement independent electronic control the two solenoids of the magnetic trap for evaporative cooling and improve the spectroscopic detection sensitivity.

5.1 The apparatus

5.1.1 Previous setup

A schematic diagram of the experimental apparatus prior to modification is shown in Figure 5.1. A detailed description of the components of the apparatus is presented in Reference [65]. Details which are relevant to the modifications and the He*

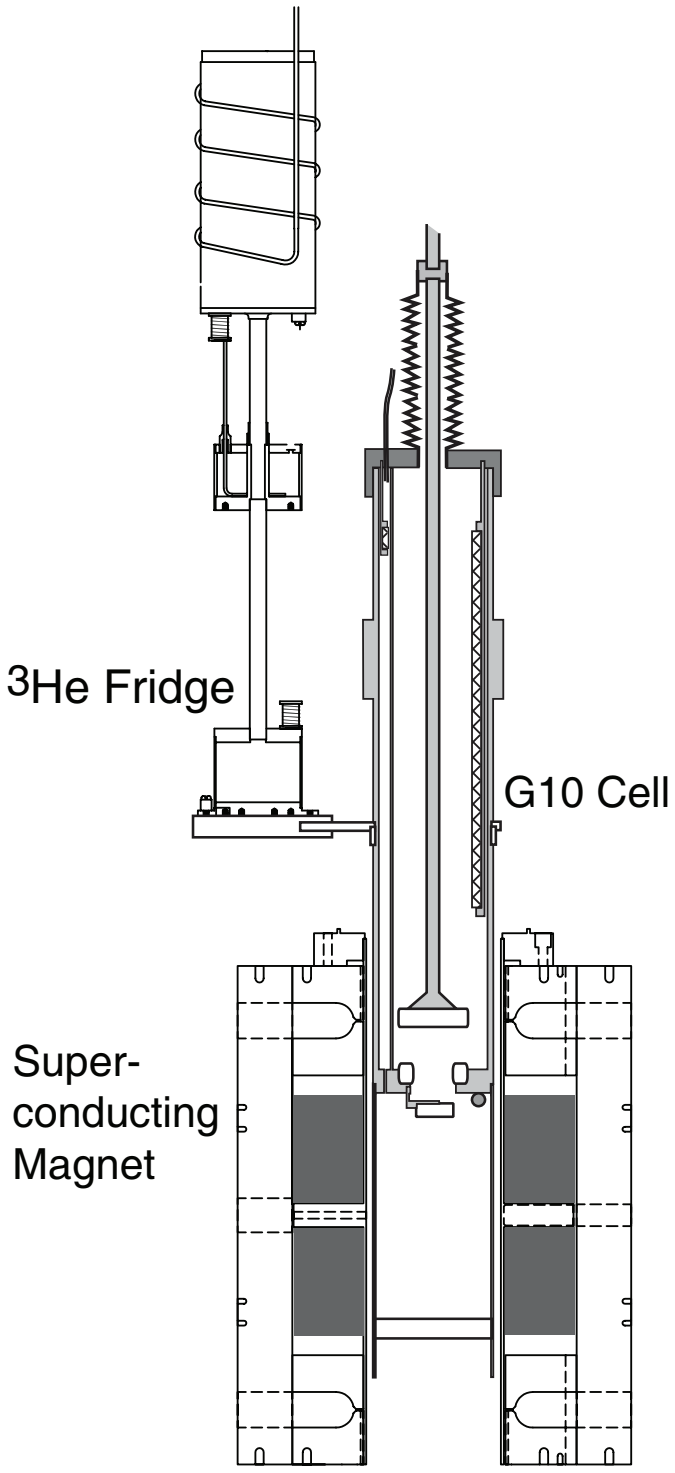

Figure 5.1: Schematic diagram of the experimental apparatus.

experiments are summarized below.

Atoms were produced and trapped inside a cylindrical G-10 cell [76, 77]. A valve separated the trapping chamber from a pumping region filled with ~ 30 g of activated charcoal cooled to 1.5 K by the 1 K pot [78]. The valve aperture was 1 inch in diameter and had a conductance of ~ 100 l/s, resulting in a trapping chamber pump out time of ~ 50 ms. This pump out time was limited by the conductance of the aperture, not the pumping speed of the charcoal sorb. The valve extends in vacuum to room temperature where it was actuated by a pneumatic cylinder.

Helium gas was introduced into the trapping chamber by first coating ~ 1 g charcoal sorb located inside the ante-chamber with helium gas through the fill line. This fill line sorb was maintained at 1.5 K by the 1 K pot. By heating the sorb to > 8 K, helium gas desorbed from the sorb and entered the trapping region through a pinhole. The fill line sorb cooled back to 1.5 K within a few minutes at which point it began pumping on the helium gas again. The time constant to pump helium gas from the trapping chamber back through the pinhole was ~ 2000 s. This was comparable to the time that helium gas could escape through the valve aperture when the valve was closed with ~ 100 lbs. of force.

The cell sat coaxially inside the bore of a superconducting anti-Helmholtz magnetic trap created by two solenoids with currents running in opposite directions. The critical current of the superconducting magnet at 4.2 K was 102.5 A. At the maximum operating current of 102 A, the trap depth , which was set by the cell wall, was 4.03 T. The cell radius was 3.49 cm.

The trapping chamber was maintained at 500 mK by a ^{3}He refrigerator [79] through a copper thermal link. 100 copper wires of 0.25 mm diameter were equally spaced and arranged to run along the length of the G-10 cell. At the top of the cell,

the copper wires were bundled together and anchored onto a copper cold plate attached to the ^{3}He pot. The thermal conductivity along the length of the cell provided by the copper wires was sufficient to maintain a uniform temperature to better than ~ 10 mK. The vertical arrangement of the copper wires prevented any possible paths for eddy currents to flow, essential for rapidly changing the magnetic fields.

5.1.2 Necessary changes

In previous implementations of buffer gas loading, the atoms to be trapped were produced via laser ablation of a solid metal precursor. The ablation beam was from a pulse frequency doubled Nd:YAG laser with typical pulse energies of 5-10 mJ. Though not particularly efficient, each pulse produced between 10^{11} to 10^{14} atoms depending upon the refractivity of the metal [29].

Unfortunately, He* cannot be produced via laser ablation. Standard methods for producing He* are direct current (DC) discharges or radio-frequency (RF) discharges. DC discharges are not compatible with our setup as arcing would quickly destroy the cell. Creating an RF discharge is possible in our cryogenic environment, requiring an RF coil to be wrapped around the cell. Coincidentally, the optimal helium density for sustaining RF discharges overlaps the density in which buffer gas loading generally operates [80, 81].

Unfortunately, an RF discharge is not compatible with the current cell design. The copper wires providing thermal conductivity along the cell would shield the RF from reaching the inside of the cell where the gas is contained. In addition, the thermal link from the cell to the ^{3}He pot provided by the copper wires is not optimal. In the last iteration of the experiment, the ^{3}He pot temperature was 330 mK, roughly 150 mK colder than the cell. We believe this temperature differential was due to work

hardening of the copper wires as they were bundled together and attached to the ^{3}He pot cold plate, lowering their thermal conductivity. One of the conclusions of the first experiments on the apparatus was that the number of atoms trapped and thermally isolated is strongly dependent on the base temperature of the cell. For a $2\mu_B$ species, a decrease from 550 mK to 480 mK increased the number thermally isolated by over an order of magnitude (Fig. 1.4). To circumvent this problem, we will implement a superfluid helium thermal link which will also keep the cell electrically insulating. This requires additional gas lines and a redesign of the cell to incorporate a double walled jacket for the superfluid helium.

Evaporative cooling will also be implemented differently than in previous experiments. Rather than uniformly lowering the magnet trap depth, evaporation will be achieved by lowering the trapped sample towards the cell window, thereby preferentially removing high energy atoms as they collide with the window surface. The advantage of this method is the decoupling of the trap depth from the confinement. Details of this evaporation method are presented in Chapter 6. The position of the trap center is determined by the ratio of the currents in the two solenoids of the magnet, so lowering the trap center requires independent computer control of these two currents.

5.2 RF discharge

An RF discharge is a standard method of producing metastable states of noble gases [80, 81]. It relies on the acceleration of electrons and ions by radio waves to energies sufficient to collisionally ionize neutral atoms in the discharge. This rapidly leads to the formation of a plasma as the discharge is sustained. However, the discharge must be initiated by the presence of some electron or ion. Commonly one can

wait for a cosmic ray to cause an ionization event or use a radioactive beta emitter. In our case, we focus a 1 mJ pulse from a Nd:YAG laser on a solid sample to create a small ablation plume as a source of electrons and ions. As ions and electrons recombine and de-excite, a fraction of the particles in the discharge will be in the metastable state. Typically the efficiency for metastable production in RF discharges is $\sim 10^{-5} - 10^{-6}$ [80, 81]. The number is much lower than that measured in DC discharges. In most of the He* laser cooling experiments, the DC discharge which produces beams of He* can reach efficiencies up to 10^{-3} [82]. However, an RF discharge is much easier to implement in our cryogenic setup.

The RF discharge starts with a helical coil that surrounds the trapping chamber of the cell. The coil is made of 0.64 mm diameter copper wire with $\sim$ 15 evenly spaced windings. To reduce the heat load on the cell, the coil is wrapped around on a separate G-10 cylindrical form that is concentric with the cell (Fig. 5.2). The form which is thermally linked to 4 K by $\sim$ 50 0.25 mm diameter copper wires that run along the outer diameter fits snugly inside the lower IVC. A lasso standoff on the bottom of the cell prevents physical contact between the cell and RF form. The coil is secured onto the form by Mylar tape while the copper wire providing thermal conductivity is secured by Stycast 1266 [83] epoxy.

The RF circuitry starts with an RF synthesizer [84] able to generate RF signals between 1 kHz to 250 MHz (Fig. 5.3). The RF is then sent into two RF switches [85] operated back to back to limit leakage. Even though each switch has a minimum isolation of 30 dB, this leakage is enough to generate $\sim$ 50 μW of eddy current heating. To obtain the coldest cell temperatures, the RF generator is only powered on during the short time the RF is needed. The RF switches are controlled by TTL signals generated by the data acquisition program. The RF signal is then sent into

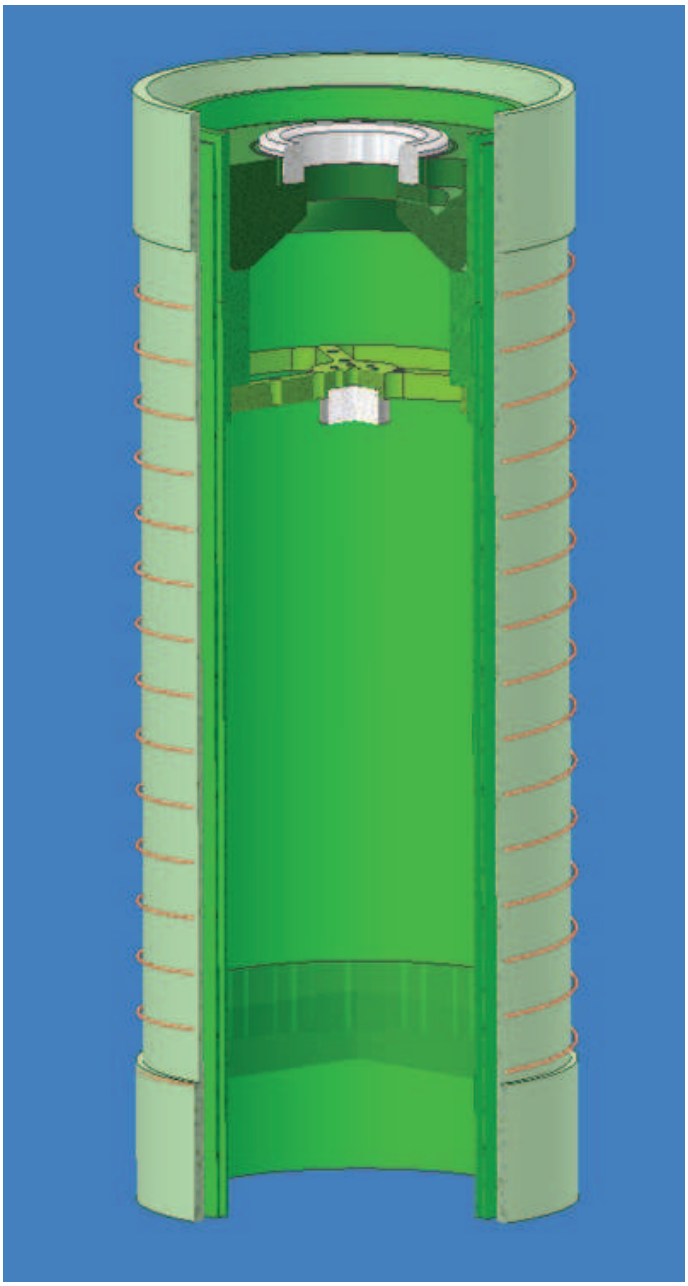

Figure 5.2: Schematic diagram of the RF form and coil surrounding the trapping chamber of the cell.

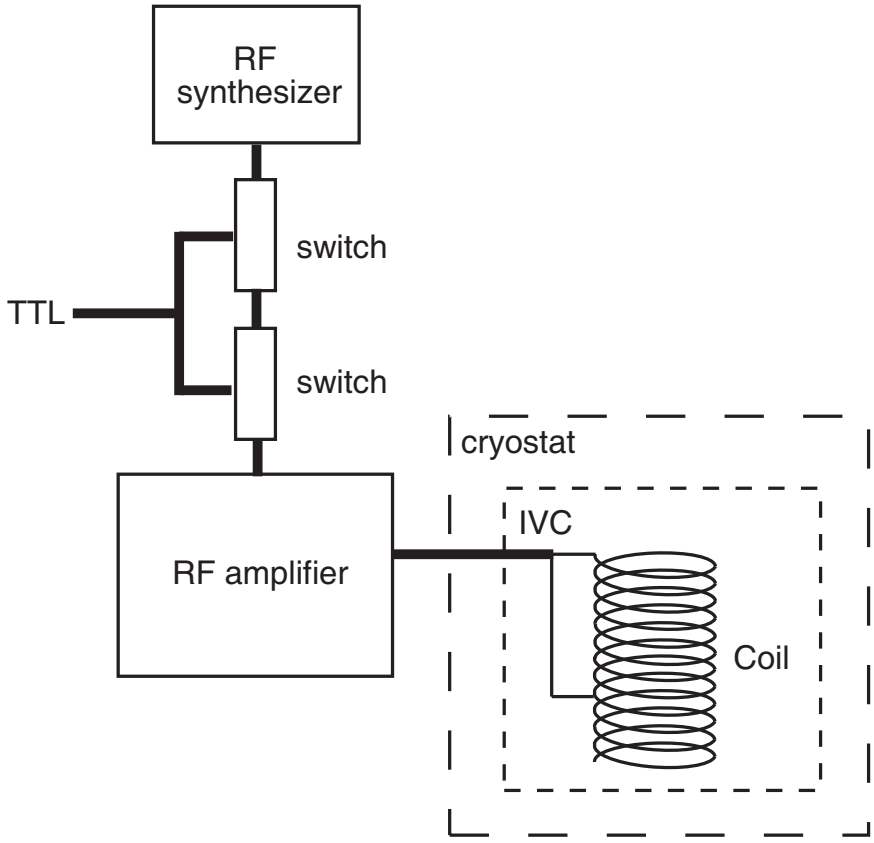

Figure 5.3: Schematic diagram of the RF circuit. The bold lines represent coax lines while the thinner lines represent bare copper wire.

an RF amplifier [86] capable of generating 50 W of RF power. The amplifier operates only in the 10-150 MHz frequency range. From the amplifier, the RF is coupled to the coil via an SMA cable which runs through the cryogenic bath space and into the IVC. Once inside the IVC, the coax cable is split, and the center lead is soldered onto one end of the discharge coil. The second lead taps onto the coil at a location which maximizes the coupling of the RF to the coil as measured by a directional coupler.

5.3 Superfluid thermal link

The RF discharge requires replacing the copper wires that provide the thermal link of the cell to the ^{3}He pot with a substitute which provides good thermal but poor electrical conductivity and does not shield the RF. Superfluid helium satisfies this criterium. Near the transition temperature of 2.2 K, the thermal conductivity of helium diverges . In the temperature range of 0.3-1 K, the thermal conductance is

$$16\frac{\mathrm{W}}{\mathrm{K}}(\frac{\mathrm{d}}{\mathrm{cm}})^3(\frac{\mathrm{L}}{\mathrm{cm}})^{-1}(\frac{\mathrm{T}}{\mathrm{K}})^3, \tag{5.1}$$

where d is the diameter of the thermal link and L is the length [87]. For example at 0.5 K, the thermal conductance of a 1 cm diameter line that is 10 cm in length is 0.2 W/K, a factor of 10 less than for a similar link made from copper with an RRR=100 [88].

5.3.1 Double walled cell

Implementing the superfluid link requires substantial changes. The new experimental cell is now double-walled, formed by two concentric G-10 cylinders. Filling the space between the two cylinders, known as the jacket space, is the superfluid helium (Fig. 5.4). The design and construction is similar to that described in Reference [48] with slight changes to take into account the different fridge/cell geometry. Because the ^{3}He pot is located in the upper IVC and space in the lower IVC where the cell resides is quite tight, the length of the superfluid jacket extends $\sim$ 30 cm, from the bottom of the cell up to the location of the ^{3}He pot. The jacket not only surrounds the trapping chamber which we want cold, it also surrounds the charcoal insert which is at 1 K. The alignment of the charcoal insert is therefore crucial to preventing a touch to the cell walls. Also when the jacket is under vacuum, there is $\sim$ 100 lbs. of

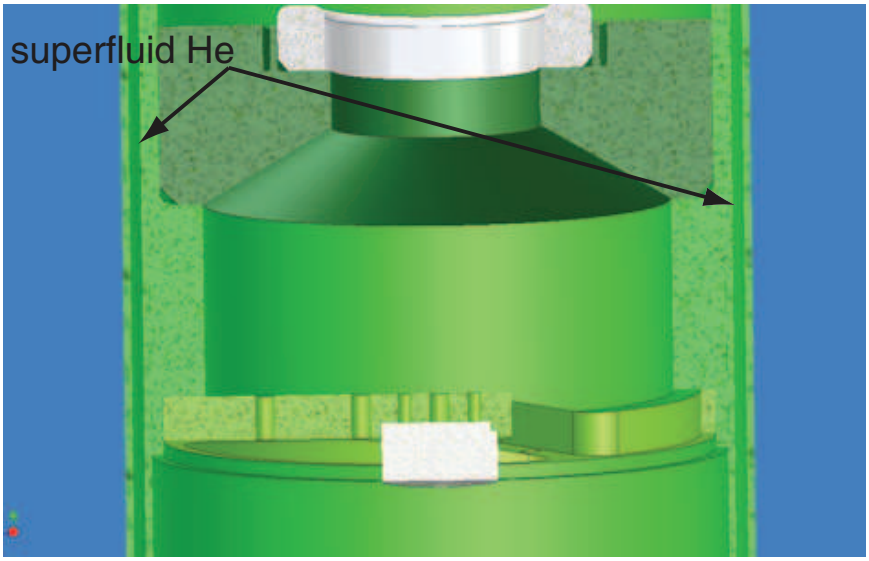

Figure 5.4: Schematic diagram of the top portion of the trapping region of the double walled cell. The superfluid fills the jacket space and provides the thermal conductivity along the length of the cell.

force pushing in on it. As a safety precaution we also place four 5×5 mm spacers midway down the length of the jacket to prevent an implosion. The thickness of the jacket is chosen to keep the cell uniform in temperature down its entire length. Assuming a reasonable heat load of 100 μW emanating from the bottom of the cell, a 1.5 mm thick jacket can maintain < 10 mK temperature differential.

5.3.2 Reservoir

The jacket is thermally linked to the ^{3}He pot by a flexible stainless bellows connected to a superfluid reservoir sitting on the ^{3}He cold plate (Fig. 5.5). The 5 cm bellows is corrugated with a 1 cm inner diameter. The time constant for cooling the superfluid helium in the jacket through this heat link is ~ 1 s. The reservoir is made of gold plated copper and has a volume of 30 cm^3. At 400 mK, Kapitza resistance between the gold surface and superfluid helium though not dominant is present. For a surface

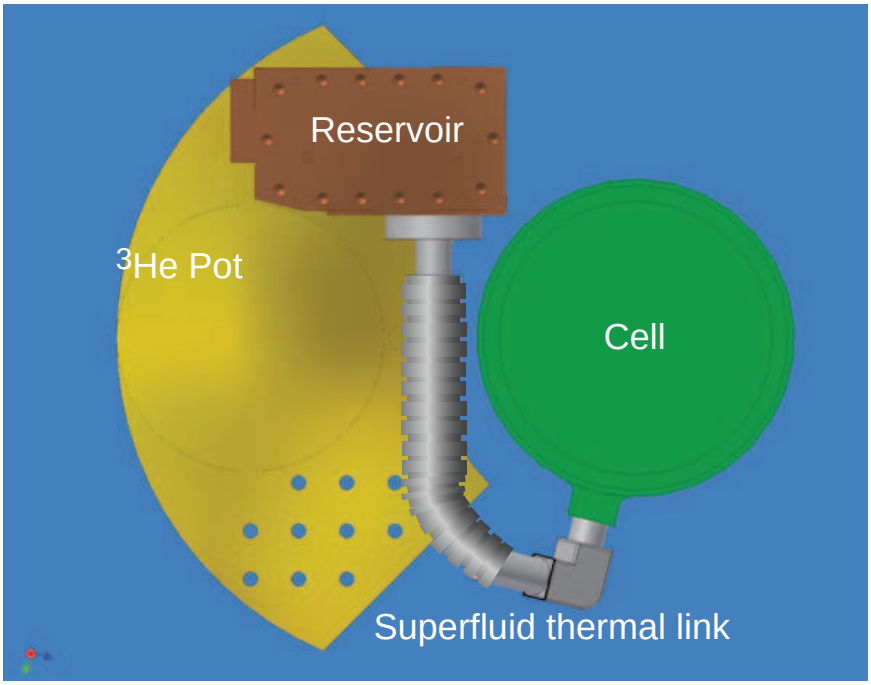

Figure 5.5: Schematic diagram of the superfluid reservoir connected to the cell via a stainless bellows.

area of 100 cm^2, the Kapitza resistance generates a $\sim$ 50 mK temperature differential between the ^{3}He pot and superfluid [88]. We add two plates covered with silver sinter to increase the effective surface area. The sinter is the same homemade one described in Reference [48, 89] and increases the surface area by a factor of $\sim$ 5.

The reservoir is connected to a helium fill line running through the bath space to room temperature. On the room temperature side, the fill line is connected to a helium cold trap which then leads to a helium dump with a volume of 70 L. The cold trap can be bypassed by a 10 psi inline check valve to allow the jacket to vent in the case of a rapid temperature rise in the cell above 4 K.

5.3.3 Filling the jacket

The volume of the jacket surrounding the cell is $\sim$ 105 cm^3. The volume of the stainless bellows is $\sim$ 15 cm^3, and the volume of the reservoir is $\sim$ 30 cm^3. These regions need to be filled to ensure a good thermal link from the cell to the ^{3}He pot, taking care not overfill, since extra superfluid would lead to an increased heat load due to conduction to warmer parts of the fill line. Given the liquid helium density of 0.15 g/cm^3 [90], one Torr of helium gas in the dumps corresponds to liquid volume of 0.1 cm^3 below 2 K.

We begin filling the jacket by putting helium gas into the dumps. To gain the largest cooling power to condense the warm incoming helium gas, we thermally link the ^{3}He pot to the 1 K pot by heating the charcoal sorb to $\sim$ 25 K. After passing through a helium cold trap, the gas is slowly fed into the jacket. The filling rate is monitored to keep the 1 K pot below 2 K. Because there is some uncertainty in the actual volume of the jacket and bellows, the jacket is filled incrementally. After each increment, the ^{3}He pot is regenerated, allowing the ^{3}He pot and cell to cool to their base temperatures. Fig. 5.6 shows the progression of the base temperatures after each incremental addition of helium. The optimal liquid volume is $\sim$ 115 cm^3. Unlike with the 100 copper wires, the temperature difference now between the cell and the ^{3}He pot is minimal. Additional liquid increases the temperature of the ^{3}He pot/cell system, most likely caused by the liquid level reaching the warmer parts of the fill line.

5.3.4 Superfluid film

Unfortunately the good thermal link provided by the superfluid helium also contributes a significant heat load on the ^{3}He pot. Flow of the superfluid film from the

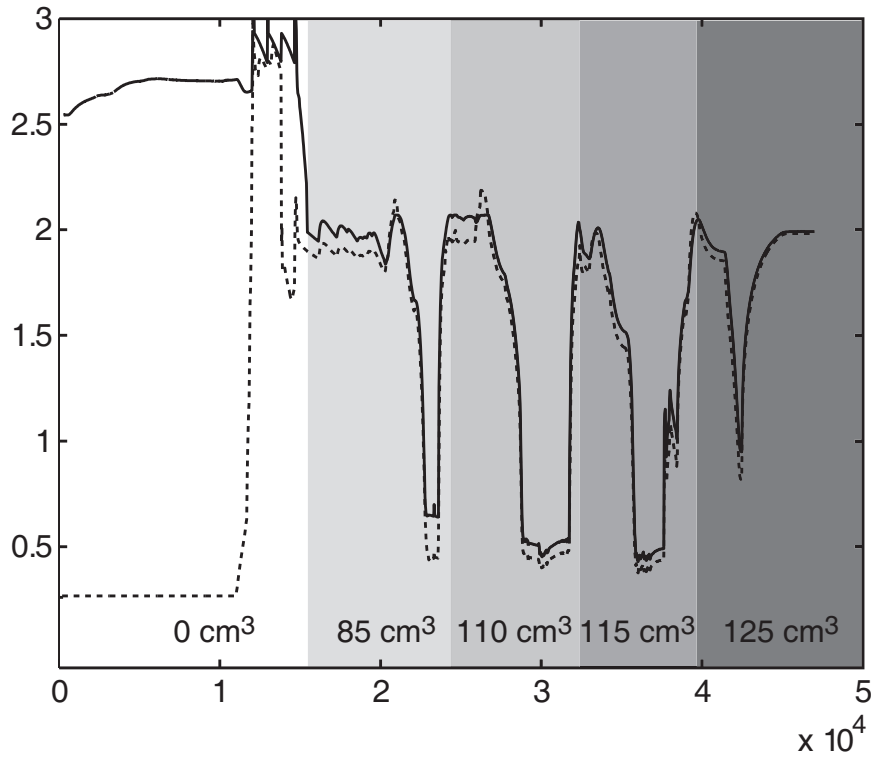

Figure 5.6: ^{3}He pot and cell temperature for as varying amounts of superfluid helium is added to the jacket. The solid line is the fridge temperature, and the dashed line is the cell temperature. The different shaded regions indicate the volume of superfluid helium that has been added to the jacket. The filling procedure is described in the text.

cold regions near the ^{3}He pot to warm regions in the fill line causes helium atoms to evaporate. These hot atoms can then contribute a heat load if they are reabsorbed onto the colder regions. If all the atoms in the film which desorb at the warmer region are reabsorbed at the ^{3}He pot, the heat load is given by $P = Lv_c t\pi d$, where $L = 2$ J/cm^3 is the latent heat, $v_c = 45$ cm/s is the superfluid critical velocity, $t \sim 30$ nm is the saturated film thickness, and d is the diameter of the fill line [91]. Assuming 1/8 in diameter fill line, the heat load from the superfluid film flow is expected to be < 100 μW.

This heat load can be reduced by placing a small pinhole in the line [92]. The

smaller radius provided by the pinhole reduces the volume of superfluid that flows through it. Therefore the number of atoms boiling off and being reabsorbed is reduced. The pinhole is made by drilling a 0.38 mm diameter hole in a VCR gasket blank. The effect of the pinhole on the conductance of the fill line is negligible compared to the length of the rest of the line.

In the first iteration, we used a 1/8" line that was thermally anchored to progressively colder parts of the fridge (Fig. 5.7). Curly sections in the line were made to prevent direct paths for hot atoms to reach the colder regions before being cooled by the walls of the fill line. A 0.38 mm diameter pinhole gasket was placed in the line right before the reservoir.

Unfortunately, we found that the heat load due to the superfluid film was much higher than expected. After filling the line with helium to make the thermal link, the temperature of the ^{3}He pot was 460 mK, a heat load of ~ 1 mW. The cell temperature tracked closely with the ^{3}He pot temperature. Serendipitously, we found that by gently shaking the dewar, we could lower the temperature of the ^{3}He pot and cell to 350 mK, a heat load of ~ 200 μW. However, this temperature was only sustained by the continual agitation of the dewar. The ^{3}He pot warmed back to 460 mK in a few seconds once the agitation stopped. We concluded that the heat load was not due to a touch for two reasons. First, the ^{3}He pot reached a base temperature of 250 mK when there was no helium in the superfluid jacket. Second, cold temperatures could only be sustained upon continual agitation. Systematically tilting the dewar slightly in different directions and holding it there did not lower the base temperature. We believe that the majority of the heat load was due to the reflux of the superfluid film. Agitation of the dewar disrupted the flow of the film in the fill line, decreasing the flux of hot helium atoms from recondensing onto the colder regions.

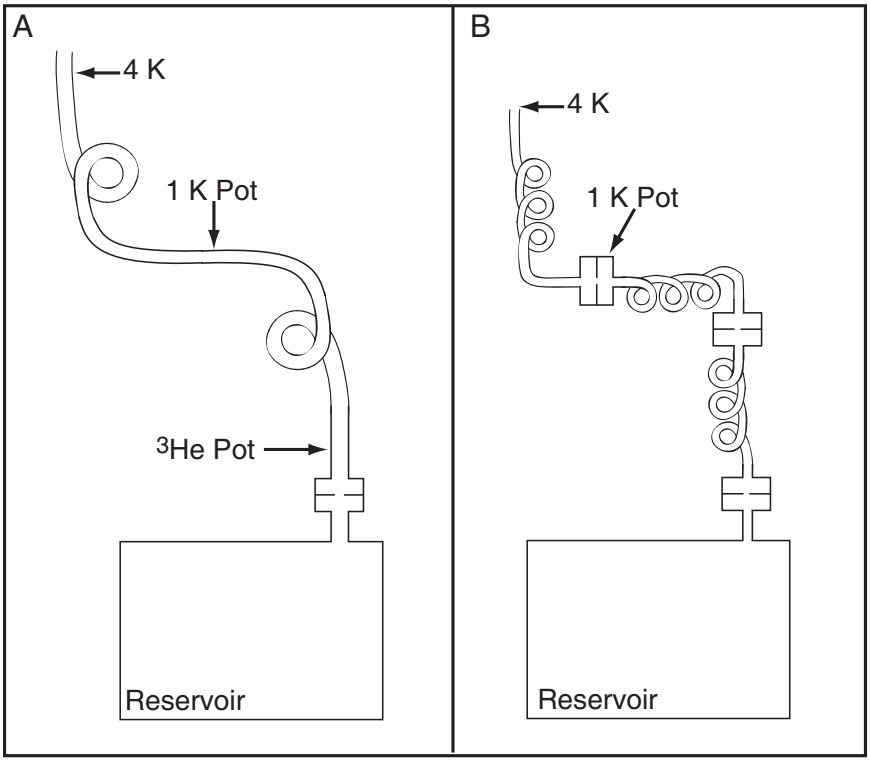

Figure 5.7: Schematic diagrams of the fill line for the superfluid thermal link connected to the reservoir. Arrow mark locations which are thermally anchored to progressively colder parts of the fridge. Rectangular sections of the fill line represent the pinhole gasket. A) First iteration with 1/8" diameter line and 0.38 mm pinhole gasket. B) Second iteration with 1/16" diameter line and 0.33 mm pinhole gaskets.

In the second iteration of the experiment, we made the following changes to the fill line to try to reduce the heat load due to the superfluid film. The fill line is now 1/16" in diameter with a total of three pinhole gaskets. In addition to the original one, a pinhole gasket is placed at the location of the 1 K heat link and another further down the line towards the reservoir. The pinhole diameters have been reduced to 0.33 mm. In addition, the heat link to the ^{3}He pot at the last gasket is removed. These changes dramatically reduced the heat load on the ^{3}He pot to $\sim$ 190 μW, resulting in a base temperature of 340 mK. Like before, continual agitation of the dewar lowered the temperature but now only to 320 mK. Table 5.1 is a summary of

the base temperatures obtained for the two iterations.

Table 5.1: Comparison of the base temperatures for the two versions of the jacket fill line.

	1st iteration	2nd iteration
^{3}He pot (thermal link empty)	260 mK	240 mK
^{3}He pot (thermal link full)	460 mK	345 mK
Cell (thermal link full)	500 mK	390 mK

5.4 Cooling the valve shaft

In the previous setup, the valve shaft contributed a heat load of $\sim$ 200 μW even though sections of the shaft were thermally linked to the 1 K pot and 4 K bath. This heat load was due to conduction from room temperature since the valve shaft ran from the cell to the top of the support structure through a vacuum space. Efforts to bulk up the heat link to 4 K did improve the situation but did not completely remedy the problem. When the valve was closed, the base temperature of the cell was 480 mK and cooled to 400 mK after opening the valve.

Rather then letting the shaft run through vacuum, we allowed the valve shaft to be cooled by the helium vapor in the bath. This required simply adding an additional section of bellows where the valve shaft intersected the IVC. There is now only a 5 mK temperature difference between an open and closed valve, a heat load of less than 10 μW.

5.5 Magnet

The Mark IV superconducting magnet used in this experiment has a pair of leads originating from each coil unlike its predecessors [20]. However this feature was never utilized in any of the previous experiments. The two coils were simply run in series with a single power supply. However evaporative cooling by lowering the sample towards the window requires that the current in the two coils be independently controlled. The position of the trap center relative to the window is determined by the ratio of the currents in the top and bottom coil. The magnetic field profiles for varying ratios of top and bottom coil currents are described in Chapter 6.

5.5.1 Circuit

To implement this evaporation procedure, we use four power supplies. Two high current power supplies separately control the top and bottom coil currents [93]. Unfortunately, the high current power supplies has a current stability of only 0.1% which is too high for evaporation at the lowest trap depths. This problem is alleviated by running a second low current power supply [94] with a 10^{-4} current stability in parallel with the high current power supply. The low current supplies have a maximum output of 20 A.

During the evaporation procedure, the low current power supplies are set to values which determine the final trap depth. Current from the high current power supplies are then added to achieve the full trap depth at 102 A. Evaporation then begins by lowering the currents in the high current power supplies. Unfortunately at the initial trap depth the superconducting magnet operates only 0.5 A below its critical current. Asymmetries in the current actually increases the magnetic field at the location of the top coil and can initiate a quench. Therefore, the two coils are initially uniformly

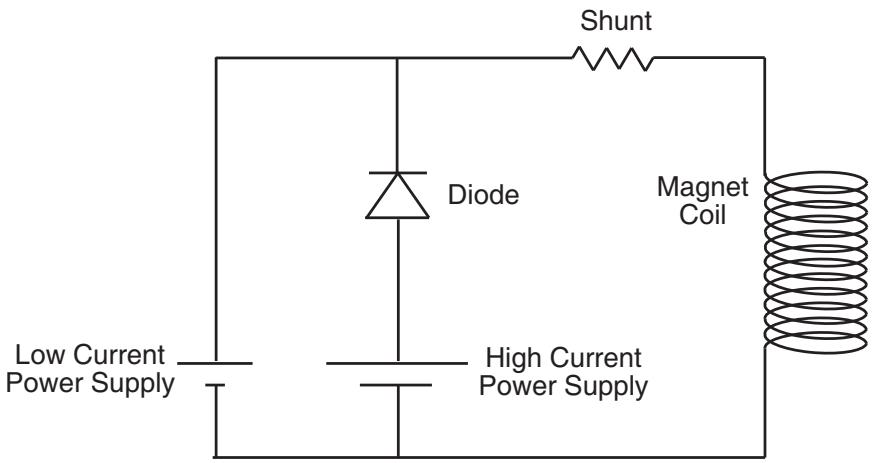

Figure 5.8: Circuit diagram for the magnet current supply. The circuit for the top and bottom magnet coils are the same.

ramped down to a total current of 75 A each to avoid quenching the magnet. At this point the currents in the high current supplies are assymmetrically ramped to zero at different rates. Once at zero, the low current power supplies have sole control over the magnet current. To ensure that the high current supplies are not contributing any current, they are actually ramped to a negative current. A diode is placed in series with the power supplies to prevent any current from flowing in this direction. The currents in both coils are monitored with two high current (old school) shunts of 0.01 Ω. A diagram of the magnet circuit is shown in Figure 5.8.

5.5.2 Computer control

The current in the magnet is computer controlled. Specific evaporation trajectories can be programmed in and easily modified to ensure that the evaporation is efficient during the cooling process. This is different than previously done in the evaporation of Cr. As mentioned in Chapter 3, the current was exponentially ramped down to the final trap depth with a time constant set by the L/R of the magnet and resistor bank. The time constant could not be varied. At the lower trap depths, the current

was changing too quickly compared to the elastic collision rate as the density of the sample was rapidly falling. In our case we are able to vary the rate of change of the trap depth depending upon the density and collision rates to ensure that the evaporation process is efficient.

We first used a 12-bit digital to analog output card [95] to control the current in the large power supplies. Unfortunately when evaporating to the lower trap depths, we observed the current changing in discrete steps. The 10 V output from the card corresponds to a current of 125 A in the magnet. Therefore the 12-bit card had a digital resolution of 30 mA, insufficient for the fine steps we wanted to take to evaporate. For example with the top coil at 15.1 A and bottom coil at 3.37, corresponding to a trap depth of 2.7 mK, the 30 mA digital resolution corresponds $\Delta U_{\mathrm{trap}} = 2.8$ mK. We then upgraded to a 16-bit card [96] giving us a digital resolution of 2 mA or $\Delta U_{\mathrm{trap}} = 0.19$ mK for a top/bottom coil current of 15.1/3.37 A.

Even with the 16-bit card further evaporation will also see signs of digitization. We can avoid this by computer controlling the current in the low current power supply at the low trap depths. If a 10 V output from the card corresponds to a 10 A from the supply, we can reduce the digital steps even further by more than an order of magnitude.

5.5.3 Eddy current heating

Another problem associated with ramping the magnet is eddy current heating. Even though the cell is almost all plastic, eddy currents can be induced in the ^{3}He pot and cold plate which is thermally connected to the cell by the superfluid thermal link. We observed that ramp rates faster than 2 A/s lead to eddy current heating causing an increase in the background gas density leading to trap loss. An example of trap loss

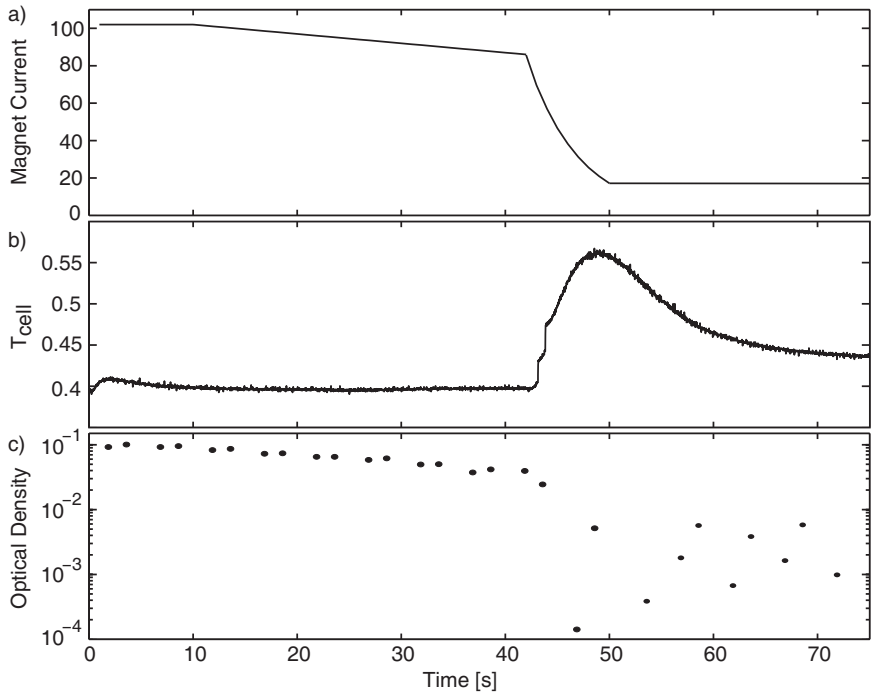

Figure 5.9: Eddy current induced trap loss. a) Current in the superconducting magnet. b) Cell temperature. c) Optical density of trapped ^{4}He*.

due to ramping the magnet too fast is shown in Figure 5.9.

5.6 Spectroscopic detection

We detect and monitor the trapped He* with absorption spectroscopy. As described in Appendix B, He* has two optically accessible transitions for detection, the $2^3S_1 \rightarrow 2^3P_2$ transition at 1083 nm and the $2^3S_1 \rightarrow 3^3P_2$ transition at 389 nm. All the experiments on He* described in this thesis use the 1083 nm transition.

To obtain the number and temperature of the trapped He*, we continuously scan the frequency of the probe laser back and forth over the Zeeman broadened transition. The scan rate, however, must be much faster than the rate of change of the He* cloud to accurate measure any of the properties of the trapped sample. Fortunately,

most of the processes affecting the trapped He* occur with timescales of seconds or longer, slow enough that problems associated with electronic bandwidth and noise are minimal.

5.6.1 Optics setup

The 1083 nm light used to probe the $2^3S_1 \rightarrow 2^3P_2$ transition is produced by a commercially available diode laser [97]. The laser produces up to 10 mW of light and has the range to access the two other fine structure lines in the excited state, the 2^3P_0 and 2^3P_1. The laser can be scanned rapidly up to 100 Hz over a range of ~ 5 GHz with no observable nonlinearities.

The layout of the optical beam path is shown in Figure. 5.10. A fraction of the beam from the diode laser is picked off and directed towards a wavemeter, allowing us to constantly monitor the wavelength of the laser. The beam then is reflected off a flipper mirror. The 1083 nm beam is invisible, making alignment difficult and at times frustrating. A second diode laser outputting a blue beam is used to initially align all the optics components. We then overlap the the 1083 nm beam and the blue beam using the flipper mirror. Alignment is then straight forward and requires minimal adjustments. The beam is chopped at 5 kHz and directed towards the dewar.

An optics breadboard is attached to the bottom of the cryogenic dewar. There the beam is divided into two by a 90/10 beam splitter. The 90% fraction is referred to as the reference beam and is directed to the reference photodiode [98]. The 10% fraction of the beam is referred to as the signal beam. It is directed up into the dewar and passes through the cloud of atoms. After reflecting off the mirror at the top of the cell, it passes again through the atoms and out the dewar. Care is taken to overlap the incoming beam and outgoing beam. This simplifies the spectroscopy as the two beams

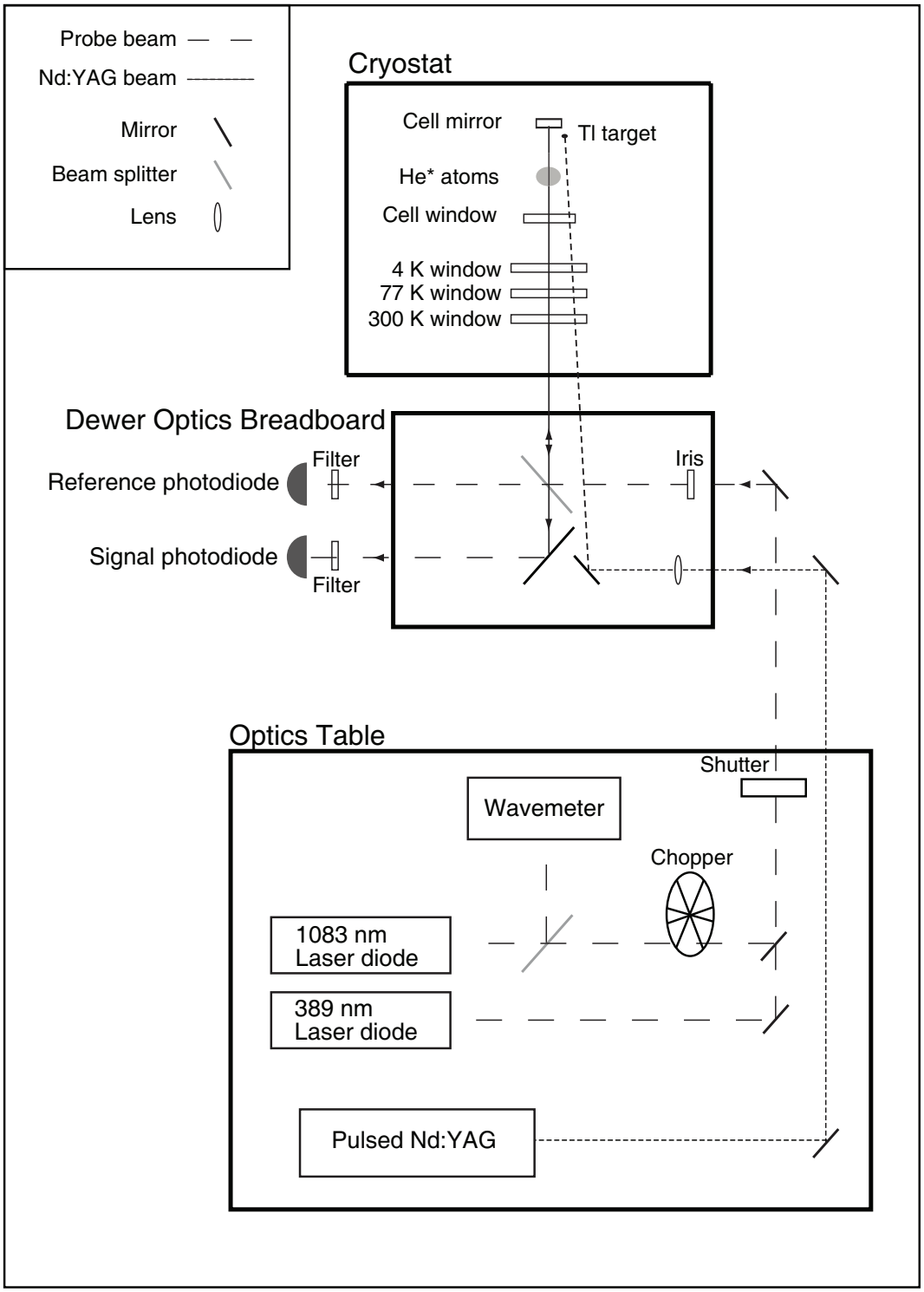

Figure 5.10: Layout of optical components used for spectroscopic detection.

trace out the same path through the magnetic field. Outside the dewar, the beam passes through the beam splitter and is directed to the signal photodiode, carrying all the information about the atoms. The photocurrent for both photodiodes are fed into a lock-in amplifier. During data processing, the signal and reference are divided to cancel out any noise which is common mode to both beams, such as laser intensity fluctuations.

The optics necessary for the YAG beam used to initiate the discharge are also shown in Figure 5.10. The laser is a Q-switched pulse Nd:YAG laser [99]. Each pulse is frequency doubled to 532 nm with a maximum possible output of 180 mJ. We use dielectric mirrors with a Max-Brite [100] coating which increases the damage threshold of the mirror. A 700 mm lens located underneath the dewar focuses the beam onto the metal targets surrounding the mirror. The lens is mounted on a translation stage whose position is varied for maximum ablation yield for a given pulse energy. As mentioned before, pulse energies of only 1 mJ are needed to reliably initiate the discharge. We also take care to locate all back reflections of the beam and adjust the beam path accordingly to prevent these back reflections from being focused onto any optical element.

5.6.2 Optical pumping

The $2^3S_1 \rightarrow 2^3P_2$ transition at 1083 nm has a saturation intensity of 0.167 mW/cm^2. This is much lower than all the blue transitions which have been previously used to detect the other atoms in our experiment because of the λ^{-3} dependence of the saturation intensity.

For a 2 mm beam diameter, we were initially sending $\sim$ 500 nW of laser power into the dewar, $\sim$ 300 nW of which made it through the 8 window surfaces to probe the

atomic cloud. At this intensity of 0.017 mW/cm^2, we noticed trap loss at a time scale of tens of seconds which we believed to be due to optical pumping as we continuously monitored the trap distribution by scanning the laser frequency. Lowering the probe beam power, we observed the proportional increase of the trap lifetime. However substantially lowering the laser power compromised our signal to noise. Because the photodiodes have a dark current of $\sim$ 50 pW, we needed to use at least 50 nW of laser power to have a sensitivity of 10^{-3}. At this laser power trap loss due to optical pumping was substantially reduced but not negligible.

Therefore during the evaporation process, we did not continuously monitor the atomic cloud. The atoms were allowed to evolve in the dark. Only at the very end of the evaporation trajectory did we open the shutters and spectroscopically probe the atomic distribution to obtain the number and temperature. The time scale to obtain a spectrum was less than a second, a timescale which is much shorter than the time scale for optical pumping. Therefore, the trap distribution should not be affected by the laser power during the measurement period.

In addition, because the transition is in the IR, care was taken to prevent stray light from entering into the dewar. Other labs studying trapped lithium atoms have seen background light induced trap loss [101].

5.6.3 389 nm transition

Optical detection can also be performed on the $2^3S_1 \rightarrow 3^3P_2$ transition at 389 nm. The advantage of this transition over the 1083 nm transition is two fold. First, the saturation intensity is a factor of 30 larger because of the shorter wavelength. Second, photomultiplier tubes (PMTs) can be used for detection at this wavelength. Because of the intrinsic gain of the PMTs, the signal to noise can be much better than

for the photodiodes. Unfortunately, the disadvantage of this transition is the lower absorption cross-section which scales are λ^2. When we implemented detection using the 389 nm transition, the factor of 10 reduction we saw in the noise was cancelled out by the factor of 10 we lost in absorption. Even though we used only the 1083 nm transition in this experiment, using the 389 nm transition would have been equally effective for detection. One advantage which should not be underestimated is the ability to see the beam for alignment purposes.

Chapter 6

Evaporative Cooling of He*

Of all the atoms which have been Bose-condensed, metastable helium He* ($2\mu_B$) has the unique property of having 20 eV of internal energy. Experiments to produce Bose-condensates of ^{4}He* have thus far used laser cooling as the initial loading stage [102, 103, 104]. However, the number of ^{4}He* loaded into the magnetic trap is limited by both the low efficiency for exciting helium to the metastable state and the lower cooling rate of the 1083 nm transition as compared to the transitions used in cooling the alkali-metals. In this chapter, we describe experiments to produce, trap, and evaporatively cool He* from $\sim$ 1 K down into the ultracold regime. The advantage of larger trapped samples afforded to us by buffer gas loading should lead to larger condensates and facilitate novel experiments in quantum atom optics and cold molecular physics.

6.1 He* atomic structure

A summary of the properties of He* is presented in Appendix B. Here we detail the points relevant to our magnetic trapping experiments. Helium has two metastable

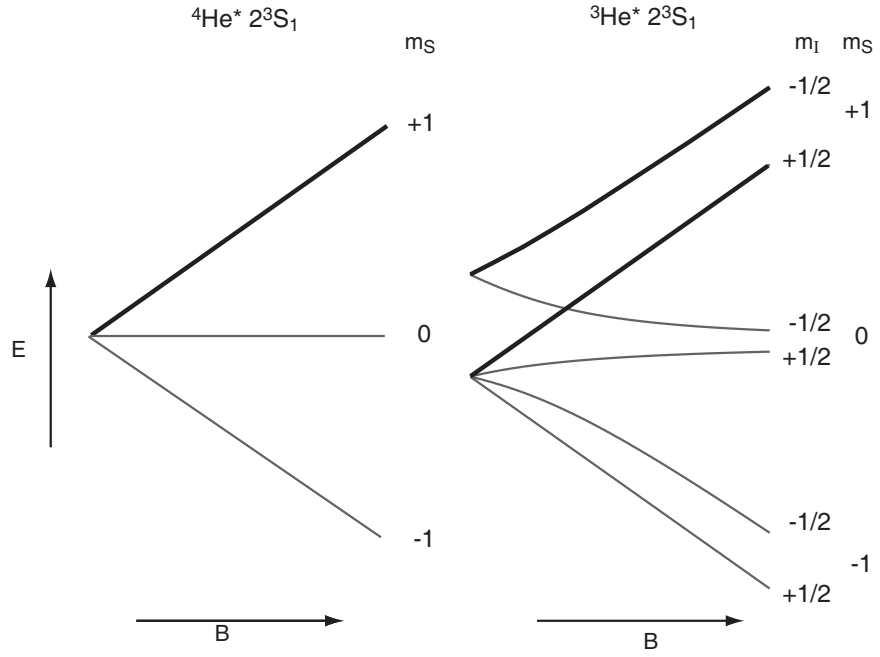

Figure 6.1: Zeeman structure of the 2^3S_1 state for ^{4}He* and ^{3}He*. Bold lines represents Zeeman states which can be magnetically trapped.

states, the singlet 2^1S_os state and the triplet 2^3S_1 state. As the singlet has no magnetic moment and therefore cannot be magnetically trapped, we concern ourselves with only the triplet state. The Zeeman structure of the triplet state for both ^{4}He* and ^{3}He* is shown pictorially in Figure 6.1. ^{4}He has no nuclear spin while ^{3}He has a nuclear spin of $I = 1/2$. We aim to trap the $|m_S = +1\rangle$ state which has a magnetic moment of $2\mu_\mathrm{B}$.

The excited triplet state is ~ 20 eV above the ground singlet state 1^1S_0. Because it decays via a M1 transition, it has a lifetime of 7900 s [105]. Therefore for all practical purposes the lifetime of this state is never an issue, and we can consider it like any other ground state atom.

6.1.1 Penning ionization

The 20 eV of internal energy does present one problem. As the binding energy is $\sim$ 24 eV, collisions between two He* atoms can lead to a process where one atom is ionized while demoting the other back down to the ground state. This process is known as Penning ionization (PI),

$$\mathrm{He}^* + \mathrm{He}^* \rightarrow \mathrm{He}^+ + \mathrm{He} + \mathrm{e}^- \tag{6.1}$$

In an unpolarized sample, PI leads to rapid depletion of He* atoms. The measurements of the rate constant for this process in ^{4}He* varies and ranges between 8×10^{-11} to 4×10^{-9} cm^3/s [106, 107, 108, 109, 80]. However, in a spin polarized sample, this process is suppressed due to conservation of angular momentum [110]. The total spin of the two He* is initially $2\hbar$; the maximum total spin of the byproducts of PI is $\hbar$. However, there still exists a second order process (dipolar relaxation induced PI) involving virtual transitions in the molecular levels during a collision where PI can still occur. Theoretical calculations by Shlyapnikov and coworkers predict that PI is suppressed for a spin polarized sample of ^{4}He* by atleast 5 orders of magnitude for temperatures from the ultracold up to 1 K [110, 111]. As a function of magnetic field, the PI rate is fairly constant up to 100 G but decreases dramatically by two orders of magnitude at 10 T.

For ^{3}He*, experimental data and theoretical calculations have been limited and are not in agreement. Single channel calculations and measurements with a laser-cooled, unpolarized sample ^{3}He* at 1 mK by Stas *et al.* yield a rate of 2×10^{-10} cm^3/s [107] while Kumakura *et al.* measure rates an order of magnitude larger [109]. Both studies suggest that the PI rate in an unpolarized sample is slightly higher for ^{3}He* samples than in ^{4}He* samples. Calculations however have not been made for a spin-

polarized sample of ^{3}He* where the hyperfine structure may play a significant role. The spin conservation argument suggests that PI would be similarly suppressed for ^{3}He* in its fully stretch $|m_S = +1, m_I = +1/2\rangle$ state. The degree of suppression though is unknown. Of particular interest is the rate constant for collisions with the $|m_S = +1, m_I = -1/2\rangle$ state. Because it would also be produced in the RF discharge and subsequently trapped along with the fully stretched state, a high rate constant would destroy the trapped sample.

6.1.2 Dipolar relaxation

In addition to PI, dipolar relaxation will also contribute to trap loss [111]. In dipolar relaxation, the collision of the two He* atoms in the $|m_S = +1\rangle$ state results in two He* atoms in the $|m_S = 0\rangle$ state with the angular momentum going into the orbital angular momentum. The process actually dominates PI at temperatures higher than 10 mK or fields higher than 100 G with an average rate constant of 10^{-14} cm^3/s. There is a magnetic field resonance at 750 G, increasing the rate constant up to 5×10^{-13} cm^3/s. These dipolar relaxation rates are an order of magnitude smaller than in chromium and are comparable to those in the alkali-metals.

6.1.3 Elastic collisions

As stated in Chapter 2, the efficiency of evaporative cooling depends on the ratio of the elastic to inelastic collision rates. He* has the benefit of having large elastic collisions rate due to two factors. The first is simply that its small mass gives rise to a high velocity. Second, because of the presence of a weakly bound molecular level, the elastic cross section in the ultracold regime is large. Photoassociation experiments of He* have determined a zero field s-wave scattering length of 7 nm [112], slightly

larger than observed in the alkali-metals. The elastic rate constant is greater than 10^{-9} cm^3/s for temperatures above the s-wave cutoff at ~ 10 mK and falls off as $\sqrt{T}$ for temperatures below that. Likewise the ratio of elastic to inelastic collision rate is $\sim 10^5$ for temperatures above 10 mK and drops to to $\sim 5 \times 10^3$ at 1 μK, boding well for evaporative cooling [111]

6.2 He* production

Metastable helium is produced via an RF discharge in the cryogenic apparatus described in Chapter 5. Generally, the valve is initially closed and the trapping region of the cell is filled with He gas by temporarily heating the fill line sorb to temperatures higher than 8 K. Typical He densities range from 10^{15} to 10^{16} cm^{-3}. The cell can be filled with either ^{3}He or ^{4}He.

The source of the RF for the discharge is an RF generator which is then sent into an RF amplifier capable of generating 50 W of RF power. The RF is then coupled into the copper coil surrounding the trapping region. Because of the relative proximity of metal objects, RF pulses of only a few hundred microsecond are used to avoid inducing unwanted eddy current heating. With RF powers of 10-50 W, these pulses have energies comparable to the optical pulses used to produce atoms via laser ablation.

Unfortunately, the RF discharge cannot be reliably ignited with solely the RF pulse. We use a 5 ns, 1 mJ pulse from a frequency-doubled Nd:YAG laser focused onto a small sample of thulium to create an ablation plume to reliably ignite the discharge. At this energy, the laser pulse does not produce any detectable thulium atoms. Given our signal to noise, we can place an upper bound of 10^8 thulium atoms. The spin relaxation rate due to collisions with helium atoms is also relatively fast at

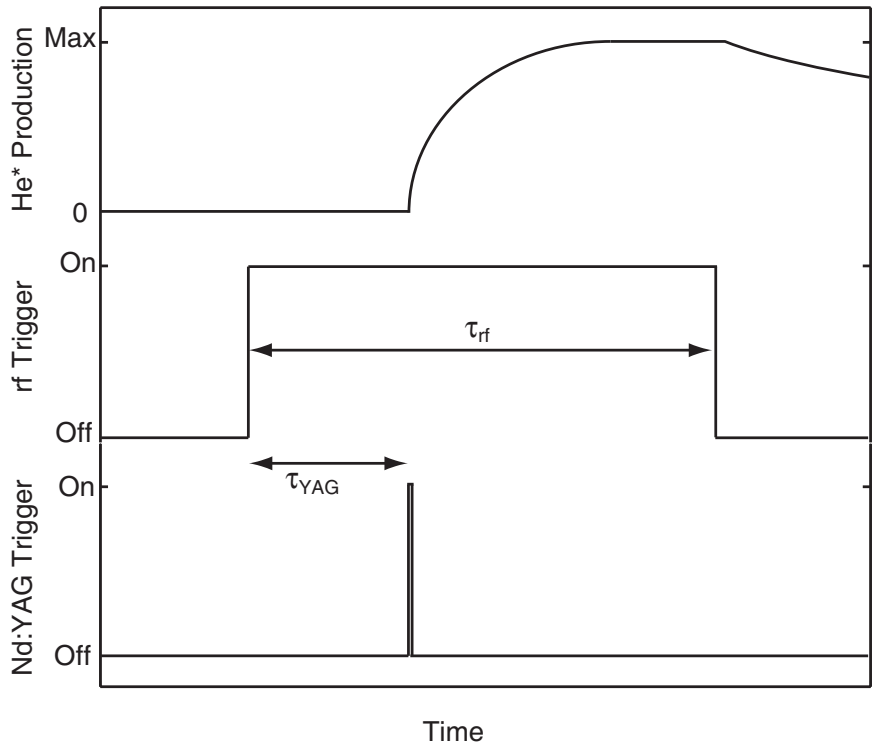

Figure 6.2: Discharge timing sequence. Parameters used in the magnetic trapping experiments are $\tau_{\rm RF} = 150$ μs and $\tau_{\rm YAG} = 50$ μs.

10^{-13} cm^3/s [27]. Thulium atoms not already lost to diffusion would be ejected from the magnetic trap in less than 10 ms. In addition, the lifetimes of the He* are in agreement with loss due solely to diffusion.

6.2.1 Pulse sequence

The He* production sequence is illustrated in Figure 6.2. At $t = 0$ an RF pulse of duration $\tau_{\rm RF}$ is generated. After a delay of $\tau_{\rm YAG}$, the laser pulse from the Nd:YAG is focused on the thulium sample. Because of delays in the electronics, we set $\tau_{\rm YAG} = 50$ μs to ensure that the Nd:YAG pulse is coincident with the RF pulse. He* is produced at $t = \tau_{\rm YAG}$, and the maximum production is reached after ~ 50 μs. The RF pulse duration used in all the experiments is $\tau_{\rm RF} = 150$ μs.

6.2.2 Production numbers

Based on the absorption at zero magnetic field, upwards of a few times 10^{12} He* are produced during every RF pulse. This number is consistent with previously reported efficiencies of He* production in RF discharges [80, 106]. The production is strongly dependent on the RF frequency with an optimal frequency range of ~ 5 MHz. This optimal frequency and width varies with temperature but is steady once a stable temperature is reached. For instance, at 50 K He* can be produced in the frequency range of 75-115 MHz and 122-128 MHz. At 400 mK, the frequency range changes to 90-120 MHz, with an optimal frequency of 118 MHz which we use for the magnetic trapping experiments.

The production of He* is fairly constant over a buffer gas range of 10^{15} to 10^{16} cm^{-3}, indicating that the efficiency for He* production is inversely proportional to the buffer gas density. Above and below this range, a discharge cannot be maintained. The range also coincides with the buffer gas density needed for thermalization of atoms produced via laser ablation, making it possible to simultaneously produce and trap both He* and other species [24]

6.2.3 Discharge revivals

At 50 K after being able to initiate the discharge with an RF and focused Nd:YAG pulse, we find it possible to re-initiate the discharge with additional RF pulses without the need for additional Nd:YAG pulses. An example of this behavior is shown in Figure 6.3. The discharge and He* production is revived by each additional RF pulse, shown here to be separated by 1 ms. In addition, with each additional pulse, the total number of He* produced also increases.

One advantage of this method is that the He* production can be maintained as

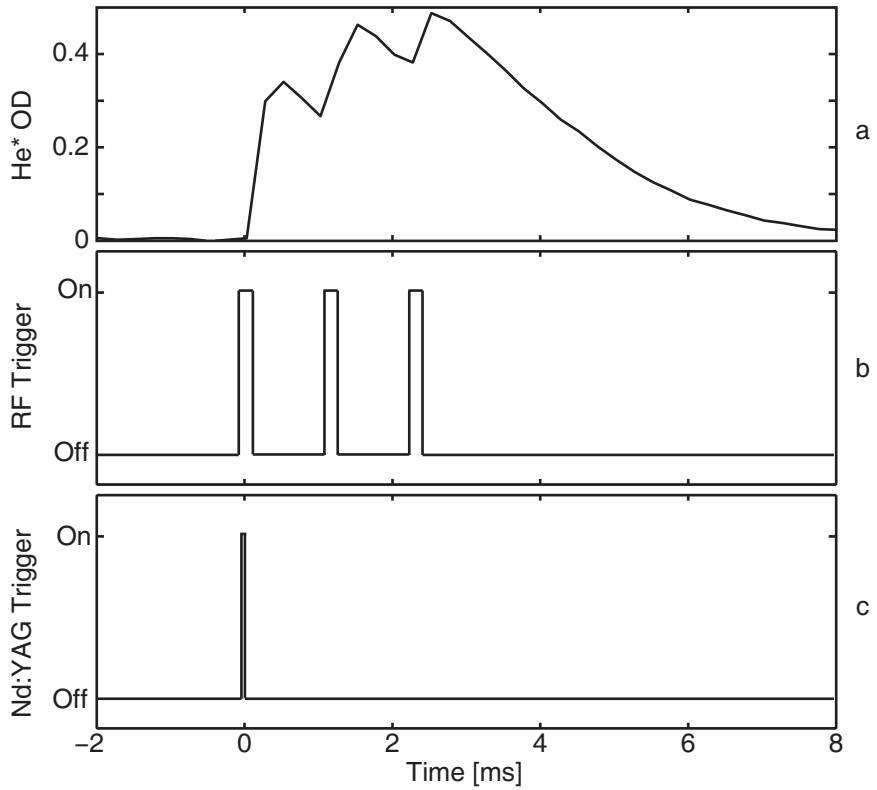

Figure 6.3: Timing sequence for discharge revivals. a) Optical density of He* produced in the cell. b) Trigger signal sent to RF switch. Pulses are 150 μs long and are separated by 1 ms. c) Trigger signal sent to Nd:YAG.

the cell and helium gas cool down from the heat generated by the Nd:YAG pulse. This would improve the number of He* atoms that are magnetically trapped after the buffer gas is removed. The second advantage is the increase in the number of He* atoms produced with each successive RF pulse. Unfortunately, the effectiveness of the multiple pulse sequences declines as the temperature decreases. At 4 K there is only a faint hint of a revival, and at 400 mK we are unable to re-initiate the discharge without an Nd:YAG pulse. There may likely exist a small parameter space in which this revival is still favorable at low temperatures, and further exploration may prove beneficial for magnetic trapping.

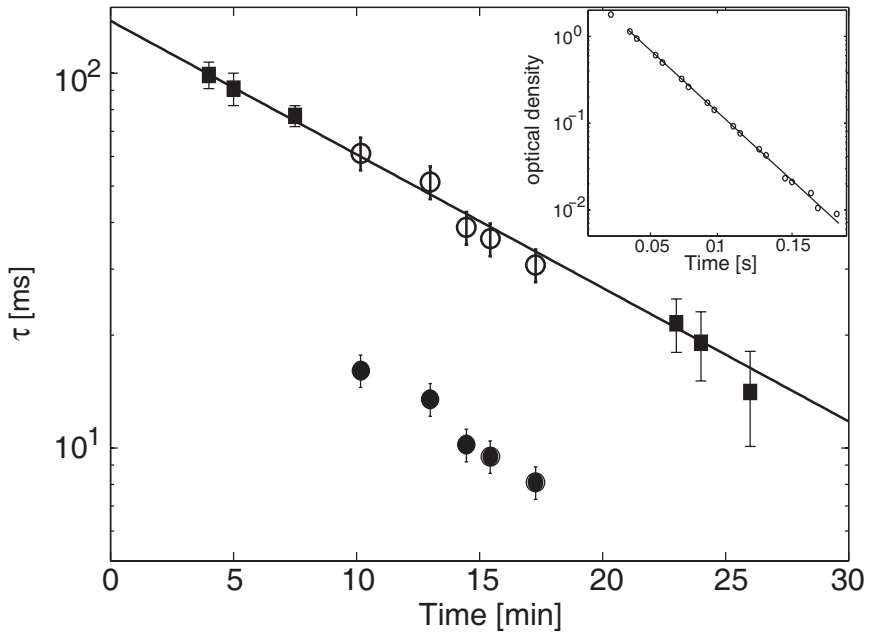

Figure 6.4: Lifetimes of ^{4}He* and Mn* in the absence of magnetic fields as a function of the time after filling the cell with helium buffer gas. The squares are lifetimes for manganese. The solid circles are lifetimes for ^{4}He*. The open circles are lifetimes for ^{4}He* scaled by 3.8 to match the lifetimes of manganese. The line is a fit to the time dependence of lifetimes for manganese. Insert: Decay of ^{4}He*. Shown is the optical density of ^{4}He* as a function of time along with an exponential fit.

6.3 He*-He collisions

Once the He* atoms are produced, they undergo multiple collisions as they diffuse through the background helium gas and are lost at the cell walls. By measuring the lifetime of the ^{4}He* atoms in the absence of magnetic fields, we can determine the ^{4}He*-^{4}He collision cross-sections. This is done by fitting the decay of the ^{4}He* population to an exponential loss as shown in the insert of Figure 6.4. Unfortunately the helium buffer gas density slowly decreases after the cell is filled. To calibrate the helium density, we also measure the diffusion lifetime of laser ablated manganese whose Mn-He elastic cross-section is known to be 1.0×10^{-14} cm^2 [113].

Figure 6.4 plots the measured lifetime for both ^{4}He* and manganese as a function

of time after the cell is filled with helium buffer gas. Measurements of the ^{4}He* lifetime are made between the measurements of the diffusion lifetime of manganese. The lifetime of the manganese atoms indicates that the helium buffer gas is slowly leaking out of the trapping region with a time constant of ~ 12 min, as expected. The measured lifetime for ^{4}He* is much lower. The decrease in the lifetime as the helium density decreases indicates that there is no collision induced loss such as de-excitation.

If we assume that the decay of He* is due solely to diffusion we can determine the elastic collision cross-section by comparing with the decay of manganese. Because the diffusion lifetimes are linearly proportional to the elastic cross-section, we find σ_{el} is $2.6(+3/-1) \times 10^{-15}$ cm^2, four times smaller than that of manganese [113]

6.4 Magnetic trapping of He*

6.4.1 Number trapped

We magnetically trap He* by running the RF discharge with the magnet energized. In all the experiments, the magnet is fully energized at a current of 102 A. This corresponds to a trap depth of 3.67 T at the cell walls or $U_{\rm trap} = 4.9$ K for an atom with a magnetic moment of $2\mu_{\rm B}$. The cell temperature is ~ 400 mK.

Under these conditions, we are able to trap upwards of 10^{12} He* atoms in the $|m_S = +1\rangle$ state at densities of 10^{12} cm^{-3}. For ^{3}He* we trap both hyperfine states $|m_S = +1, m_I = \pm 1/2\rangle$. While other m_S states are likely also produced in the discharge, they would be lost to diffusion and Penning ionization too rapidly to be detected by our electronics. Figure 6.5 shows the Zeeman broadened spectra of trapped ^{4}He* and ^{3}He*.

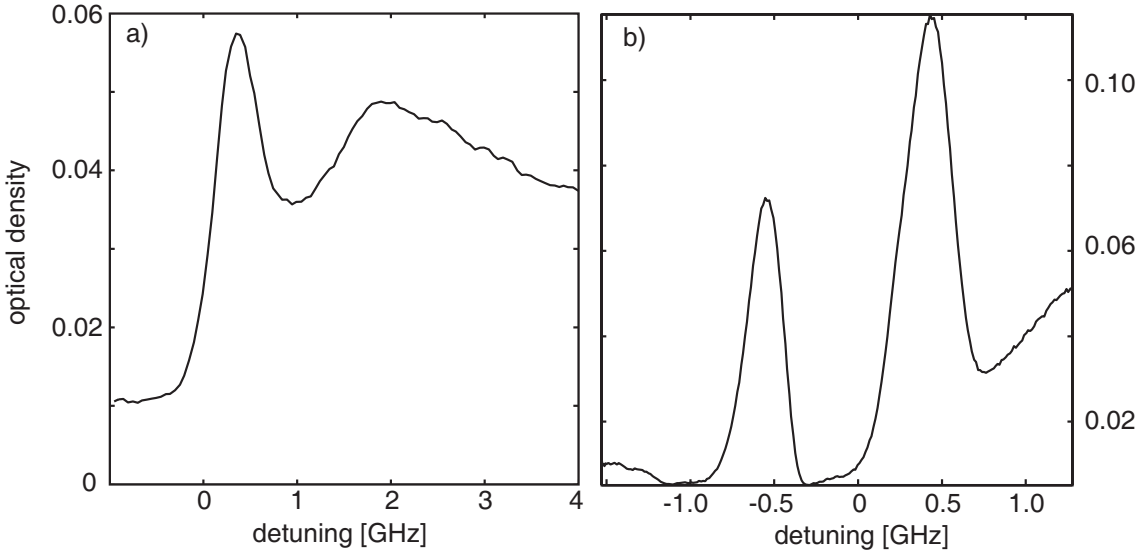

Figure 6.5: Spectra of trapped He*. a) Spectra of trapped ^{4}He*. The left peak is the $\Delta m = 0$ transition while the broad feature on the right is the $\Delta m = +1$ transition. b) Spectra of trapped ^{3}He*. Left most peak is $\Delta m = 0$ transition from the $|m_S = +1, m_I = -1/2\rangle$ state. The right peak is $\Delta m = 0$ transition from the $|m_S = +1, m_I = +1/2\rangle$ state.

6.4.2 Penning ionization in ^{3}He*

The production and numbers trapped are similar for both ^{4}He* and ^{3}He*. However once the background helium gas is removed, they behave quite differently. Shown in Figure 6.6 is the population of both species as a function of time. After being initially trapped at t=0, ^{4}He* decays slowly with a time constant of hundreds of seconds. For the same experimental parameters, however, there is rapid trap loss for the ^{3}He* sample. Within two seconds of being trapped, the number of trapped ^{3}He* is reduced by a factor of five.

The decay shown in Figure 6.6 is for the $|m_S = +1, m_I = +1/2\rangle$ state of ^{3}He*. We also trap the $|m_S = +1, m_I = -1/2\rangle$ state. Figure 6.7 shows the decays of both $|m_S = +1, m_I = \pm 1/2\rangle$ states after they are simultaneously loaded into the trap. The $|m_S = +1, m_I = -1/2\rangle$ state experiences an even faster decay. In addition,

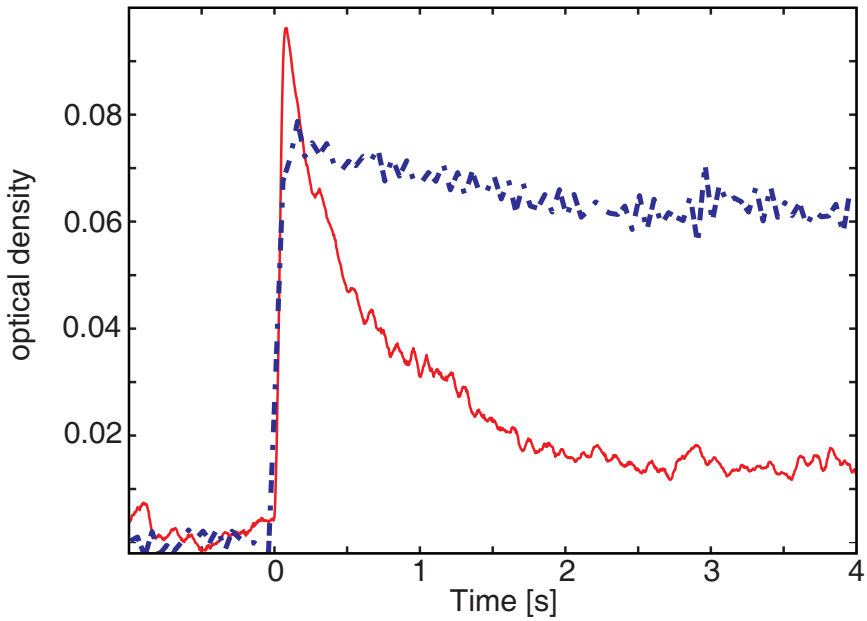

Figure 6.6: Decay of He* after being initially trapped at $t = 0$. The dotted line is the optical density of trapped ^{4}He*. The solid line is the optical density of the $|m_S = +1, m_I = +1/2\rangle$ state of trap ^{3}He*. The experimental parameters in both cases are the same.

the levelling off of the $|m_S = +1, m_I = +1/2\rangle$ coincides with the depletion of the $|m_S = +1, m_I = -1/2\rangle$ state. The trap loss for both states could be due to Penning ionization. As stated earlier in the chapter, PI is suppressed in a spin polarized sample. This is not however the case for our ^{3}He* sample. Collisions between atoms in the $|m_S = +1, m_I = -1/2\rangle$ state with either hyperfine state can result in PI and lead to the the same spin purification of the trapped sample as that seen in Figure 6.7. If we attribute this loss solely to PI, the dynamics of the two states can be described by the following rate equations,

$$\dot{n}_a = -\Gamma_{a,b} n_a n_b \tag{6.2}$$

$$\dot{n}_b = -\Gamma_{a,b} n_a n_b - \Gamma_{b,b} n_b^2, \tag{6.3}$$

where n_a is the density of the $|m_I = +1/2\rangle$ state, n_b is the density of the $|m_I = -1/2\rangle$ state, $\Gamma_{a,b}$ is the PI rate constant collisions between atoms of state $|m_I = +1/2\rangle$

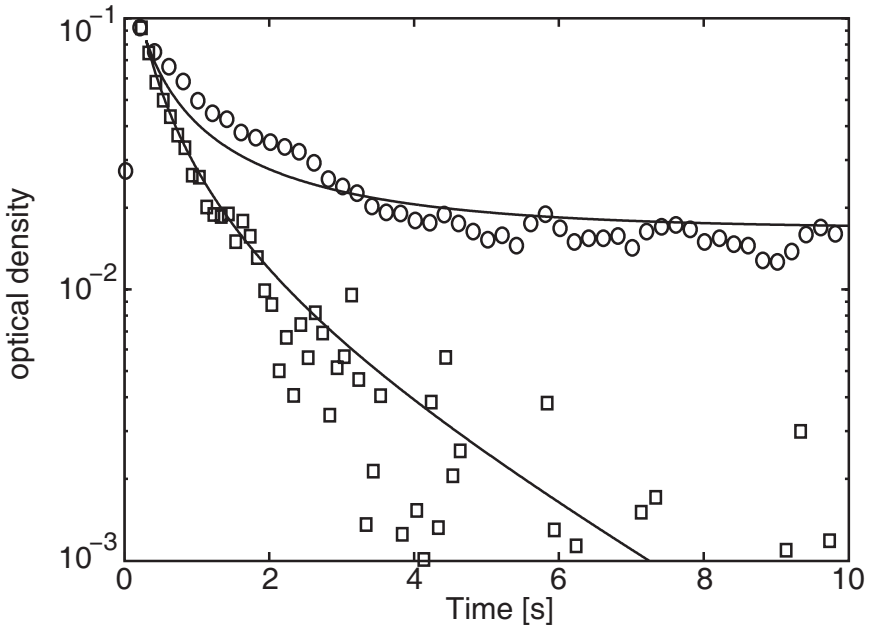

Figure 6.7: Penning ionization in ^{3}He*. The circles represent the decay of the $|m_S = +1, m_I = +1/2\rangle$ state. The squares represent the decay of the $|m_S = +1, m_I = +1/2\rangle$ state. The solid lines are from a least squares fit to Eqs. 6.2 and 6.3.

and state $|m_I = -1/2\rangle$, and $\Gamma_{b,b}$ is the rate constant for collisions between two $|m_I = -1/2\rangle$ atoms. A least squares fit of the decay of both $|m_I = \pm 1/2\rangle$ states yields PI rate constants of $\Gamma_{a,b} = 1 \times 10^{-10\pm1}\mathrm{cm}^3/\mathrm{s}$ and $\Gamma_{b,b} = 5 \times 10^{-11\pm1}\mathrm{cm}^3/\mathrm{s}$. The fit though not perfect does reproduce the behavior of the measured data fairly well. The $|m_I = -1/2\rangle$ states is completely depleted while the $|m_I = +1/2\rangle$ levels off.

The measured rate constants are consistent with previously measured PI rates for ^{3}He* [107, 109]. However our data is taken at different experimental conditions. Because we have an electronically polarized sample ($|m_S = +S\rangle$) and are in the high-field limit, we would naively expect that PI would be suppressed. However similar to the case seen in manganese (Chapter 4), the $|m_S = 1, m_I = -1/2\rangle$ state will have a small admixture ϵ of the $|m_S = 0, m_I = +1/2\rangle$. ϵ depends on the magnitude of the hyperfine coupling relative to the Zeeman energy and is proportional to $A/(g_e\mu_\mathrm{B}B)$

where A is the hyperfine coupling constant [69, 70]. Therefore two ^{3}He* inside our trap will be sampling both the $S = 2$ and $S = 1$ internuclear potentials, opening up a channel for PI to occur. The theory presented in References [107, 114] may be able to be extended to consider this particular set of collisions.

Because of the number of ^{3}He* atoms lost in the first few seconds, the absorption signal from the remaining atoms while scanning the laser frequency is comparable to the noise. This ratio of signal to noise limits how well we can spectroscopically measure the temperature of the trap sample. Because of this, we focus our attention on the evaporative cooling of ^{4}He* where the signal to noise does not present a problem. Further studies of ^{3}He* should be done in the future to elucidate the particular processes that lead to PI in ^{3}He*.

6.5 Solving the film problem

Evaporative cooling of ^{4}He* to lower temperatures is now possible. We have a thermally isolated sample at high densities. The ensuing high elastic collision rates are a necessary component to efficiently evaporate from our starting phase space density of 10^{-10}.

6.5.1 Film problem

Unfortunately, we have trap loss due to collisions with background helium gas. After magnetically trapping the ^{4}He* atoms, the valve is opened, and the buffer gas is pumped out of the trapping chamber onto the charcoal sorb. Although this removes the bulk of the buffer gas from the trapping chamber, the desorption of ^{4}He* atoms from a film that coats the cell walls provides an influx of ^{4}He atoms into the cell

volume. A simulation of the desorption of ^{4}He atoms from the film is shown in Figure 6.8. Details of the simulation can be found in Reference [30, 65]. Even though the buffer gas is initially pumped out with a 50 ms time constant, this desorption from the film provides an influx of 10^{12} ^{4}He atoms/s into the cell volume, resulting in a roughly constant background density of $\sim 10^{10}$ cm^{-3}. At this density, the lifetime of the trap sample is $\sim$ 10 s, too short for efficient evaporation. This film can be thinned by "baking out" the cell, i.e. by bringing the temperature of the cell up to 650 mK while the atoms remain trapped (Fig. 6.8). Although this lowers the background gas levels, it works well only for species with large magnetic moments such as chromium (6 μ_B) [30]. A 2 μ_B species like ^{4}He* is blown out of the trap by the hot helium during such a bake out procedure.

6.5.2 Production with the valve open

Unexpected but advantageous, we are able to produce and trap a substantial number of He* with the valve open. In Figure 6.9, the maximum number of ^{3}He* trapped is plotted as a function of the time after filling the trapping chamber with buffer gas. In addition, the valve closing pressure is decreased at the specified times to efficiently access a wide range of buffer gas densities. Though we do not know the functional form of how the buffer gas density in the cell varies with time, it ranges from 10^{16} cm^{-3} at the beginning of the measurement to a 10^{10} cm^{-3} at the end of the measurement.

For our experimental parameters, there is an optimal buffer gas density for trapping of He*. We believe this to be at $\sim 10^{15}$ cm^{-3}. Of particular interest though is the production and trapping once the valve is completely open. We are able to trap a few times 10^{11} ^{3}He* atoms, only a factor of 3 less than at the optimal buffer

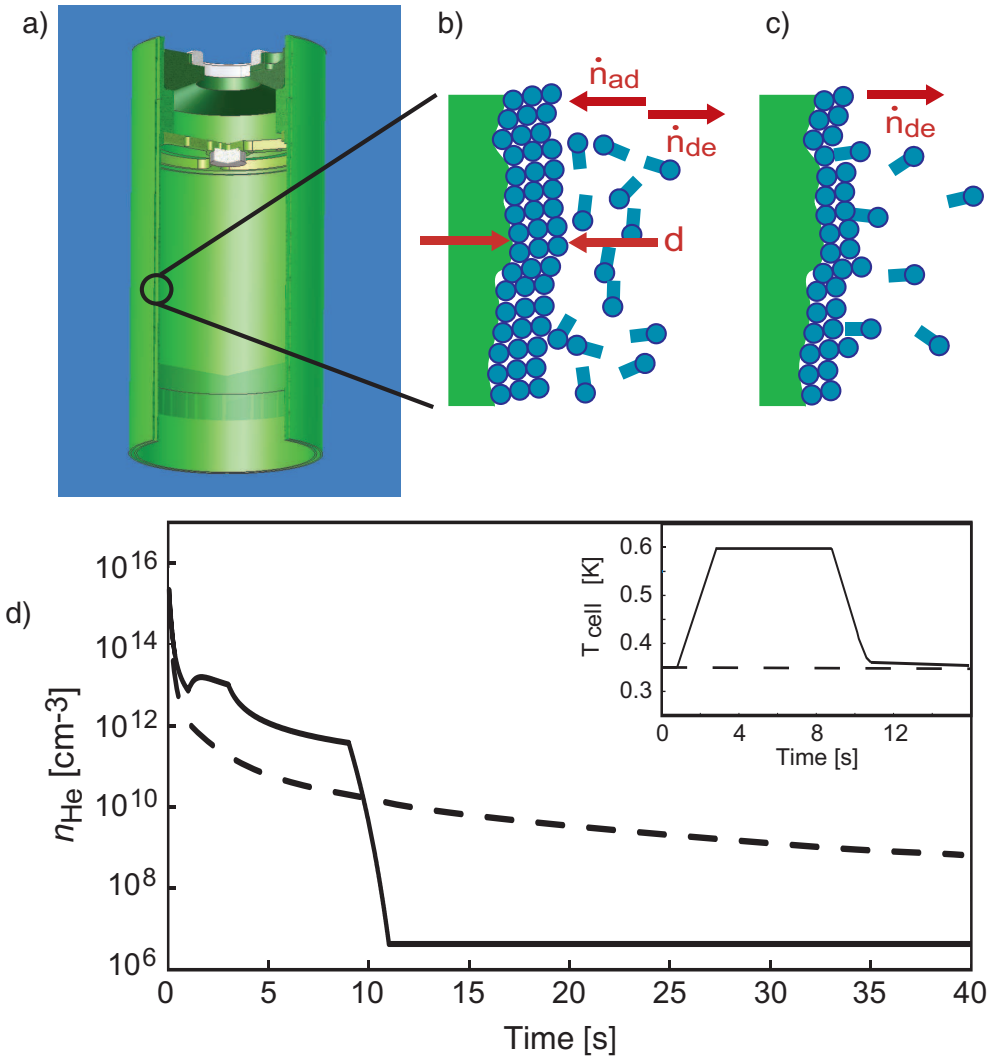

Figure 6.8: Film problem. a) Cut away of the trapping chamber. A thin film of helium resides on the cell walls. b) With the valve closed, the adsorption $\dot{n}_{\rm ad}$ and desorption $\dot{n}_{\rm de}$ of helium atoms results in an equilibrium film thickness d. c) With the valve open, helium atoms desorb from the film to replace the gas that is pumped away. d) Simulation of the helium density in the trapping chamber taking into account the film desorption. The valve is opened at $t = 0$. The dashed line is for a constant cell temperature. The solid line represents a "bake out" procedure.

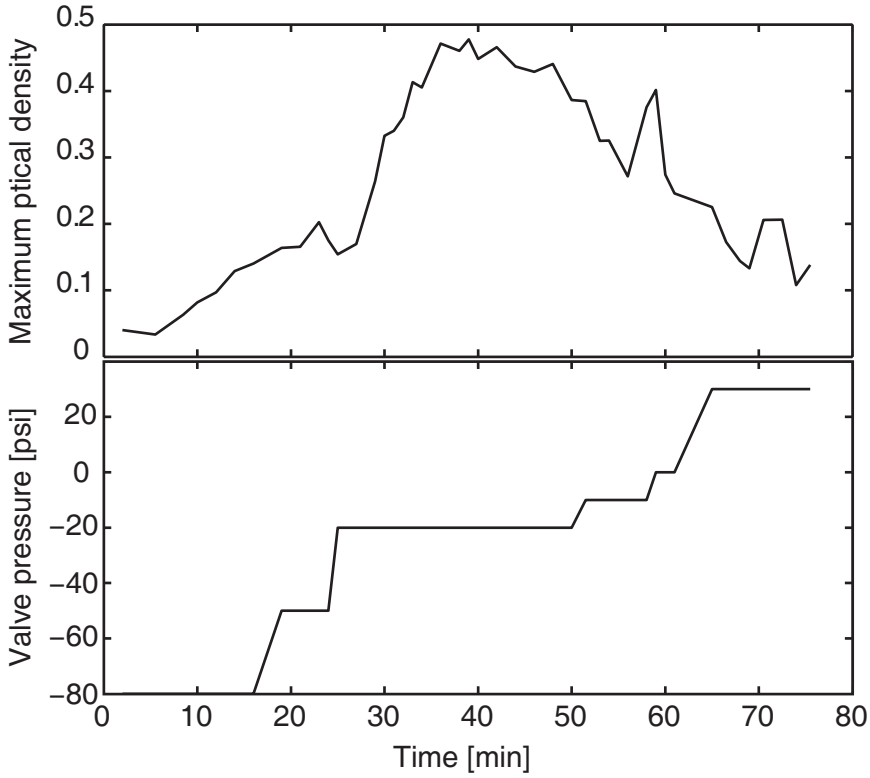

Figure 6.9: Dependence of the number of ^{3}He* trapped on the buffer gas density. a) Maximum optical density of trapped ^{3}He* as a function of time after filling the trapping chamber with buffer gas. b) The valve closing pressure. For negative pressures, the valve is closed; positive pressure means an open valve. The buffer gas density is $\sim 10^{16}$ cm^{-3} at $t = 0$ and decreases to 10^{10} cm^{-3} at $t = 75$ min.

gas density. Given typical RF discharge efficiencies of 10^{-5}, the number of ^{3}He* that are magnetically trapped implies an initial ^{3}He density in the cell of $> 10^{14}$ cm^{-3}, a number far too large to be accounted for by the equilibrium background ^{3}He density in the cell. We believe the source of this large density is rapid desorption of ^{3}He atoms from the cell walls due to local heating of the cell by the RF pulse; after this initial large influx of the atoms, those atoms not converted into ^{3}He* and trapped are cryopumped back to the cell walls with a time constant of ~ 1 ms. Similar behavior and numbers are seen for ^{4}He*.

6.5.3 Reducing background gas density

The ability to trap He* with the valve open is advantageous because it opens up a new method to addressing the trap loss due to the high density of background helium gas. The new method begins by filling the trapping chamber to a density of $\sim 10^{15}$ cm^{-3} of ^{4}He with the valve initially closed. After a short wait while the ^{4}He gas comes into equilibrium with the cell, the valve is opened. The ^{4}He gas is pumped away, leaving behind a ^{4}He film that coats the cell walls and is the source of unwanted background gas. The cell is then heated to 700 mK for 30 s, driving weakly bound monolayers off the film. The remaining few monolayers are more tightly bound to the surface, lowering the effective vapor pressure and reducing the background density to $< 10^6$ cm^{-3}. At this density, the loss rate from collisions with background ^{4}He gas is negligible. With the "prepared" cell, ^{4}He* is then produced in the discharge, and we are able to trap 10^{11} ^{4}He* at densities of 10^{11} cm^{-3}. Although this method of producing ^{4}He* reduces the number of atoms initially trapped by roughly an order of magnitude compared to using a buffer gas filled cell, it reduces the background gas density sufficiently to enable efficient evaporative cooling.

6.6 Evaporative cooling of ^{4}He*

Armed now with both high densities of trapped ^{4}He* and low background gas density, we begin evaporative cooling in an attempt to progress towards quantum degeneracy.

6.6.1 Evaporation against the window

When the ^{4}He* atoms are initially loaded, the trap depth U_{trap} is set by the cell walls. Evaporative cooling of chromium described in Chapter 3 was achieved by

lowering the depth of the magnetic trap at the cell walls. The chromium atoms were cooled by both adiabatic expansion and forced evaporation. One disadvantage of this method was the reduction of the confinement as the trap depth was lowered. The high densities needed for high collision rates were not maintained during the process. As shown in Figure 3.8, the density dropped two orders of magnitude as the trap depth was lowered. The phase space density, the figure of merit for reaching quantum degeneracy, increased marginally but remained at the 10^{-11} level [48].

This confinement problem is generally avoided by using an RF knife to set the trap depth [34, 32]. The confinement is defined by the magnetic trap and is independent of the trap depth. Unfortunately, an RF knife is unfeasible with our experimental parameters. At the initial trap depth and temperature, the resonant frequency to eject the higher energy atoms is in the microwave range. Second, hundreds of Watts of power is required to efficiently drive these transitions.

In this experiment, we evaporate by lowering the trapped ^{4}He* towards the surface of the cell window. This is possible by independently controlling the currents in the two coils. ^{4}He* atoms that hit the window are lost through adsorption. Because the atoms at the edge of the cloud have higher energy than the average energy of an atom in the cloud, evaporative cooling occurs. This adsorption method has been previously demonstrated with both H [36] and Rb [35]. In this method, the trap depth is decoupled from the confinement. The trap depth is determined by the distance between the trapped sample and the cell window, set by the ratio of the two coils currents, whereas the confinement is set simply by the magnitude of the bottom coil current. This allows for tight confinement and therefore larger ^{4}He*-^{4}He* collision rates.

Examples of magnetic field profiles for an evaporation trajectory is shown in Fig-

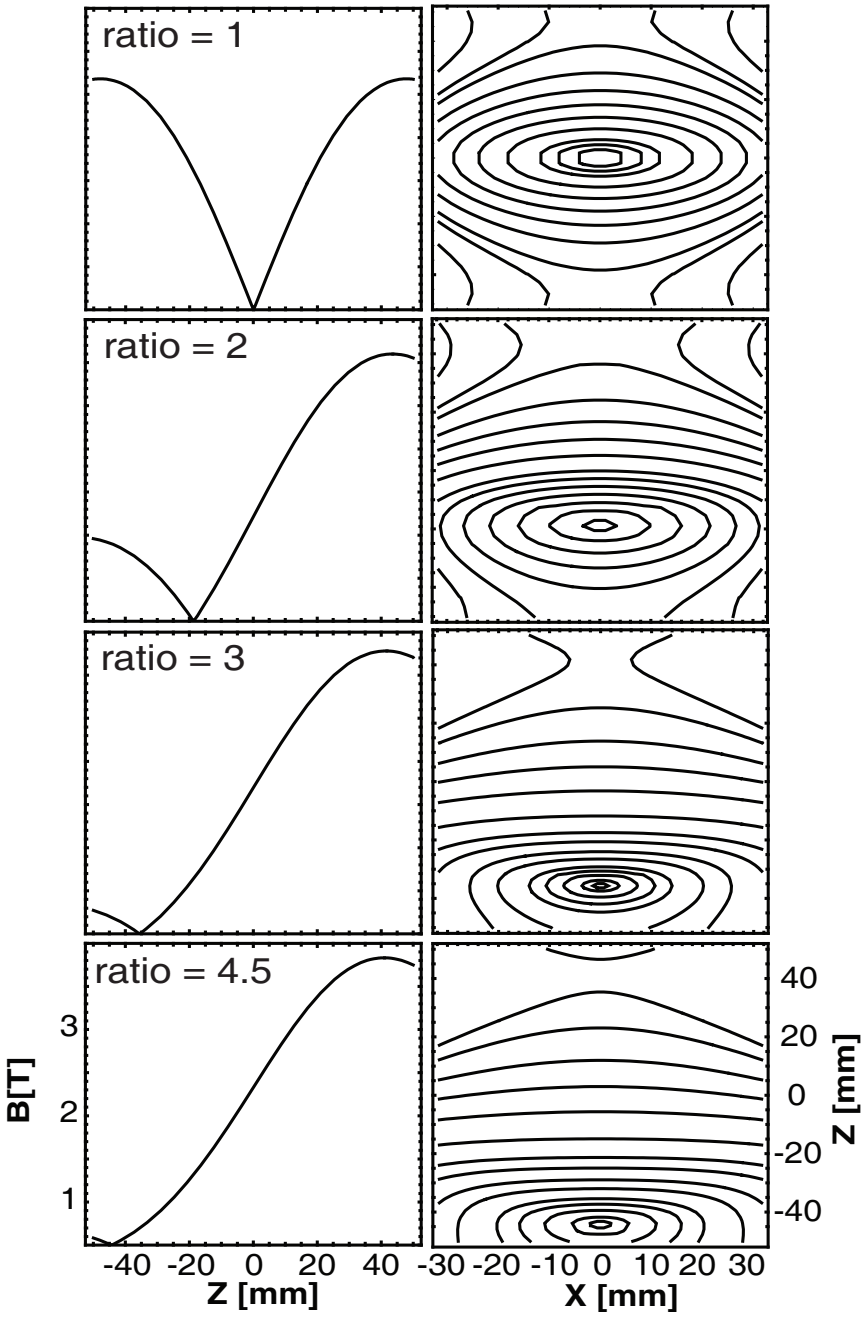

Figure 6.10: Magnetic field profiles for various ratios of the current in the two magnet coils. The cell window is located at $Z = -4.999$ cm.

Table 6.1: Comparison of the magnetic field gradients for evaporation against the window $B'_{\rm win}$ versus uniformly lowering the trap depth $B'_{\rm uni}$. The numbers for evaporation against the window are for a top current of 50 Amps and corresponds to the magnetic field profiles shown in Figure 6.10. $B'_{\rm uni}$ is the gradient at the specified $U_{\rm trap}$ assuming a cell radius of 3.16 cm.

Ratio	$U_{\rm trap}$ [K]	$B'_{\rm win}$ [G/mm]	$B'_{\rm uni}$ [G/mm]
1	2.4	570	570
2	1.1	270	270
3	0.36	130	80
4.5	0.005	64	1.1

ure 6.10. The trap shape is only minimally affected during the evaporation procedure and remains linear near the trap center. Details of the trap shape are presented in Appendix A. Table 6.1 compares the gradients for this evaporation method with the method of uniformly lowering the trap depth. For current ratios 1 and 2, the distance from the trap center and window is still greater than the cell radius. Therefore the gradients of the two methods are equivalent. The advantage arises at higher ratios when the trap depth is now defined by the cell window. At 5 mK, the confinement is 60 times greater when evaporating against the window. Since elastic collision rates depend on the cube of the gradient, this will significantly enhance the evaporative cooling process.

6.6.2 Locating the window

To determine the trap depth and the proper evaporation trajectory, it is essential to determine the location of the cell window relative to the superconducting magnets. Because of the complexity of assembling the apparatus plus the differential contraction

at cold temperatures, we locate the position of the window spectroscopically. After loading the ^{4}He* at 102 A, both magnet coils are ramped to 75.57 A. The top coil current is held constant as the bottom coil is ramped down, lowering the trapped sample towards the window. This is done for varying bottom coil currents, and we detect the presence of trapped ^{4}He*. A null signal implies that the location of the trap center is within (or below) the cell window. We determine the location of the cell window to correspond to a top coil current of 75.57 A and a bottom coil current of 16.7 ± 0.02 A. To check the results, we repeat the measurement with the top coil at 30.23 A. The corresponding bottom coil current for the window location is 6.77 ± 0.05 A. From these two sets of numbers, the cell window is located 4.999 ± 0.001 cm from the original center of the magnetic trap.

In the process of locating the window, we are evaporatively cooling, though very inefficiently. This is seen in the spectroscopic data shown in Figure 6.11. Because the degree of Zeeman broadening depends on the temperature of the trap sample, the spectrum for coil current ratio 17/75 is colder than the coil current ratio 17.5/75.

6.6.3 Evaporation Trajectory

The evaporation trajectory starts with the trapped sample 5 cm ($U_{\mathrm{trap}} = 4.9$ K) from the cell window (Fig. 6.13). The radial (axial) gradient is 1.15 (2.3) T/cm. Because the ^{4}He* is loaded right below the critical current of the superconducting magnetic trap, both coils are simultaneously ramped down to 75 A from 102 A to avoid quenching the magnet. The ramp rate is 1 A/s. Ramp rates faster than 2 A/s lead to eddy current heating causing an increase in the background gas density leading to trap loss, described in Chapter 5.

From 75 A, the coils are asymmetrically ramped down. The evaporation tra-

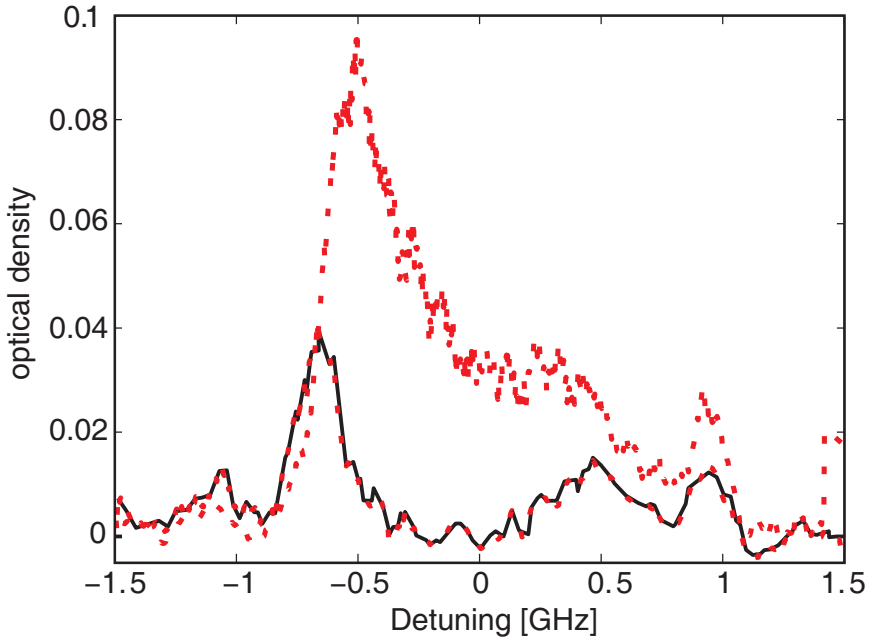

Figure 6.11: Spectra taken of cold ^{4}He* while locating position of the cell window. The dashed line is a spectrum taken for $I_{\rm top} = 75.57$ A and $I_{\rm bot} = 17.5$. The solid line is the spectrum taken for $I_{\rm top} = 75.57$ A and $I_{\rm bot} = 17$ A.

jectory is empirically optimized. For our coldest trapped sample and largest increase in phase space density, the trajectory is shown in Figure 6.12. Over 215 s, the trap center is gradually ramped towards the cell window to a final separation of 580 μm ($U_{\rm trap}$=2.7 mK) and radial (axial) gradient of 200 (400) G/cm, resulting in a trapped sample of $N = 2 \pm 0.5 \times 10^9$ ^{4}He* atoms with a peak density of $n_o = 2.3 \pm 0.2 \times 10^{12}$ cm^{-3}, and temperature of $T = 1.4 \pm 0.2$ mK (Fig. 6.13b). N, n_o, and T are determined by fitting the trapped atoms' Zeeman-broadened absorption spectrum to that of a spatial Boltzmann distribution of atoms in our magnetic trap, as described in Ref. [48, 66]. During most of the evaporation, the ratio of the trap depth to temperature defined as $\eta \equiv \mu_{\rm B} B / k_{\rm B} T$ is ~ 5. Only during the final stages of evaporation down to ~ 1 mK is this ratio observed to be reduced to two.

At the coldest temperature of 1.4 mK, the corresponding phase space density is

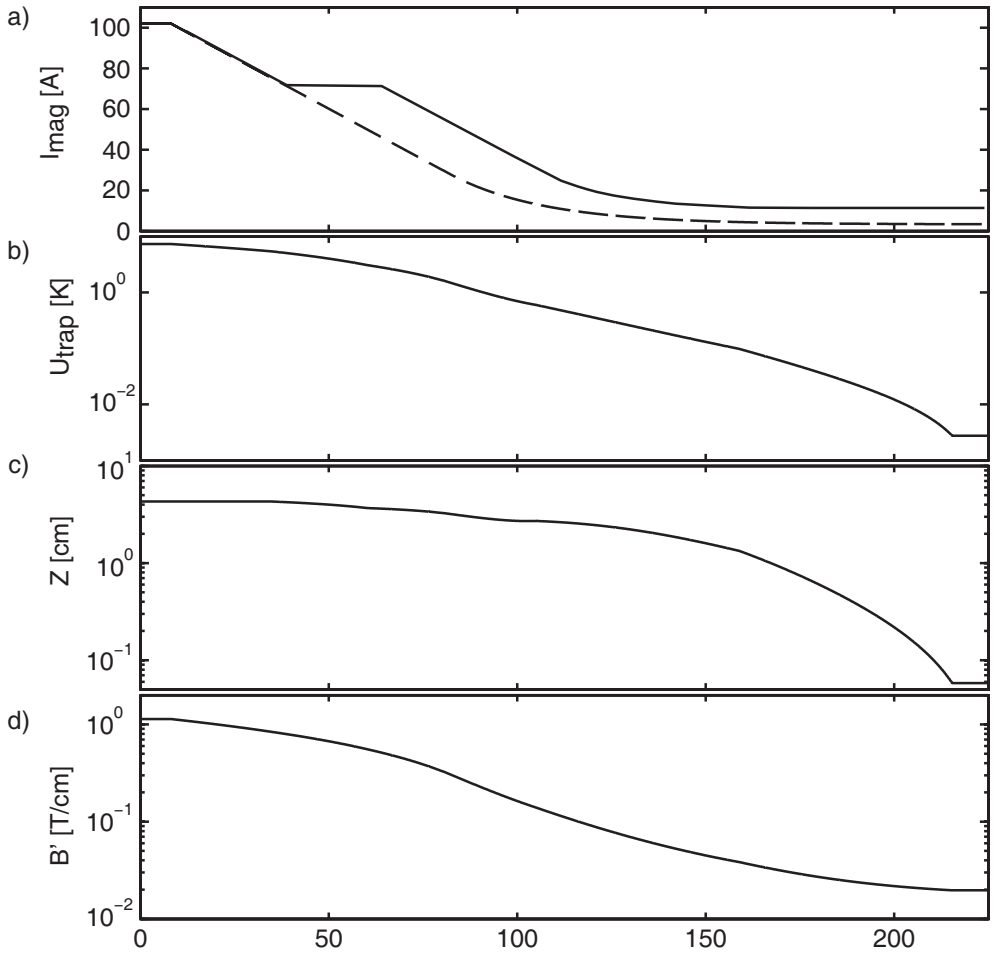

Figure 6.12: Parameters for optimal evaporation trajectory a) Current in the magnet coils. The solid line is for the top coil. The dashed line is for the bottom coil. b) The trap depth $U_{\rm trap}$. c) The distance from the cell window Z. d) The radial gradient.

3×10^{-5}, an increase of 5 orders of magnitude over the initial loading conditions. The efficiency of the evaporation implies a favorable ratio of elastic to inelastic cross-section in the multi-partial wave regime and down into the ultracold regime, confirming the calculation of Shlyapnokov *et al.* [110, 111]. There is no indication of shape resonances or other unpredicted mechanisms that would lead to substantial trap loss.

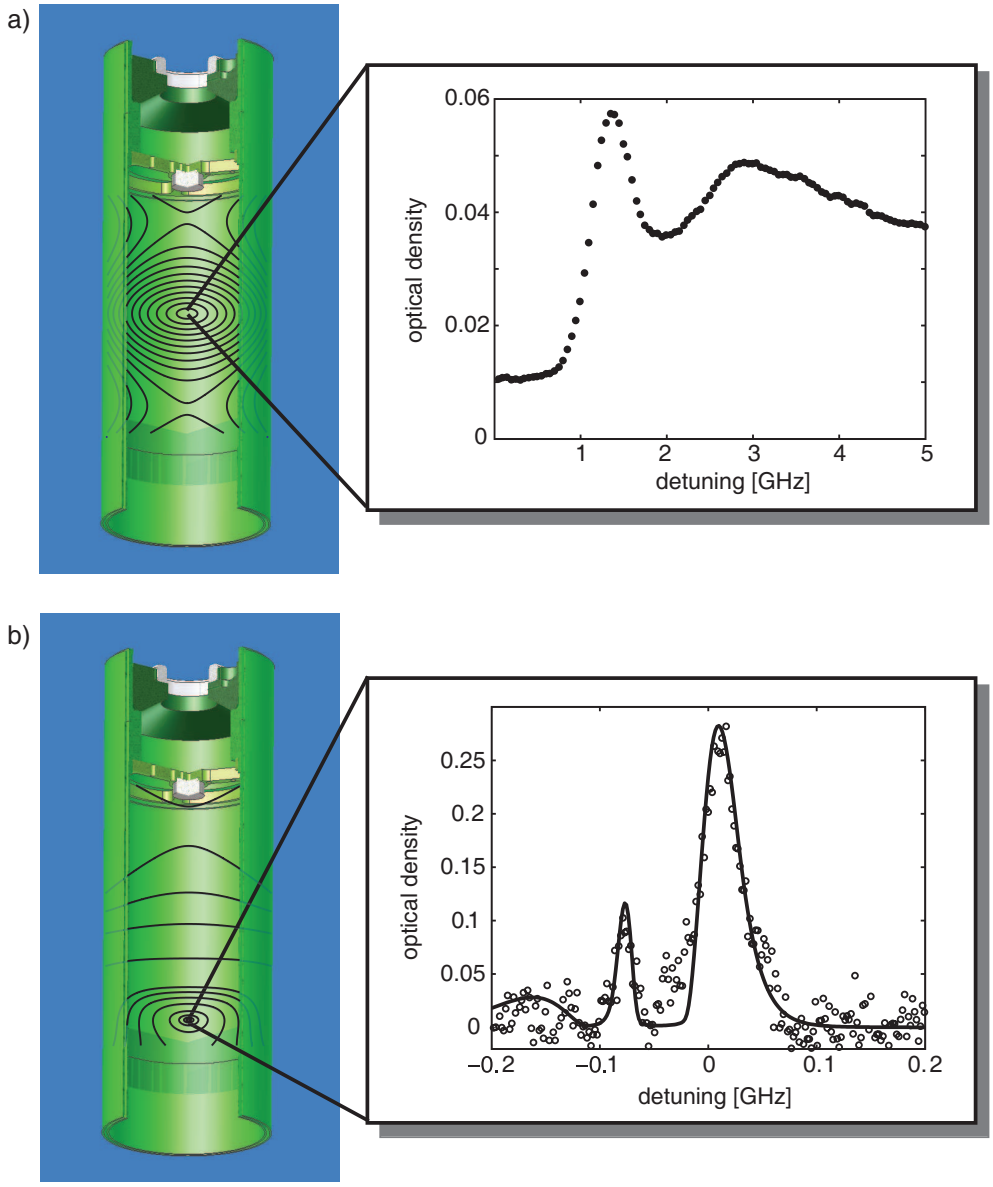

Figure 6.13: Trapping and evaporative cooling of ^{4}He*. **a)** The magnetic field contour lines at the initial trap depth $U_{\rm trap} = 4.9$ K. Inset: spectrum of trapped ^{4}He* initially loaded at 0.4 K. **b)** The contour lines at the end of the evaporation, $U_{\rm trap} = 2.7$ mK. Inset: spectrum of trapped ^{4}He* after evaporation. The fit (solid line) gives $T = 1.4 \pm 0.2$ mK, $n_o = 2.3 \pm 0.2 \times 10^{12}$ cm^{-3}, and $N = 2 \pm 0.5 \times 10^9$.

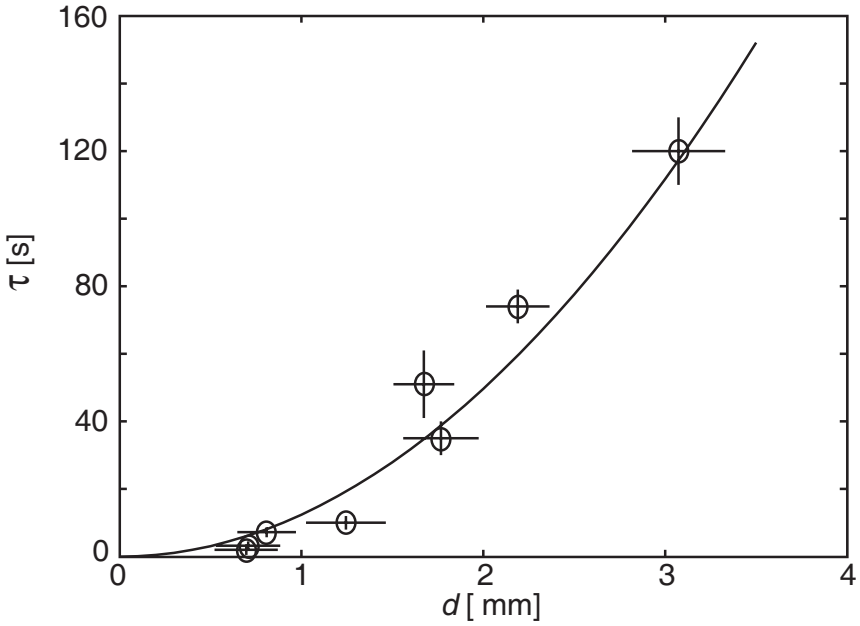

Figure 6.14: Trap loss due to Majorana flops. The open circles are measured trap lifetimes τ at various temperatures and trap confinements. Solid line is an estimation of the trap lifetime due to Majorana flops for a cloud of size d.

6.7 Majorana loss

As expected in a quadrupole trap, further evaporation is ultimately limited by Majorana flops (nonadiabatic spin flips to untrapped states) from the magnetic field zero at the center of the quadrupole trap. At the coldest temperatures, the trap lifetime decreases from hundreds of seconds to just a few seconds. Previous studies show that the loss rate due to Majorana flops is set by the ratio of the surface area of the nonadiabatic region to surface area of the atomic cloud [115, 116]. By varying the evaporation trajectory, we measure the trap lifetime at different temperatures and confinements (Fig. 6.14). For a cloud size with a spatial extent of $d \equiv 2k_{\mathrm{B}}T/\mu B'$, where B' is the average gradient of the quadrupole trap, we estimate a lifetime of $\tau = 12.4d^2$ s/mm^2, agreeing well with the measured values.

6.8 Cryostat improvements

The numbers achieved in our first demonstration of buffer gas loading of ^{4}He* were not optimized. For example, in an improved cryostat that uses a dilution refrigerator to to attain lower cell temperatures, it should be possible to load and trap at 400 mK with the valve closed. The desorption of atoms from the helium film that contributes to the background gas problem is controlled by lowering the cell temperature below 100 mK. With this method, ^{4}He* can be buffer gas loaded with 100 times more helium atoms in the cell, resulting in at least a tenfold increase in the number of trapped ^{4}He*.

In addition our present results indicate that the same improved cryostat should also lead to major improvements in the number trapped and evaporatively cooled for other atomic species with magnetic moments $\leq 2\mu_B$ (and perhaps as low as $1\mu_B$).

Chapter 7

Future Directions

The evaporative cooling of ^{4}He* from 0.4 K to 1 mK marks three significant feats. First, the 2×10^9 ^{4}He* atoms remaining at 1 mK is comparable to that attained via laser cooling [104], with much room for improvement. Second, evaporation is performed well in the multi-partial-wave regime and is efficient into the ultracold regime. And third, the phase space density is increased by 5 orders of magnitude from the initial loading conditions, the first time a significant increase in phase space density for a buffer gas loaded sample has been achieved.

7.1 Reaching quantum degeneracy

These three feats bode well for further evaporation towards quantum degeneracy. With known collision rates in the ultracold regime and high numbers and density, evaporation should be very efficient [111, 112]. However, this will require the atoms be transferred into an Ioffe trap to avoid Majorana flops [117, 118]. Furthermore, the final evaporation towards quantum degeneracy can be enhanced by using the standard method of RF evaporation [34].

The evaporation model described in Chapter 2 indicates that for our initial number of 2×10^9 and density of 2×10^{12} cm^{-3}, a Bose-Einstein condensate of $> 10^7$ ^{4}He* atoms should be easily achievable (Fig. 7.1). This is comparable to the number of condensate atoms recently produced using a multi-stage laser cooling scheme [104] to overcome previous technical difficulties, and it is comparable to condensates achieved with alkali metals [32].

7.2 Ioffe trap

One of the essential steps in reaching quantum degeneracy is transferring the cold ^{4}He* into an Ioffe trap to avoid Majorana flops. This can be done by placing a cloverleaf trap at the axial location of the cell window.

7.2.1 Cloverleaf trap

The cloverleaf trap is made of 12 coils [118] (Fig. 7.2). A pair of four coils which constitutes the "leaves" provides the radial confinement. Axial confinement is provided by a set of pinch coils, and the compensation coils sets the bias field. This trap configuration allows for independent control of the axial bias field, the axial curvature, and radial gradient. The coils are made of Nb:Ti superconducting wire and are designed to run at 10 A in all 12 coils, with the leaves in one circuit and the pinch and compensation coils running in series in a second circuit. This helps cancel out the effect of current fluctuations on the trap shape.

When fully energized, the cloverleaf trap provides a bias field of ~ 2 G, sufficient to prevent Majorana flops (Fig. 7.4). The trap depth, set by the position of the window, is 42 G ($U_{\rm trap} = 5.3$ mK). We also have strong confinement with $B'_r = 320$ G/cm and

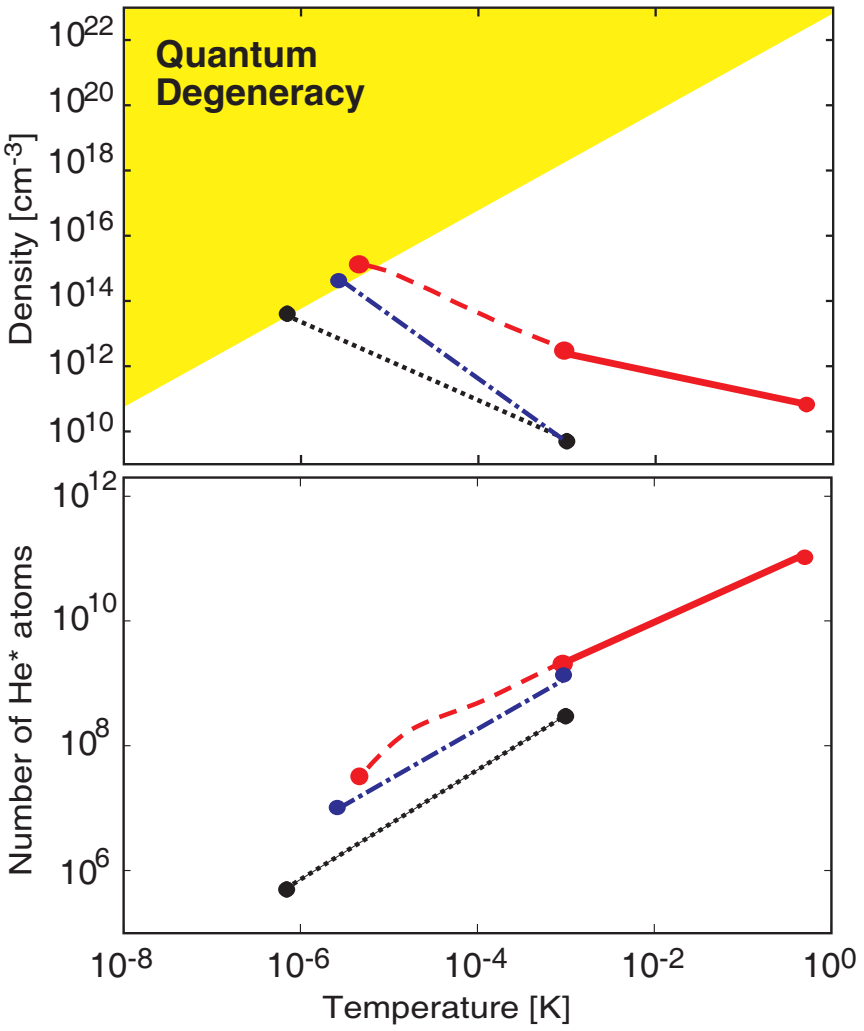

Figure 7.1: Comparison of laser cooling and buffer gas loading evaporation trajectories. The dotted line is the evaporation path for laser cooled ^{4}He* in References [102, 103]. The dashed-dotted line is the evaporation path using the multi-staged laser cooling technique in Reference [104]. The solid line is the evaporation path for the buffer gas loaded ^{4}He* presented in Chapter 6. The dashed line is the projected path for based on the evaporation model assuming the numbers and temperatures obtained after the initial evaporation.

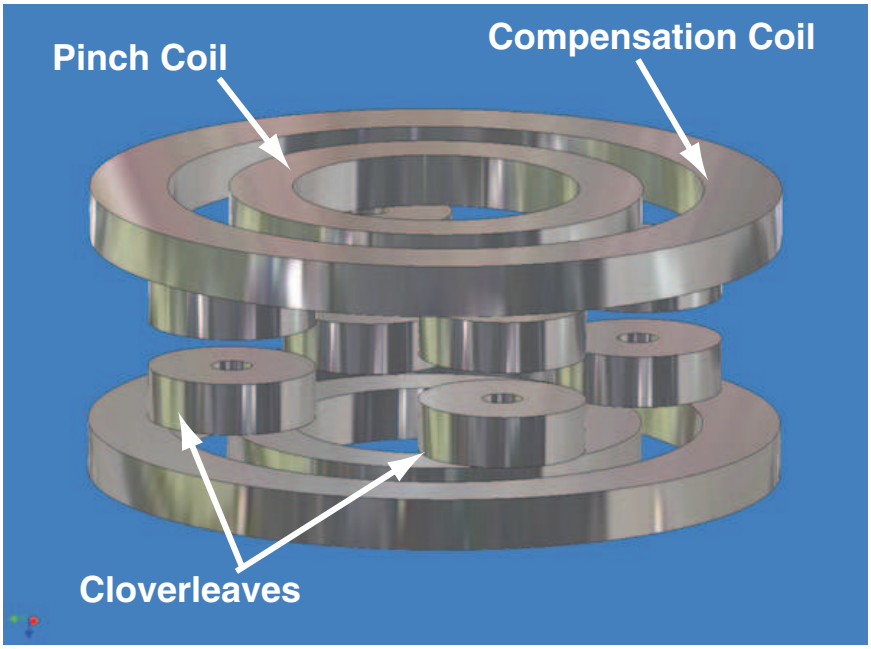

Figure 7.2: Diagram of the coils of the cloverleaf Ioffe trap.

$B"_r = 250$ G/cm^2 in the radial direction and $B'_z = 22$ G/cm and $B"_z = 540$ G/mm^2 in the axial direction. In addition, adjustments to the bias field can be made by running small currents through the bottom coil of the quadrupole magnet.

7.2.2 Cell modification

Integration of the cloverleaf trap requires a significant modification to the cell. Because of the inner diameter of the cloverleaf trap is 1 inch, the lower portion of the cell had to be modified as to make space for the cloverleaf trap (Fig. 7.3). Therefore starting at 0.75 inches below the center of the quadrupole trap, the cell walls have been shrunk to 1 inch. The 0.75 inches also coincides with the distance in which the magnetic field in the axial direction equals the magnetic field the cell walls, increasing the efficiency of evaporation against the cell window. Shrinking the walls in first required sawing off the original lower portion of the cell, taking care as to not

damage any of the glue joints in the double walled jacket. Second, the double walled jacket had to be extended from the original section down through the new extension. The inner diameter of this section is 0.5", and the outer diameter is 1". The 2.84" diameter window is replaced by a 0.5" window. The location of the window surface is now 43 mm from the center of the quadrupole trap.

The evaporation after initially loading now proceeds as follows: Initially the trap depth is set by the cell walls. As the top and bottom coil of the quadrupole trap are asymmetrically ramped down, the trapped sample is lowered down and the trap depth is now set by the distance from the trap center to the top inner edge of the cell extension. Once the atoms enter into the cell extension, the trap depth is now set by the inner diameter of the cell extension. Once the distance of the trap center to the window is shorter than the distance to the inner wall, evaporation is once again defined by the cell window.

7.2.3 Transfer from quadrupole to Ioffe trap

During the initial evaporation, the Ioffe trap can be fully energized. The magnetic fields from the quadrupole trap completely overwhelm the fields from the cloverleaf and define the magnetic trap. Once the atoms are cold (< 2 mK), the coils of the quadrupole trap can be slowly ramped to zero at a constant ratio, making a smooth transition and transfer into the Ioffe trap (Fig. 7.4). Even though multiple wells are introduced in the process, the atoms will never spill into any wells which do not eventually combine with the original well .

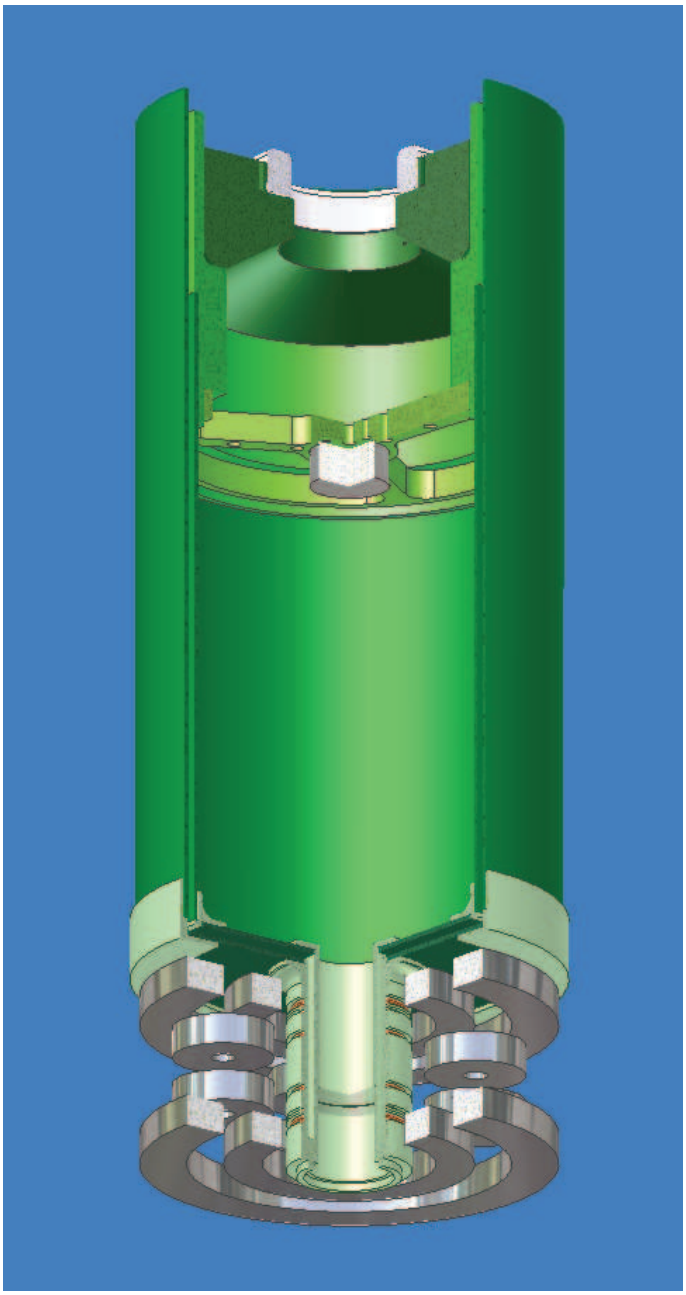

Figure 7.3: Cutaway diagram of the modifications to the original cell to accommodate the cloverleaf trap. The chrome coils are the coils to the cloverleaf trap.

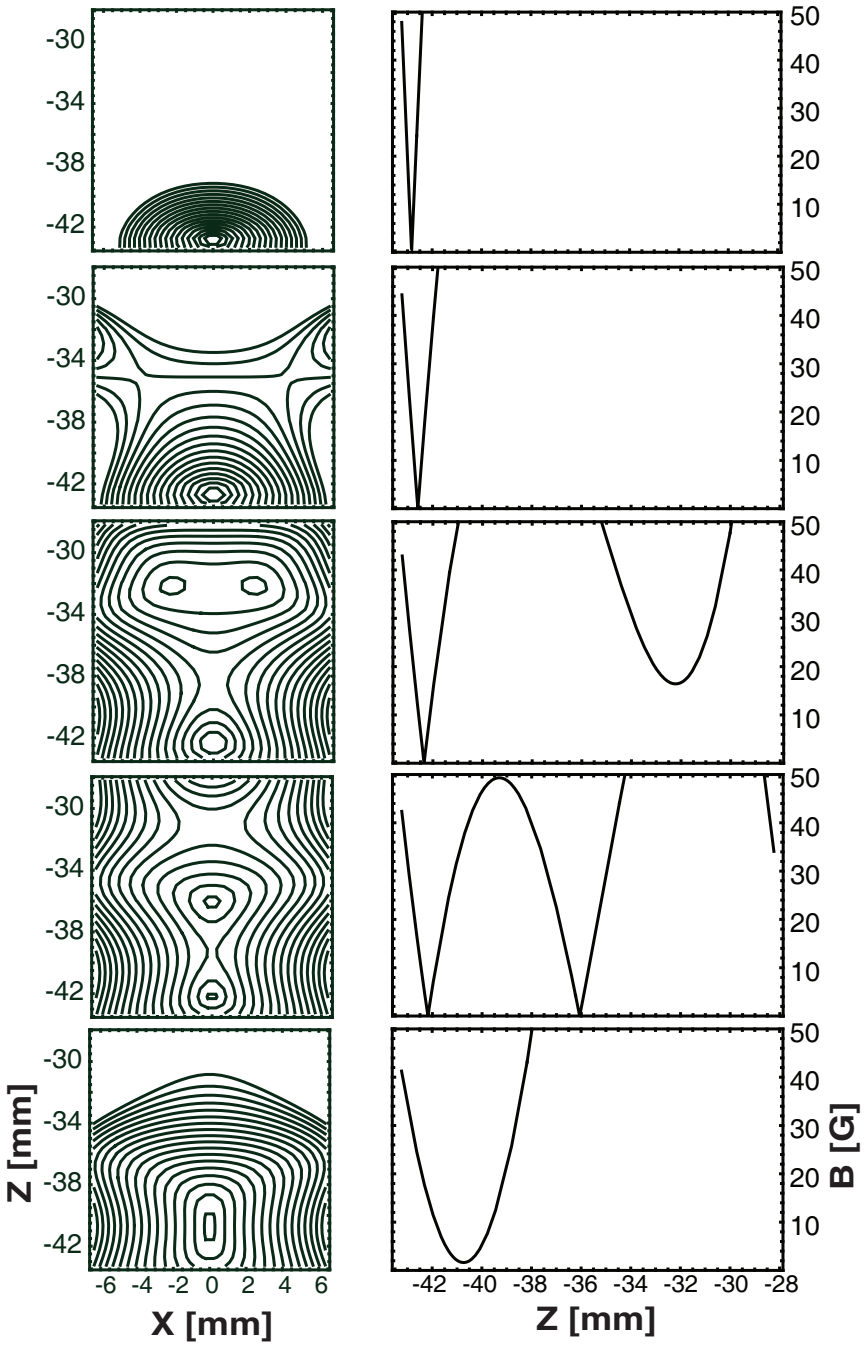

Figure 7.4: Magnetic field profiles with the Ioffe trap fully energized and the quadrupole trap being ramped to zero. The cell window is located at $z = -43$ mm and the quadrupole trap center is at $z = 0$ mm.

7.3 RF evaporation

Once transferred into the Ioffe trap, the ^{4}He* can be further cooled to degeneracy by using an RF knife to drive higher energy atoms in the trap from the $|m_S = +1\rangle$ state to the untrapped $|m_S = 0\rangle$ state. The RF knife is composed to two sets of coils mounted on the inner diameter of the form holding the cloverleaf traps. The coils are oriented such that their axes are perpendicular to the axial direction of the cell. This produces an RF field perpendicular to the bias magnetic field which is essential to efficiently drive these RF transitions.

The RF power required to efficiently evaporate the desired atoms can be determined by considering these transitions in a Landau-Zener model [119]. The probability P of making this transition is given by

$$P = 1 - \exp(-2\pi \frac{\hbar \Omega_{\mathrm{R}}^2}{\mu B_o' v}), \tag{7.1}$$

where Ω_{R}^2 is the Rabi frequency, B_o' is the gradient of the static trapping field, and v is the velocity of the ^{4}He* atom. The criteria for efficient evaporation requires that $P\omega_{\mathrm{osc}} > \Gamma_{\mathrm{el}}$ such that high energy atoms are evaporated before they collide with other atoms in the trap. ω_{osc} is the oscillation frequency, and Γ_{el} is the the elastic collision rate. The necessary Rabi frequency then is

$$\Omega_{\mathrm{R}}^2 = -\frac{\mu B_o' v}{2\pi\hbar} \ln(1 - \frac{\Gamma_{\mathrm{el}}}{\omega_{\mathrm{osc}}}). \tag{7.2}$$

Figure 7.5 plots the transverse B-field B_{min} required to efficiently evaporate as a function of temperature for various peak atom densities n_o. For a density of $n_0 = 10^{13}$ cm^{-3} and the temperature range > 300 μK, B_{min} diverges because the elastic collision rate is faster than the oscillation period. For all other densities and relevant temperature ranges, the minimum field required is < 50 mG. This is easily accomplished with the present RF electronics.

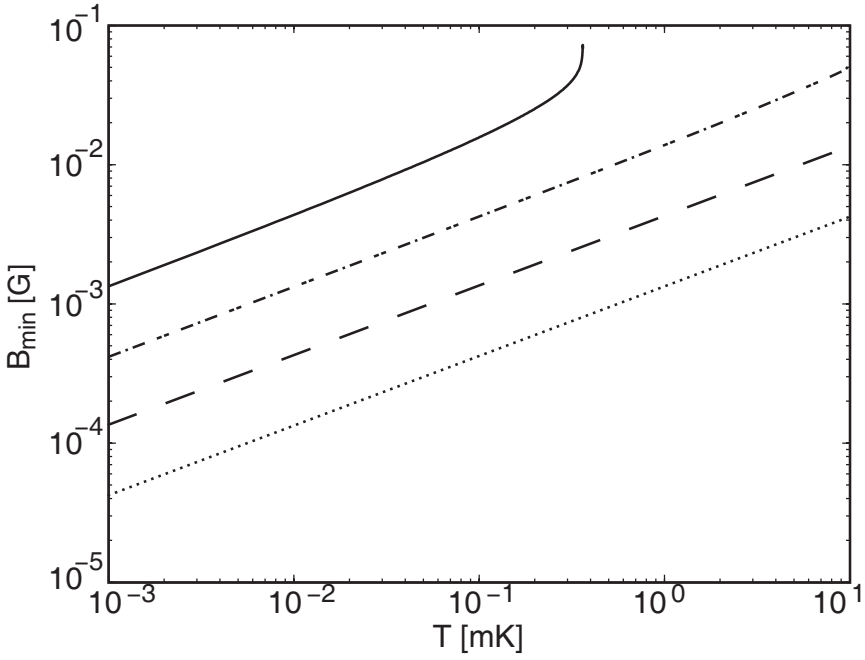

Figure 7.5: The minimum field needed to efficiently evaporate via an RF knife for various peak atom density n_o. The dotted line: $n_o = 10^{10}$ cm^{-3}. The dashed line: $n_o = 10^{11}$ cm^{-3}. The dashed dotted line: $n_o = 10^{12}$ cm^{-3}. The solid line: $n_o = 10^{13}$ cm^{-3}.

7.4 Applications with large He* BECs

Achieving Bose-condensation with $> 10^7$ atoms ^{4}He* will potentially impact several areas in atomic physics. The 20 eV of internal energy provides single-atom detection with both high temporal and spatial resolution using multichannel plates. Therefore ^{4}He* is expected to be the workhorse of future quantum atom optics experiments, where in analogy with quantum optics, the statistics and correlations of single atoms are studied. For example, recently, ^{4}He* was used for three-dimensional correlation measurements in both thermal clouds and Bose-condensates, the atomic analogue to the Hanbury-Brown Twiss experiment [120].

Additionally, this production and evaporation method could easily be extended to ^{3}He* for studies of Fermi-degenerate gases [121]. The trapping of a ^{3}He*-^{4}He*

mixture is straight forward and does not increase the experimental complexity, one advantage buffer gas loading has over laser cooling [122]. The large clouds of ^{4}He* would prove ideal as a sympathetic coolant once in the ultracold regime where the ^{3}He*-^{3}He* collision cross-section vanishes. However, in contrast to ^{4}He* there exists no calculations of the inelastic cross-sections for ^{3}He*-^{4}He* collisions. It is an open question whether the hyperfine structure of ^{3}He* will lead to the same degree of suppression of Penning ionization as that observed in ^{4}He*. As our measurement showed, this was definitely not the case for collisions between different hyperfine states of ^{3}He*. There has been however calculations of the s-wave scattering length for ^{3}He*-^{4}He* collisions [123, 114]. Based on the measured s-wave scattering length for ^{4}He*, mass scaling of the molecular potential predicts an interspecies scattering length that is large and positive. Sympathetic cooling of ^{3}He* by evaporation of ^{4}He* should prove very efficient, leading to phase separation once at quantum degeneracy [123, 124].

In addition to ^{3}He*, large clouds of ^{4}He* could potentially be used to sympathetically cool molecules [131]. Because of their complicated level structure, molecules have not been able to be directly cooled into the ultracold regime using laser cooling. There have been however multiple efforts to cool molecules using alternative methods [132]. Figure.7.6 show the status of the experimental efforts to produce cold molecules. For the methods where the molecules are still in the cold regime, the goal is to cool them further, reaching the ultracold regime with high densities. Unfortunately, in all these experiments, the densities are quite low [28, 125, 126, 127]. The molecule-molecule collisions which are essential to evaporative cooling are virtually non-existent. In addition, the multiple degrees of freedom which make molecules such an attractive candidate for many experiments also opens up a wealth of new inelastic channels which may lead to high inelastic rates [133, 134, 135].

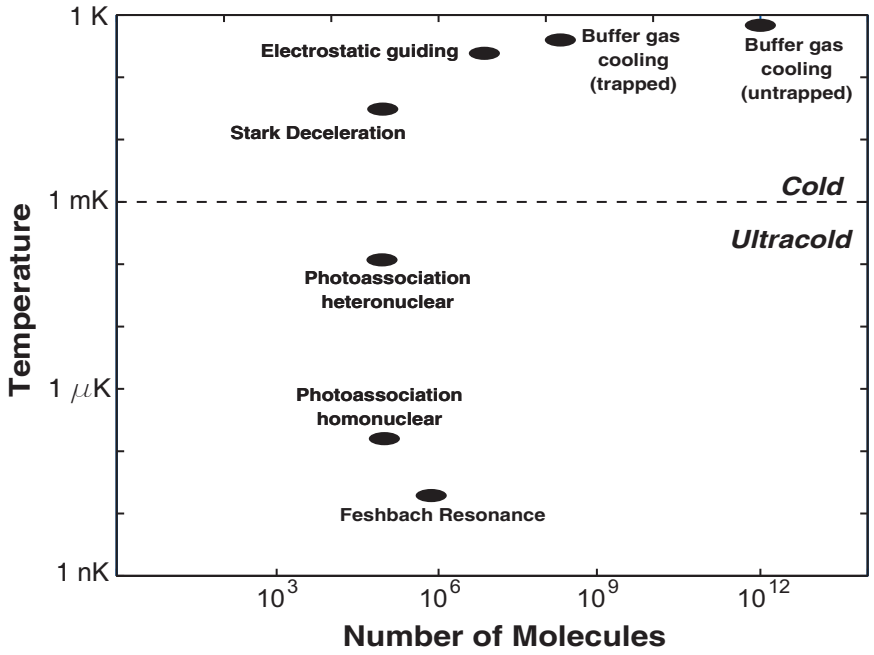

Figure 7.6: Status of current experiments producing cold and ultracold experiments [28, 125, 126, 127, 128, 129, 130].

It may be possible to circumvent these problems if we are able to simultaneously trap a large number of atoms such as ^{4}He* and the molecular species of interest. The large atom cloud would lead to high collision rates and thus act as a refrigerant for the molecular cloud. Furthermore, this decreases the number of inelastic channels. For ^{4}He*-molecule collisions in particular, Penning ionization should still be suppressed if both species are in their maximally stretched spin states. This achievement would be a breakthrough in the growing cold molecule field.

Appendix A

Asymmetric trap parameters

Evaporation against the surface of the cell window as described in Section 6.6 is achieved by independently controlling the current in the two coils of the superconducting magnet. As shown in Figure 6.10, the distance of the trap center from the surface can be controlled by the ratio $I_{\rm top}/I_{\rm bot}$. For the most part, the trap remains a linear quadrupole trap, but there are slight deviations to the trap shape. The top half of the trap is slightly different than the bottom half. The properties of this asymmetric magnetic trap are shown in Figure A.1 Fits to this data are given below.

The cell window is located a position $Z = 4.999$ cm from the original trap center. The Z location of the trap center as a function of the current ratio is

$$Z_{\rm trap}[\rm cm] = -1.215(\frac{I_{\rm top}}{I_{\rm bot}}) + 0.508. \tag{A.1}$$

The trap depth is

$$B_{\rm max}/I_{\rm bot}[\rm T/A] = -0.01515(\frac{I_{\rm top}}{I_{\rm bot}}) + 0.0691 \tag{A.2}$$

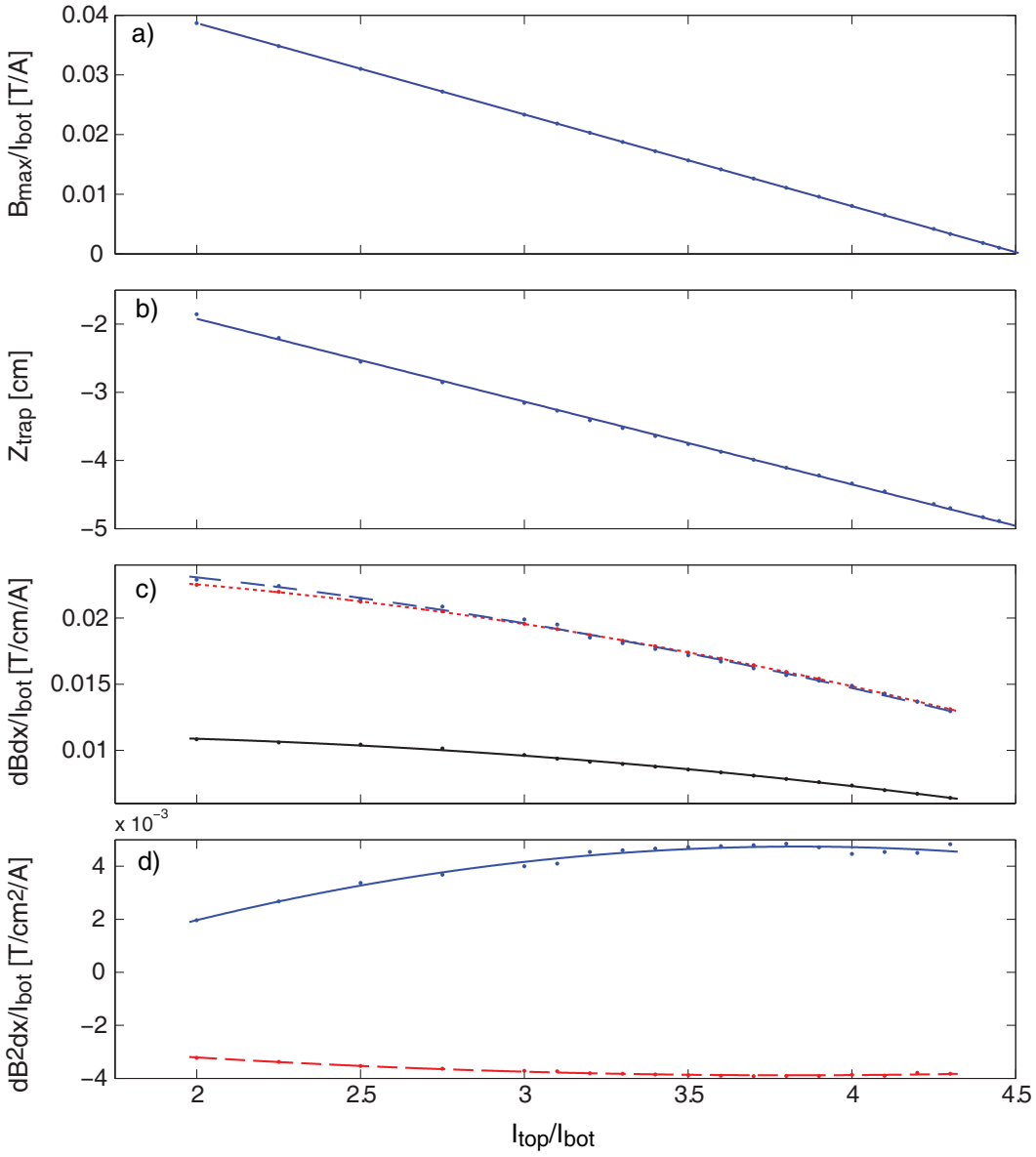

Figure A.1: Properties of the asymmetric magnetic trap. Points are values calculated from magnetic field simulations. Solid lines are polynomial fits. a) Trap depth. b) Z position of the trap center. The window is at 4.999 cm. c) The solid line is dB/dr. The dashed line is dB/dz_{top}. The dotted line is dB/dz_{bot}. d) The solid line is d^2B/dz^2_{top}. The dashed line is d^2B/dz^2_{bot}.

The first order terms in an expansion of the magnetic trap are

$$\frac{dB}{dr}/I_{\rm bot}[\mathrm{T/cmA}] = -0.00051(\frac{I_{\rm top}}{I_{\rm bot}})^2 + 0.00126(\frac{I_{\rm top}}{I_{\rm bot}}) + 0.0104 \quad \text{(A.3)}$$

$$\frac{dB}{dz_{\rm top}}/I_{\rm bot}[\mathrm{T/cmA}] = -0.00071(\frac{I_{\rm top}}{I_{\rm bot}})^2 + 0.00009(\frac{I_{\rm top}}{I_{\rm bot}}) + 0.02573 \quad \text{(A.4)}$$

$$\frac{dB}{dz_{\rm bot}}/I_{\rm bot}[\mathrm{T/cmA}] = -0.00085(\frac{I_{\rm top}}{I_{\rm bot}})^2 + 0.00127(\frac{I_{\rm top}}{I_{\rm bot}}) + 0.02339 \quad \text{(A.5)}$$

In radial direction, the fields remain linear. The second order terms for the axial direction are

$$\frac{dB^2}{dz_{\rm top}^2}/I_{\rm bot}[\mathrm{T/cm^2A}] = -0.000822(\frac{I_{\rm top}}{I_{\rm bot}})^2 + 0.0063(\frac{I_{\rm top}}{I_{\rm bot}}) - 0.0074 \quad \text{(A.6)}$$

$$\frac{dB^2}{dz_{\rm bot}^2}/I_{\rm bot}[\mathrm{T/cm^2A}] = 0.000205(\frac{I_{\rm top}}{I_{\rm bot}})^2 - 0.00156(\frac{I_{\rm top}}{I_{\rm bot}}) - 0.00091 \quad \text{(A.7)}$$

Appendix B

He* properties

Figure B.1 shows the energy level diagram for helium with the corresponding lifetime of each state. We magnetically trap the metastable triplet 2^3S_1 state which has a lifetime of 7900 s because it requires an M1 transition to decay down to the ground 1^1S_0 state [136]. We can optically detect using either the $2^3S_1 \rightarrow 2^3P$ transition at 1083 nm or $2^3S_1 \rightarrow 3^3P$ transition at 389 nm. Helium has two isotopes, ^{3}He and ^{4}He. ^{3}He has hyperfine structure with $I = 1/2$. Figure B.2 shows both the fine structure and hyperfine structure of the relevant states for both isotopes. For ^{3}He*, the hyperfine constants are listed in Table B.1. The information relevant to the spectroscopic detection are listed in Table B.2.

Table B.1: ^{3}He hyperfine constants [138]

State	2^3S_1	3^3S_1	2^3P_1	2^3P_2	3^3P_1	3^3P_2
A [GHz]	-4.494	-4.373	-2.171	-2.154	-2.168	-2.163

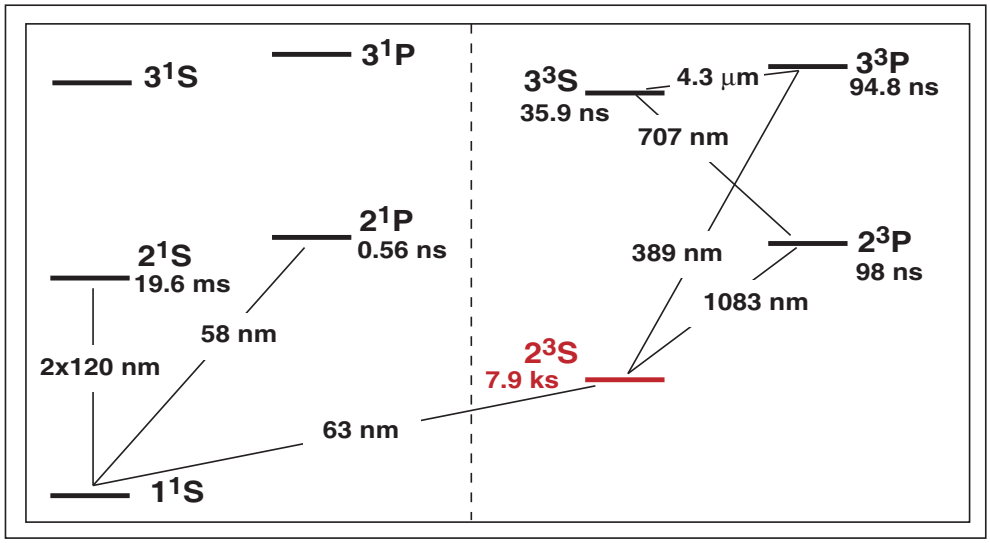

Figure B.1: Energy level diagram of helium. We magnetically trap the triplet 2^3S_1 state.

Table B.2: He* spectroscopic information [137, 139, 140]

	Transistions	
	1083 nm	389 nm
E [cm^{-1}]	9230.792	25707.687
Γ [MHz]	1.62	1.51
τ [ns]	98.0	94.8
I_{sat} [mW/cm^2]	0.167	2.35
$\Delta\nu_{\text{ISO}}$ [GHz]	-33.668	-42.184

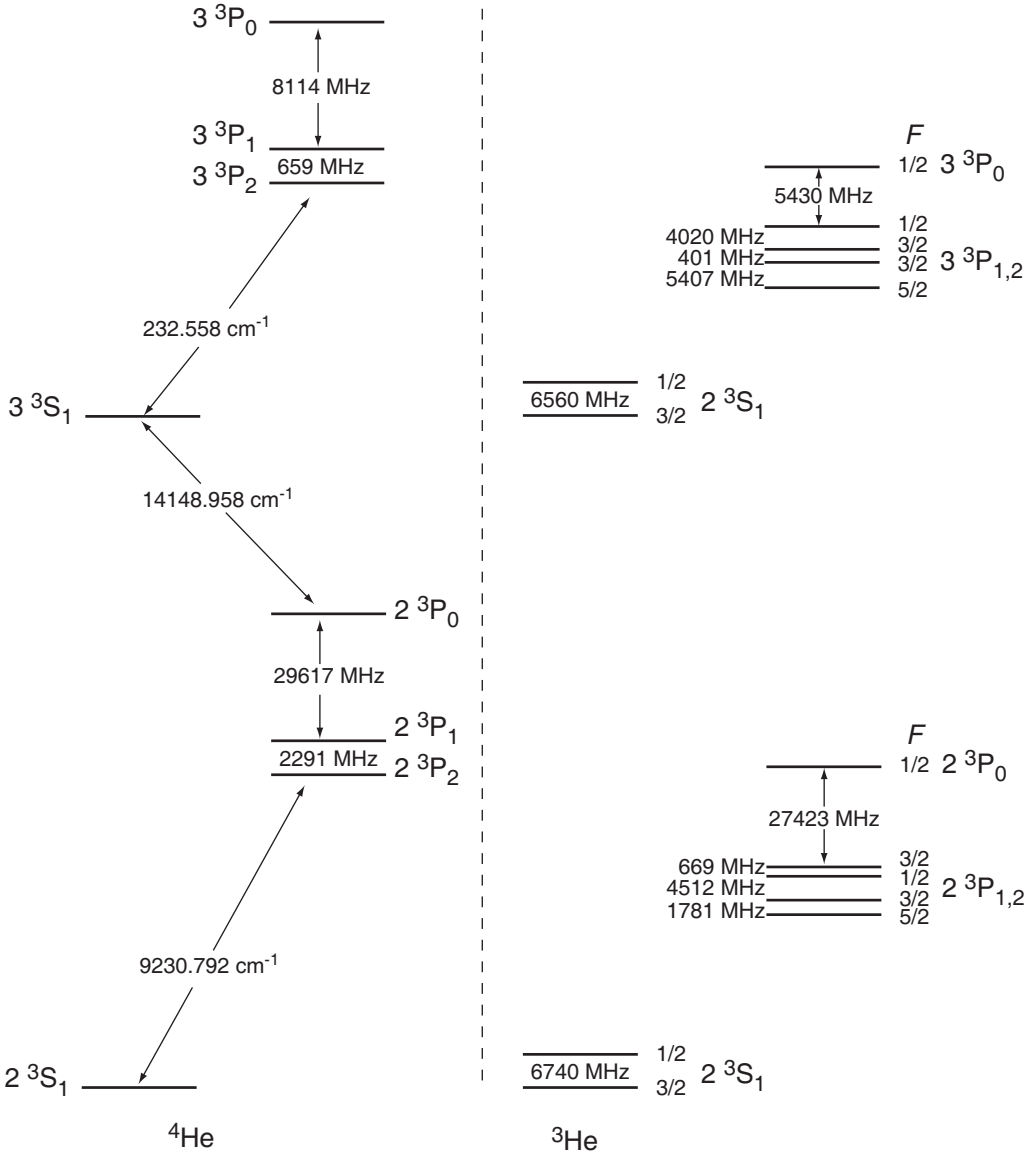

Figure B.2: Fine structure and hyperfine structure of helium [137, 138]

Appendix C

Mn properties

Manganese is a transition metal with a single bosonic isotope ^{55}Mn. It has a nuclear spin of $I = 5/2$. The ground state is $^6S_{5/2}$ with a maximum magnetic moment of $5\mu_{\mathrm{B}}$. Figure C.1 shows the Zeeman structure of the ground state. We are able to magnetically trap the maximally stretched electronic state $|m_J = +5/2\rangle$ in all six hyperfine states $m_I = +5/2, ..., -5/2$.

We spectroscopic detect Mn by exciting the ground state to the ^6P state. Table C.1 lists the energy levels and lifetimes of each fine structure levels of the ^6P state and the hyperfine constants for both the ground and excited states.

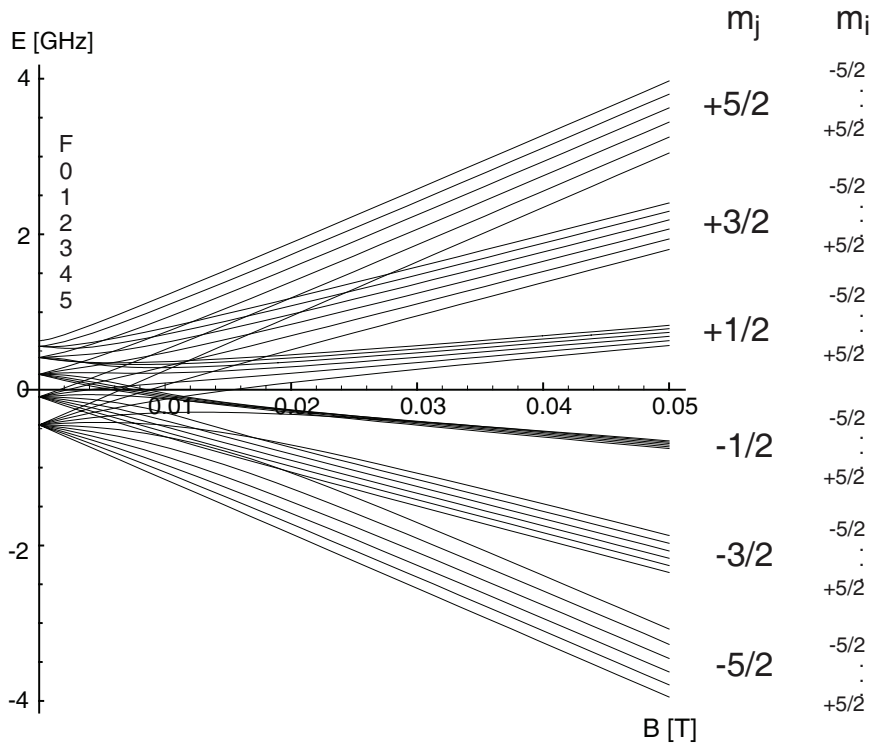

Figure C.1: Manganese Zeeman Structure

Table C.1: The energies, lifetimes [137], and hyperfine coupling constants [71, 141] of the ground and excited states used to spectroscopically detect Mn.

State	Energy [cm^{-1}]	τ [ns]	A [MHz]	B [MHz]
$^6S_{5/2}$	0	-	-72.4	0.019
$^6P_{3/2}$	24779.32	58.8	571.9	11.5
$^6P_{5/2}$	24788.05	60.6	467.4	-73.46
$^6P_{7/2}$	24802.25	63.3	429.1	63.86

Bibliography

[1] D.B. Sullivan, J.C. Bergquist, R.E. Drullinger, W.M. Itano, S.R. Jefferts, D. Lee, D. Meekhof, T.E. Parker, F.L. Walls, and D.J. Wineland. Primary atomic frequency standards at NIST. *Journal of Research of the National Institute of Standards and Technology* **106**, 47–63 (2001).

[2] M. Greiner, I. Bloch, O. Mandel, T.W. Hnsch, and T. Esslinger. Bose-einstein condensates in 1D- and 2D optical lattices. *Applied Physics B* **73**, 769–772 (2001).

[3] I. Bloch and M. Greiner. Exploring quantum matter with ultracold atoms in optical lattices. *Advances in Atomic Molecular Physics* **52**, 1–47 (2005).

[4] Mark Kasevich and Steven Chu. Atomic interferometry using stimulated Raman transitions. *Physical Review Letters* **67**, 181–184 (1991).

[5] J.F. Clauser. Ultrahigh sensitivity accelerometers and gyoscopes using neutral atom matter-wave interferometry. *Physica B and C* **151**, 262–272 (1988).

[6] Thad Walker and Paul Feng. Measurements of collisions between laser-cooled atoms. *Advances in Atomic, Molecular, and Optical Physics* **34**, 125–170 (1994).

[7] J. L. Roberts, N. R. Claussen, Jr. James P. Burke, Chris H. Greene, E. A. Cornell, and C. E. Wieman. Resonant magnetic field control of elastic scattering in cold ^{85}Rb. *Physical Review Letters* **81**, 5109–5112 (1998).

[8] P. D. Lett, K. Helmerson, W. D. Phillips, L. P. Ratliff, S. L. Rolston, and M. E. Wagshul. Spectroscopy of Na_2 by photoassociation of laser-cooled Na. *Physical Review Letters* **71**, 2200–2203 (1993).

[9] Cheng Chin, Vladan Vuletic, Andrew J. Kerman, and Steven Chu. High resolution feshbach spectroscopy of cesium. *Physical Review Letters* **85**, 2000 (2717).

[10] Paul J. Leo, Carl J. Williams, , and Paul S. Julienne. Collision properties of ultracold Cs atoms. *Physical Review Letters* **85**, 2721 (2000).

[11] J. Söding, D. Guéry-Odelin, P. Desbiolles, G. Ferrari, and J. Dalibard. Giant spin relaxation of an ultracold cesium gas. *Physical Review Letters* **80**, 1869–1872 (1998).

[12] C. C. Bradley, C. A. Sackett, J. J. Tollet, and R. G. Hulet. Evidence of Bose-Einstein condensation in an atomic gas with attractive interactions. *Physical Review Letters* **75**, 1687–1690 (1995).

[13] M.H. Anderson, J.R. Ensher, M.R. Matthews, C.E. Wieman, and E.A. Cornell. Observation of Bose-Einstein condensation in a dilute atomic vapor. *Science* **269**, 198 (1995).

[14] K. B. Davis, M. O. Mewes, M. R. Andrews, N. J. van Druten, D. S. Durfee, D. M. Kurn, and W. Ketterle. Bose-Einstein condensation in a gas of sodium atoms. *Physical Review Letters* **75**, 3969–3973 (1995).

[15] B. DeMarco and D. S. Jin. Onset of Fermi degeneracy in a trapped atomic gas. *Science* **285**, 1703 (1999).

[16] M. Greiner, O. Mandel, T. Esslinger, T.W. Hnsch, and I. Bloch. Quantum phase transition from a superfluid to a Mott insulator in a gas of ultracold atoms. *Nature* **415**, 39–44 (2002).

[17] W. Hofstetter, J. I. Cirac, P. Zoller, E. Demler, and M. D. Lukin. High-temperature superfluidity of fermionic atoms in optical lattices. *Physical Review Letters* **89**, 220407 (2002).

[18] Gianfranco Vidali, G. Ihm, Hye-Young Kim, and Milton W. Cole. Potentials of physical adsorption. *Surface Science Reports* **12**, 133–181 (1991).

[19] T. Bergeman, Gideon Erez, and Harold J. Metcalf. Magnetostatic trapping fields for neutral atoms. *Physical Review A* **35**, 1535–1546 (1987).

[20] J.G.E. Harris, R.A. Michniak, S.V. Nguyen, W.C. Campbell, D. Egorov, S.E. Maxwell, L.D. vanBuuren, and J.M. Doyle. Deep superconducting magnetic traps for neutral atoms and molecules. *Review of Scientific Instruments* **75**, 17–23 (2004).

[21] William D. Phillips and Harold Metcalf. Laser deceleration of an atomic beam. *Physical Review Letters* **48**, 596–599 (1982).

[22] William D. Phillips. Nobel lecture: Laser cooling and trapping of neutral atoms. *Review of Moden Phyics* **70**, 721–741 (1998).

[23] Wolfgang Ketterle, Kendall B. Davis, Michael A. Joffe, Alex Martin, and David E. Pritchard. High densities of cold atoms in a dark spontaneous-force optical trap. *Physical Review Letters* **70**, 2253–2256 (1993).

[24] John M. Doyle, Bretislav Friedrich, Jinha Kim, and David Patterson. Buffer-gas loading of atoms and molecules into a magnetic trap. *Physical Review A* **52**, R2515–R2518 (1995).

[25] Jinha Kim, Bretislav Friedrich, Daniel P. Katz, David Patterson, Jonathan D. Weinstein, Robert DeCarvalho, and John M. Doyle. Buffer-gas loading and magnetic trapping of atomic europium. *Physical Review Letters* **78**, 3665–3668 (1997).

[26] Jonathan D. Weinstein, Robert deCarvalho, Cindy I. Hancox, and John M. Doyle. Evaporative cooling of atomic chromium. *Physical Review A* **65**, 021604R (2002).

[27] Cindy I. Hancox, S. Charles Doret, Matthew T. Hummon, Linjiao Luo, and John M. Doyle. Magnetic trapping of rare-earth atoms at millikelvin temperatures. *Nature* **431**, 281–284 (2004).

[28] Jonathan D. Weinstein, Robert deCarvalho, Thierry Guillet, Bretislav Friedrich, and John M. Doyle. Magnetic trapping of calcium monohydride molecules at millikelvin temperatures. *Nature* **395**, 148–150 (1998).

[29] Robert deCarvalho, John M. Doyle, Bretislav Friedrich, Thierry Guillet, Jinha Kim, David Patterson, and Jonathan D. Weinstein. Buffer-gas loaded magnetic traps for atoms and molecules: a primer. *European Physical Journal D* **7**, 289–309 (1999).

[30] Jack G. Harris, Robert A. Michniak, Scott V. Nguyen, Nathaniel Brahms, Wolfgang Ketterle, and John M. Doyle. Buffer-gas cooling and trapping of atoms with small effective magnetic moments. *Europhysics Letters* **67**, 198–204 (2004).

[31] Axel Griesmaier, Jorg Werner, Sven Hensler, Jurgen Stuhler, and Tilman Pfau. Bose-Einstein condensation of chromium. *Physical Review Letters* **94**, 160401 (2005).

[32] W. Ketterle and N. J. Van Druten. Evaporative cooling of trapped atoms. *Advances in Atomic, Molecular, and Optical Physics* **37**, 181–236 (1996).

[33] Harald F. Hess. Evaporative cooling of magnetically trapped and compressed spin-polarized hydrogen. *Physical Review B* **34**, 3476–3479 (1986).

[34] A.G. Martin, K. Helmerson, V.S. Bagnato, G.P. Lafyatis, and D.E. Pritchard. RF spectroscopy of trapped neutral atoms. *Physical Review Letters* **61**, 2431–2434 (1989).

[35] D. M. Harver, J. M. McGuirk, J. M. Obrecht, and E. A. Cornell. Thermally induced losses in ultra-cold atoms magnetically trapped near room-temperature surfaces. *Journal of Low Temperature Physics* **133**, 229–238 (2003).

[36] J. M. Doyle, J. C. Sandberg, N. Masuhara, I. A. Yu, D. Kleppner, and T. J. Greytak. Energy distributions of trapped atomic hydrogen. *JOSA B* **6**, 2244 (1989).

[37] T. Weber, J. Herbig, M. Mark, H.-C. Ngerl, and R. Grimm. Bose-Einstein condensation of chromium. *Science* **299**, 232 (2003).

[38] J. J. Sakurai and San Fu Tuan. *Modern Quantum Mechanics*. Revised edition. Addison-Wesley, 1994.

[39] H. M. J. M. Boesten, C. C. Tsai, J. R. Gardner, D. J. Heinzen, and B. J. Verhaar. Observation of a shape resonance in the collision of two cold ^{87}Rb atoms. *Physical Review A* **55**, 636–640 (1997).

[40] J.M. Doyle, J.C. Sandberg, I.A. Yu, C.L. Cesar, D. Kleppner, and T.J. Greytak. Evaporative cooling of atomic hydrogen: Theory of cooling and progress towards the Bose-Einstein transition. *Physica B* **13**, 194–196 (1994).

[41] A. J. Moerdijk and B. J. Verhaar. Collisional two- and three-body decay rates of dilute quantum gases at ultralow temperatures. *Physical Review A* **53**, R19–R22 (1996).

[42] Rob deCarvalho and John Doyle. Evaporative cooling at low trap depth. *Physical Review A* **70**, 053409 (2004).

[43] T. J. Greytak, D. Kleppner, D. G. Fried, T. C. Killian, L. Willmann, D.Landhuis, and S.C.Moss. Bose-Einstein condensation in atomic hydrogen. *Physica B* **280**, 20–26 (2000).

[44] Robert deCarvalho, Cindy I. Hancox, and John M. Doyle. Enhanced inelastic scattering rates of cold atomic chromium. *Journal of the Optical Society of America B* **20**, 1131 (2003).

[45] Z. Pavlovic, B.O. Roos, R. Cote, R, and H.R. Sadeghpour. Collisional properties of trapped cold chromium atoms. *Physical Review A* **69**, 030701 (2004).

[46] Z. Pavlovic, R.V. Krems, R. Cote, R, and H.R. Sadeghpour. Magnetic Feshbach resonances and Zeeman relaxation in bosonic chromium gas. *Physical Review A* **71**, 061402 (2005).

[47] J. Werner, A. Griesmaier, S. Hensler, J. Stuhler, T. Pfau, A. Simoni, and E. Tiesinga. Observation of Feshbach resonances in an ultracold gas of ^{52}Cr. *Physical Review Letters* **94**, 183201 (2005).

[48] Jonathan D. Weinstein. *Magnetic trapping of atomic chromium and molecular calcium monohydride.* PhD thesis, Harvard University, 2001.

[49] L. Santos, G. V. Shlyapnikov, P. Zoller, and M. Lewenstein. Bose-Einstein condensation in trapped dipolar gases. *Physical Review Letters* **85**, 1791 (2000).

[50] R.K. Nesbet. Heisenberg exchange interaction of two Mn atoms. *Physical Review* **135**, A460 (1964).

[51] C. A. Baumann, R. J. Van Zee, S. V. Bhat, and W. Weltner Jr. ESR of Mn_2 and Mn_5 molecules in rare-gas matrices. *The Journal of Chemical Physics* **78**, 190–199 (1983).

[52] S.K. Nayak and P. Jena. Anomalous magnetism in small Mn clusters. *Chemical Physics Letters* **289**, 473 (1998).

[53] Bingwu Wang and Zhida Chen. Magnetic coupling interaction under different spin multiplets in neutral manganese dimer: CASPT2 theoretical investigation. *Chemical Physics Letters* **387**, 395 (2004).

[54] R. J. Van Zee, C. A. Baumann, and Jr. W. Weltner. The antiferromagnetic Mn_2 molecule. *The Journal of Chemical Physics* **74**, 6977–6978 (1981).

[55] M. R. Pederson, F. Reuse, and S. N. Khanna. Magnetic transition in Mn (n=28) clusters. *Physical Review B* **58**, 5632 (1998).

[56] R. J. Van Zee and Jr. W. Weltner. The ferromagnetic Mn_2 molecule. *The Journal of Chemical Physics* **89**, 4444–4446 (1988).

[57] R. J. Van Zee, C. A. Baumann, S. V. Bhat, and Jr. W. Weltner. ESR of the high-spin (s = 25/2) Mn_2 molecule. *The Journal of Chemical Physics* **76**, 5636–5637 (1982).

[58] M. Valiev, E. J. Bylaska, and J. H. Weare. Calculations of the electronic structure of $3d$ transition metal dimers with projector augmented plane wave method. *The Journal of Chemical Physics* **119**, 5955–5964 (2003).

[59] Florentino Lopez-Urias and Alejandro Diaz-Ortiz. Magnetism in Mn clusters: Interplay between spin ordering and structure. *Physical Review B* **68**, 132405 (2003).

[60] Cindy I. Hancox, Stephen C. Doret, Matthew T. Hummon, Roman Krems, and John M. Doyle. Suppression of angular momentum transfer in cold collisions of transition metal atoms in ground states with nonzero orbital angular momentum. *Physical Review Letters* **94**, 013201 (2005).

[61] R. V. Krems, J. Klos, M. F. Rode, M. M. Szczesniak, G. Chalasinski, and A. Dalgarno. Suppression of angular forces in collisions of non-S-state transition metal atoms. *Physical Review Letters* **94**, 103202 (2005).

[62] Robin Santra and Chris H. Greene. Tensorial analysis of the long-range interaction between metastable alkaline-earth-metal atoms. *Physical Review A* **67**, 062713 (2003).

[63] Viatcheslav Kokoouline, Robin Santra, and Chris H. Greene. Multichannel cold collisions between metastable Sr atoms. *Physical Review Letters* **90**, 253201 (2003).

[64] Roman V. Krems and Alex Dalgarno. Disalignment transitions in cold collisions of ^3P atoms with structureless targets in a magnetic field. *Physical Review A* **68**, 013406 (2003).

[65] Robert Michniak. *Enhanced buffer gas loading: cooling and trapping of atoms with low effective magnetic moments*. PhD thesis, Harvard University, 2004.

[66] L. Cai, B. Friedrich, and J.M. Doyle. Simulation of the hyperfine-resolved Zeeman spectrum of Eu atoms in a magnetic trap. *Physical Review A* **61**, 033412/1 (2000).

[67] John David Jackson. *Classical Electrodynamics*. 2nd edition. John Wiley & Sons Inc., 1975.

[68] Claude Cohen-Tannoudji, Jacques Dupont-Roc, and Gilbert Grynberg. *Atom-Photon Interactions: basic processes and applications*. John Wiley & Sons, Inc., 1992.

[69] H. T. C. Stoof, J. M .V. A. Koelman, and B. J. Verhaar. Spin-exchange and dipole relaxation rates in atomic hydrogen: Rigorous and simplified calculations. *Physical Review B* **38**, 4688–4697 (1988).

[70] B. J. Verhaar E. Tiesinga, S. J. M. Kuppens and H. T. C. Stoof. Collisions between cold ground-state Na atoms. *Physical Review A* **43**, 5188 (1991).

[71] S.J. Davis, J.J. Wright, and L.C. Balling. Hyperfine structure of the ground state of ^{55}Mn. *Physical Review A* **3**, 1220 (1971).

[72] G. D. Telles, W. Garcia, L. G. Marcassa, V. S. Bagnato, D. Ciampini, M. Fazzi, J. H. Mller, D. Wilkowski, and E. Arimondo. Trap loss in a two-species Rb-Cs magneto-optical trap. *Physical Review A* **63**, 033406 (2001).

[73] J.P. Shaffer, W. Chalupczak, and N.P. Bigelow. Trap loss in a two-species Na-Cs magneto-optical trap: Intramultiplet mixing in heteronuclear ultracold collisions. *Physical Review A* **60**, R3365 (year).

[74] Z. Hadzibabic, S. Gupta, C.A. Stan, C.H. Schunck, M.W. Zwierlein, K. Dieckmann, and W. Ketterle. Fiftyfold improvement in the number of quantum degenerate fermionic atoms. *Physical Review Letters* **91**, 160401 (2003).

[75] Cindy I. Hancox, Matthew T. Hummon, Scott V. Nguyen, and John M. Doyle. Evaporative cooling of magnetically trapped atomic molybdenum. *Physical Review A* **71**, 031402 (2005).

[76] AIN Plastics, `http://www.tincna.com/ain1.htm`.

[77] Spaulding Composites, Co., `http://www.spauldingcom.com`.

[78] D.W. Sedgley, A.G. Tobin, T.H. Batzer, and W.R. Call. Characterization of charcoals for helium cryopumping in fusion devices. *Journal of Vacuum Science & Technology A (Vacuum, Surfaces, and Films* **5**, 2572–2576 (1987).

[79] ^{3}He Refrigerator, Janis Research, `www.janis.com/`.

[80] I.Y. Fugol, O.N. Grigorashchenko, and D.A.Myshkis. Experimental investigation of the destruction of metastable atoms of helium in a plasma at low temperatures. *JETP* **33**, 227 (1971).

[81] A. Wayne Johnson and J. B. Gerardo. Electronic recombination coefficient of molecular helium ions. *Physical Review Letters* **27**, 835 (1971).

[82] F.Pereira Dos Santos, F.Perales, J.Lonard, A.Sinatra, Junmin Wang, F.Saverio Pavone, E.Rasel, C.S.Unnikrishnan, , and M.Leduc. Efficient magneto-optical trapping of a metastable helium gas. *The European Physical Journal - Applied Physics* **14**, 69 (2001).

[83] Stycast 1266 A/B epoxy. Emerson & Cuming Inc., `http://www.emersoncuming.com/`.

[84] HP Model 8647A.

[85] ZSDR-230 RF Switch. Mini Circuits, `http://www.minicircuits.com/`.

[86] EIN Model 325LA.

[87] Dennis S. Greywall. Thermal-conductivity measurements in liquid ^{4}He below 0.7 K. *Physical Review B* **23**, 2152–2168 (1981).

[88] Frank Pobell. *Matter and Methods at Low Temperatures*. Springer-Verlag, 1992.

[89] P. A. Busch, S. P. Cheston, and D. S. Greywall. Properties of sintered-silver heat exchangers. *Cryogenics* **24**, 445–447 (1984).

[90] J. A. Nissen, D. R. Swanson, Z. K. Geng, K. Kim, P. Day, and J. A. Lipa. Superfluid density as a function of temperature and pressure near the lambda line. *Physica B* **284-288**, 51 (2000).

[91] Dale G. Fried. *Bose-Einstein Condensation of Atomic Hydrogen*. PhD thesis, Massachusetts Institute of Technology, 1999.

[92] Carlo Egon Heinrich Mattoni. *Magnetic Trapping of Ultracold Neutrons Produced Using a Monochromatic Cold Neutron Beam*. PhD thesis, Harvard University, 2001.

[93] Lakeshore Models 622,623. `http://www.lakeshore.com/`.

[94] Kepco Model BOP-36-6 M. `http://www.kepcopower.com/`.

[95] NI PXI 6713. National Instruments, `http://www.ni.com/`.

[96] NI PXI 6733. National Instruments, `http://www.ni.com/`.

[97] DL100, Toptica, `www.toptica.com/`.

[98] InGaAs, 3 mm active area, TE cooled. Electro Optical Systems, `http://www.eosystems.com/`.

[99] Continuum Surelite I-10. Continuum. `http://www.continuumlasers.com/`.

[100] 02MPQ007/001 Melles Griot Max-Brite mirror. Melles Griot, `http://www.mellesgriot.com`.

[101] W. Ketterle, private communication.

[102] A. Robert, O. Sirjean, A. Browaeys, J. Poupard, S. Nowak, D. Boiron, C. I. Westbrook, and A. Aspect. A Bose-Einstein condensate of metastable atoms. *Science* **292**, 461–464 (2001).

[103] F. P. Dos Santos, J. Leonard, J. M. Wang, C. J. Barrelet, F. Perales, E. Rasel, C. S. Unnikrishnan, M. Leduc, and C. Cohen-Tannoudji. Bose-Einstein condensation of metastable helium. *Physical Review Letters* **86**, 3459–3462 (2001).

[104] A. S. Tychkov, T. Jeltes, J. M. McNamara, P. J. J. Tol, N. Herschbach, W. Hogervorst, and W. Vassen. Metastable helium Bose-Einstein condensate with a large number of atoms. *Physical Review A* **73**, 031603 (2006).

[105] J.R. Woodworth and H.W. Moos. Experimental determination of the single-photon transition rate between 2^3S_1 and 1^1S_0 of He I. *Physical Review A* **12**, 2455 (1975).

[106] A. Wayne Johnson and J.B. Gerardo. Ionizing collisions of two metastable helium atoms (2^3S). *Physical Review A* **7**, 925 (1973).

[107] R. J. W. Stas, J. M. McNamara, W. Hogervorst, and W. Vassen. Homonuclear ionizing collisions of laser-cooled metastable helium atoms. *Physical Review A (Atomic, Molecular, and Optical Physics)* **73**, 032713 (2006).

[108] H. C. Mastwijk, J. W. Thomsen, P. van der Straten, and A. Niehaus. Optical collisions of cold, metastable helium atoms. *Physical Review Letters* **80**, 5516 (1998).

[109] Mitsutaka Kumakura and Norio Morita. Laser trapping of metastable ^{3}He atoms: Isotopic difference in cold Penning colliions. *Physical Review Letters* **82**, 2848 (1999).

[110] G.V. Shlyapnikov, J.T.M. Walraven, U.M. Rahmanov, and M.W. Reynolds. Decay kinetics and Bose condensation in a gas of spin-polarized triplet helium. *Physical Review Letters* **73**, 3247 (1994).

[111] P.O. Fedichev, M.W. Reynolds, U.M. Rahmanov, and G.V. Shlyapnikov. Inelastic decay processes in a gas of spin-polarized triplet helium. *Physical Review A* **53**, 1447 (1996).

[112] S. Moal, M. Portier, J. Kim, J. Dugue, U. D. Rapol, M. Leduc, and C. Cohen-Tannoudji. Accurate determination of the scattering length of metastable helium atoms using dark resonances between atoms and exotic molecules. *Physical Review Letters* **96**, 023203 (2006).

[113] S.V. Nguyen, J.G.E. Harris, S.C. Doret, J.Helton, R.A. Michniak, W. Ketterle, and J.M. Doyle. Spin-exchange and dipolar relaxation of magnetically trapped Mn. *to be submitted* (2005).

[114] P.J. Leo, V. Venturi, I.B. Whittingham, and J.F. Babb. Ultracold collisions of metastable helium atoms. *Physical Review A* **64**, 042710 (2001).

[115] Wolfgang Petrich, Michael H. Anderson, Jason R. Ensher, and Eric A. Cornell. Stable, tightly confining magnetic trap for evaporative cooling of neutral atoms. *Physical Review Letters* **74**, 3352–3355 (1995).

[116] Kendall B. Davis, Marc-Oliver Mewes, Micael A. Joffe, Michael R. Andrews, and Wolfgang Ketterle. Evaporative cooling of sodium atoms. *Physical Review Letters* **74**, 5202–5205 (1995).

[117] Tilman Esslinger, Immanuel Bloch, and Theodor W. Hänsch. Bose-Einstein condensation in a quadrupole-Ioffe-configuration trap. *Physical Review A* **58**, R2664–R2667 (1998).

[118] M. O. Mewes, M. R. Andrews, N. J. van Druten, D. M. Kurn, D. S. Durfee, and W. Ketterle. Bose-Einstein condensation in a tightly confining dc magnetic trap. *Physical Review Letters* **77**, 416–420 (1996).

[119] J.R. Rubbmark, M.M. Kash, M.G. Littman, and D. Kleppner. Dynamical effects at avoided level crossings: A study of the Landau-Zener effect using rydberg atoms. *Physical Review A* **56**, R4377 (1997).

[120] M. Schellekens, R. Hoppeler, A. Perrin, J. Viana Gomes, D. Boiron, A. Aspect, and C. I. Westbrook. Hanbury-Brown Twiss effect for ultracold quantum gases. *Science* **310**, 5748 (2005).

[121] R. J. W. Stas, J. M. McNamara, W. Hogervorst, and W. Vassen. Simultaneous magneto-optical trapping of a Boson-Fermion mixture of metastable helium atoms. *Physical Review Letters* **93**(5), 053001 (2004).

[122] S.V. Nguyen, J.S. Helton, K. Maussang, W. Ketterle, and J.M. Doyle. Magnetic trapping of an atomic ^{55}Mn-^{52}Cr mixture. *Physical Review A* **71**, 025602 (2005).

[123] A.S. Dickinson, F.X. Gadea, and T Leininger. Scattering lengths for spin-polarized metastable helium3- and helium-4. *Journal of Physics B: Atomic, Molecular, and Optical Physics* **37**, 587 (2004).

[124] P. Capuzzi and E. S. Hernandez. Phase separation and response of ^{3}He-^{4}He mixture within a magnetic trap. *Physical Review A* **66**, 035602 (2002).

[125] K. Maussang, D. Egorov, J.S. Helton, S.V. Nguyen, and J.M. Doyle. Zeeman relaxation of CaF in low-temperature collisions with helium. *Physical Review Letters* **94**, 123002 (2005).

[126] T. Rieger, T. Junglen, S. A. Rangwala, P. W. H. Pinkse, and G. Rempe. Continuous loading of an electrostatic trap for polar molecules. *Physical Review Letters* **95**, 173002 (2005).

[127] Sebastiaan Y. T. van de Meerakker, Paul H. M. Smeets, Nicolas Vanhaecke, Rienk T. Jongma, and Gerard Meijer. Deceleration and electrostatic trapping of OH radicals. *Physical Review Letters* **94**, 023004 (2005).

[128] Jeremy M. Sage, Sunil Sainis, Thomas Bergeman, and David DeMille. Optical production of ultracold polar molecules. *Physical Review Letters* **94**, 203001 (2005).

[129] Roahn Wynar, R. S. Freeland, D. J. Han, C. Ruy, and D. J. Heinzen. Molecules in a Bose-Einstein condensate. *Science* **287** (2000).

[130] M. W. Zwierlein, C. A. Stan, C. H. Schunck, S. M. F. Raupach, S. Gupta, Z. Hadzibabic, and W. Ketterle. Observation of Bose-Einstein Condensation of molecules. *Physical Review Letters* **91**, 250401 (2003).

[131] Pavel Soldan and Jeremy M. Hutson. Interaction of NH($X\Sigma^-$) molecules with rubidium atoms: Implications for sympathetic cooling and the formation of extremely polar molecules. *Physical Review Letters* **92**, 163202 (2004).

[132] J. Doyle, B. Friedrich, R.V. Krems, and F. Masnou-Seeuws. Quo vadis, cold molecules? - Editorial review. *European Physical Journal D* **31**, 149 (2004).

[133] N. Balakrishnan, R. C. Forrey, and A. Dalgarno. Threshold phenomena in ultracold atom-molecule collisions. *Chemical Physics Letters* **280**, 1–4 (1997).

[134] N. Balakrishnan, V. Karchenko, R. C. Forrey, and A. Dalgarno. Vibrational relaxation of trapped molecules. *Physical Review A* **59**, 2146–2152 (1999).

[135] John L. Bohn. Inelastic collisions of ultracold polar molecules. *Physical Review A* **63**, 052714 (2001).

[136] G.W.F. Drake. Theory of relativistic magnetic dipole transitions: Lifetime of the metastable 2^3S state of the heliumlike ions. *Physical Review A* **3**, 908 (1971).

[137] NIST atomic spectra database, URL `http://physics.nist.gov/PhysRefData-/ASD/index.html`.

[138] B.C. Gou, F. Wang, and X.L. Wu. Fine structure and hyperfine structure of some excited states of helium. *European Physical Journal D* **27**, 27 (2003).

[139] Ping Zhao, J. R. Lawall, and F. M. Pipkin. High-precision isotope-shift measurement of 2^3S-2^3P transition in helium. *Physical Review Letters* **66**, 592–595 (1991).

[140] F. Marin, F. Minardi, F. S. Pavone, and M. Inguscio. Precision measurement of the isotope shift of the $2^3S_1 - 2^3P_0$ transition in helium. *Physical Review A* **49**, R1523 (1994).

[141] E. Handrich, A. Steudel, and H. Walther. The hyperfine splitting of the $3d^5 4s 4p$ levels of Mn I and the quadrupole moment of ^{55}Mn. *Physics Letters A* **29**, 486 (1969).